Use of In-Operation Modal Analysis for the dynamic identification of rail-head irregularities and train modal parameters: Functional design of a novel device for railway diagnostic

Politecnico di Bari

Department of Mechanics, Mathematics and Management
MECHANICAL AND MANAGEMENT ENGINEERING
Ph.D. Program
SSD: ING-IND/13–Applied Mechanics

Final Dissertation

Use of In-Operation Modal Analysis for the dynamic identification of rail-head irregularities and train modal parameters: Functional design of a novel device for railway diagnostic vehicles

---

by
Bisceglia Giulio

Supervisors:

Prof. Soria Leonardo

Coordinator of Ph.D. Program:
Prof. Demelio Giuseppe Pompeo

Course n°34, 01/12/2018-20/11/2022

ABSTRACT

The Operational Modal Analysis (OMA) represents one of the most used techniques for the structural identification in civil engineering. Unfortunately, the NExT hypotheses (Natural Excitation Techniques) make the OMA not applicable to a railway vehicle.
In this context , the present document shows the functional design of a novel device for railway diagnostic vehicles, capable to implement the so called “In-Operation Modal Analysis” (based on a particular modal partial fraction decomposition of the power spectral densities, or PSD, response matrix, specifically dedicated to the case of track-vehicle interaction) for the dynamic identification of train modal parameters and rail-head irregularities, which represent one of the principal sources of excitation for a railway vehicle. This method allows the indirect characterization of statistical properties of rail surface roughness, starting from the output signals (e.g., accelerations) acquired on vehicles in working conditions, combined with some knowledge about the frequency response functions (FRFs) matrix of the vehicle. Moreover, by exploiting homogeneity properties, it is possible to reduce the number of quantities to be estimated for the features evaluation of parallel track profiles belonging to the same running surface. Then it is allowed to identify specific roughness statistical properties, such as the associated auto-power spectral densities (auto-PSDs) and their relevant coherence function.
This modal structure incorporates train modal parameters and statistical rail-roughness as unknowns to be identified by employing data from a simple set-up of accelerometers distributed only on some strategical measuring points of the vehicle.
The aforementioned identification strategy is applied through three different dynamic analytical models for train vibrations: a half-train multi-body model with 6 degrees of freedom (2 degrees of freedom dedicated to the vertical and pitch motions of the vehicle body and 4 degrees of freedom to describe the vertical and pitch motions of each of the two bogies; the wheels are modeled as massless and directly in contact with the rail profile), a half-train multi-body model with 10 degrees of freedom (2 degrees of freedom dedicated to the vertical and pitch motions of the vehicle body, 4 degrees of freedom to describe the vertical and pitch motions of each of the two bogies and, in conclusion, 4 degrees of freedom for the vertical motions of each wheel of the four axles), and a full-train multi-body model consisting of 17 degrees of freedom (where roll motions of vehicle body, bogies, and axles are also observed).
Finally, experimental measurements, recorded over several runs of a properly armed diagnostic vehicle, have been processed to prove the incredible potential of this brand-new device.

INDEX

1 INTRODUCTION 4
2 CHARACTERIZATION AND IDENTIFICATION OF THE RAIL HEAD'S RUNNING TABLE 5
2.1 RANDOM SIGNALS THEORY 5
2.1.1 STATIONARITY AND ERGODICITY OF A PROCESS 6
2.1.2 PROBABILITY DENSITY FUNCTIONS 8
2.1.3 CORRELATION FUNCTIONS 9
2.1.4 AUTO – POWER SPECTRAL DENSITY 10
2.1.5 BROADBAND AND NARROWBAND RANDOM PROCESSES 13
2.1.6 POWER SPECTRAL DENSITY OF THE DERIVATIVE OF A PROCESS 15
2.1.7 CROSS-POWER SPECTRAL DENSITY 17
2.2 RAIL PROFILES CHARACTERIZATION 19
2.2.1 STANDARD ISO 8608 19
2.2.2 SUSSMAN 24
2.3 SIMULATION OF RAIL PROFILES 26
2.3.1 SIMULATION OF A WHEEL 26
2.3.2 COMPLETE WHEELSET SIMULATION 29
2.4 IDENTIFICATION OF RAIL PROFILES 35
2.4.1 OPERATIONAL MODAL ANALYSIS FOR THE RAIL PROFILES IDENTIFICATION 35
2.4.2 THE GONZALEZ METHOD 39
2.4.3 STANDARD EN 13848 40
3 RAILWAY VEHICLES MODELING 43
3.1 VEHICLE MODELS 44
3.1.1 6 DOF HALF-TRAIN MODEL 44
3.1.2 10 DOF HALF-TRAIN MODEL 46
3.1.3 17 DOF FULL-TRAIN MODEL 50
3.2 DYNAMIC PROBLEM: FREQUENCY DOMAIN RESOLUTION 54
3.2.1 SYSTEM'S OUTPUT PSD 54
3.2.2 RELATIONS BETWEEN INPUT AND OUTPUT 55
3.2.3 WELCH PERIODOGRAM AND HALF SPECTRA METHOD 57
4 IDENTIFICATION THROUGH MODELS' DATA 59
4.1 CASE 1 59
4.1.1 OMA METHOD 59
4.1.2 GONZALEZ METHOD 64
4.2 CASE 2 66
4.2.1 OMA METHOD 66
4.2.2 GONZALEZ METHOD 69
4.3 CASE 3 72
4.3.1 OMA METHOD 72
4.3.2 GONZALEZ METHOD 75
5 EXPERIMENTAL RESULTS: MERMEC'S DIAGNOSTIC VEHICLE 79
5.1 MEASURING SYSTEM DESCRIPTION AND ACQUISITION PARAMETERS 79
5.2 MEASURING SYSTEM DESCRIPTION AND ACQUISITION PARAMETERS 80
5.3 PSD ESTIMATE 82
5.3.1 NON-PARAMETRIC ESTIMATE OF TIME DELAYS 85
5.3.2 NON-PARAMETRIC ESTIMATE OF COHERENCE 86
5.4 INVERSE PROBLEM RESOLUTION THROUGH THE GONZALEZ METHOD 89

5.4.1 CASE 1 89
5.4.2 CASE 2 94
5.5 PROFILE IDENTIFICATION AND LIVE VALIDATION ACCORDING TO EN 13848 97
5.6 PROFILE IDENTIFICATION AND COMPARISON WITH THE OPTICAL SYSTEMS 106
5.6.1 METHODOLOGY 107
5.6.2 CASE 1 107
5.6.3 CASE 2 110
5.6.4 CASE 3 113
6 CONCLUSIONS 116
7 APPENDICES 118
7.1 APPENDIX A 118
7.2 APPENDIX B 120
7.3 APPENDIX C 123
8 REFERENCES 126

1 INTRODUCTION

In land-vehicles literature, many authors dedicated their work at studying the surfaces where these vehicles move on. In railway sector, the rail head irregularities represent one of the principal excitation sources in vehicle dynamic. A proper knowledge about this topic is essential for both the vehicle design and a correct maintenance of railway infrastructures.
During the design step, knowing the stress levels beforehand allows you to adjust the vehicle dynamic behaviour in order to improve the overall dynamic performances, safety, and passengers' comfort. On the other hand, this could be possible only by monitoring the health state of railway infrastructure through a predictive maintenance strategy.
To pursue this aim, there are already several types of diagnostic systems, like those with optical or laser sensors. Unfortunately, all of them share the same narrow "defect": expensiveness.
Therefore, the scope of this work is to find a cheaper but equally effective way to reach the same result through the vibration-based condition monitoring. This strategy has also the merit of keeping a good model robustness even under extreme weather conditions: for example, if the rail head surface is covered by a fair amount of snow, the accelerometers layout will not be affected while all optical systems will turn out unable to properly measure the wanted track properties.
With the method described afterwards, by estimating the excitations coming from the wheel rail interaction and the subsequent response of the whole vehicle model, it will be possible to identify with an acceptable approximation of every rail head surfaces characteristics and then to classify them according to any kind of rail standard.
To hit this target, both theoretical and experimental results are then analysed. First, three multi-body models of a train have been implemented, then the records coming from several runs of a properly armed diagnostic train have been processed. All the experimental data have been recorded through the instrumentation of MerMec S.p.A., member of the Angel Company (https://www.mermecgroup.com/ ; https://www.angelcompany.com/).
Another strength of this vibrational approach, from an industrial point of view, is the possibility to create a modular set of products based on how wide the accelerometer layout is. This work underlines the different potential that exists between a "poor" accelerometers' layout (as the one usually mounted on a diagnostic vehicle) and an "augmented" one.
All experimental results have been studied and verified according to the standard EN 13848, parts 1, 2 and 5 (respectively [18],[19], and [20]).
Finally, starting from the vehicle's accelerations, the estimation of the rail head profile has been validated through a comparison with the same estimation but made by a different technology, i.e., the MerMec's opto-electronic Track Geometry Measuring System (TGMS).

2 CHARACTERIZATION AND IDENTIFICATION OF THE RAIL HEAD'S RUNNING TABLE

The major source of excitation for a train is the one coming from the vehicle interaction with the railway infrastructure. Starting from this phenomenon, it is possible to identify two different parameters that affect the vehicle's dynamic behavior: the spatial trend of the rail-road stiffness and of the track geometry. The former depends on the general basement configuration and, in a more evident way, on the longitudinal sleepers' pitch (that creates a space-periodic stiffness variation in the vehicle support); the latter takes into count all rail-head micro and macro irregularities but also the overall geometric configuration of the railway infrastructure (i.e., track gauge, longitudinal level, cross level, transverse alignment, switches and so on).
Focusing on the rail-head irregularities, the properties of the running surface's roughness could be estimated through the "power spectral density" (PSD) statistical function. This method allows to create a mathematical model of the rail-head irregularities' distribution along any wavelength of interest and then to classify the rail wear levels setting different frequency-amplitude classes.
To validate this kind of estimation, the rail profile needs to be considered as a random and stationary process, therefore its statistical properties do not depend on the considered track length.

2.1 RANDOM SIGNALS THEORY

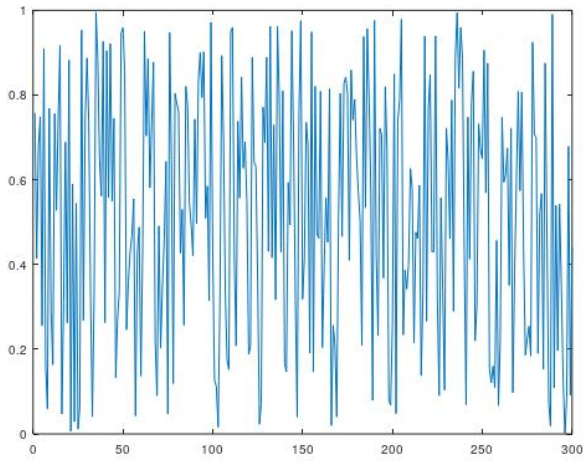

Figure 2.1: Typical time domain realization of a random signal

The system's response to random excitations is also a random phenomenon. Describing a random phenomenon using time functions is not the best approach. Several random phenomena are characterized by statistical regularity, that means they have repetitive patterns and can thus be described in terms of averages. For these reasons it is preferred to describe stochastic phenomena in terms of probability of occurrence rather than in a deterministic way.
Mainly four statistical functions are used to describe the random signals:

- *Root mean square* and *variance*, that provide information about the amplitude of the signal;
- *Probability distributions*, that provide information about the statistical properties of the signal's amplitude;

- *Correlation functions*, that provide information about the statistical properties of the signal in the time domain;

- *Power spectral density functions*, that provide information about the statistical properties of the signal in the frequency domain.

2.1.1 STATIONARITY AND ERGODICITY OF A PROCESS

Let us consider *n* realizations over time of a certain random process $x_1(t), x_2(t), \dots, x_n(t)$, as those shown in the next figure:

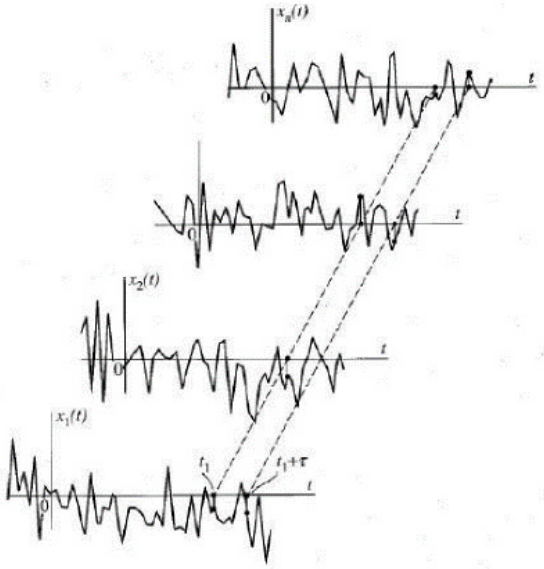

Figure 2.2: Example of *n* different time domain realizations of a random signal (adapted from [11])

Each realization will be different from the others. Therefore, it is not possible to use any of these functions over time to predict a future realization. A single function over time $x_k(t)$ is called *sample function* and can be considered a random variable. The set of all possible realizations over time constitutes the random (or stochastic) process. In such processes it is possible at first to define an *average value* at a given time $t = t_1$; the so-called overall average is obtained:

$$\mu_x(t_1) = \lim_{n\to+\infty} \frac{1}{n} \sum_{k=1}^{n} x_k(t_1). \tag{2.1}$$

The concept of assembly mean is also present within the definition of *auto-correlation function*, by referring again to Figure 2, can be defined as the mean value of the product of the function at time t and at time $t + \tau$:

$$R_{xx}(t_1, t_1 + \tau) = \lim_{n\to+\infty} \frac{1}{n} \sum_{k=1}^{n} x_k(t_1) x_k(t_1 + \tau). \tag{2.2}$$

If the values of $\mu_x(t_1)$ and $R_{xx}(t_1, t_1+\tau)$ depend on the value t_1, then the process will be defined as *non-stationary*. Otherwise, the process can be defined as *stationary*. Consequently, the average value will be time independent, so $\mu_x(t_1) = \mu_x = constant$, and the auto-correlation function will depend only on the τ value, so $R_{xx}(t_1, t_1+\tau) = R_{xx}(\tau)$.
Actually, there is a difference between *weakly stationary* and *strongly stationary* processes but in many practical applications the first one implies the second. It is a class of random processes defined as *random Gaussian processes*.
In general, for the calculation of assembly means, such as the mean value or the autocorrelation function, it is needed to have a large number of sample functions. In some cases, it is possible to refer to a single realization *k* over time, by calculating the average time value and the time domain auto-correlation function as follows:

$$\mu_x(k) = \lim_{T\to+\infty} \frac{1}{T} \int_0^T x_k(t)dt\,; \tag{2.3}$$

$$R_{xx}(k,\tau) = \lim_{T\to+\infty} \frac{1}{T} \int_0^T x_k(t)x_k(t+\tau)dt. \tag{2.4}$$

If the process is stationary and the values of $\mu_x(k)$ and $R_{xx}(k,\tau)$ are the same for any process realization of the process, then the process can be defined as *ergodic*.
Consequently, for an ergodic process:

$$\mu_x(k) = \mu_x = constant; \tag{2.5}$$

$$R_{xx}(k,\tau) = R_{xx}(\tau). \tag{2.6}$$

Ergodicity therefore makes it possible to use a single sample function to calculate the means of a given random process. The *mean square value* of a random variable $x(t)$ is defined as the quantity:

$$\psi^2{}_x = \lim_{T\to+\infty} \frac{1}{T} \int_0^T x^2(t)dt. \tag{2.7}$$

The square root of the mean square value is denoted by RMS (*root mean square value*).
We have seen how μ_x is constant for an ergodic process. In vibrations it is possible to consider the mean value μ_x as the static component of $x(t)$ and the quantity $x(t) - \mu_x$ as the dynamic component. The latter is represented by the *variance*, defined as follows:

$$\sigma^2{}_x = \lim_{T\to+\infty} \frac{1}{T} \int_0^T [x(t) - \mu_x]^2 dt. \tag{2.8}$$

Its root square value is known as standard deviation. It can be easily proved that:

$$\sigma^2{}_x = \psi^2{}_x - \mu^2{}_x. \tag{2.9}$$

2.1.2 PROBABILITY DENSITY FUNCTIONS

It has been shown that in the case of an ergodic random process it is possible to use a single assembly function to describe it in terms of averages. The *probability density function* allows you to collect information concerning a random variable in terms of amplitude.
The expected value (or average value) of a function $x(t)$ is given by:

$$E[x(t)] = \frac{1}{T}\int_0^T x(t)dt = \int_{-\infty}^{+\infty} xp(x)dx, \tag{2.10}$$

where $p(x)$ is the *probability density function*. In other words, it represents probability $p\,(x)\,dx$ that a random variable falls within the interval $[x\,;\ x + dx]$. Consequently, for a stationary process (i.e. time-invariant), we have that $E\,[x\,(t)] = E\,[x]$.
Similarly, since the root mean square value is the expected value of x^2, we have:

$$E[x^2] = \frac{1}{T}\int_0^T x^2 dt = \int_{-\infty}^{+\infty} x^2 p(x)dx. \tag{2.11}$$

The integrals in equations (2.10) and (2.11) are approximated considering that, for a value of *T* sufficiently large, all values between *0* and *T* are equally probable and therefore $dt/T \sim p(x)dx$.
According to what we saw in the previous section, the square root of $E[x^2]$ is the *RMS*. The standard deviation σ of $x(t)$ and the variance σ^2 are defined by:

$$\sigma^2 = E[x^2] - (E[x])^2. \tag{2.12}$$

If the signals are digitally recorded the mean value, the mean square value and the variance can be obtained directly from the time history of the random signal $x(t)$:

$$E[x] = \lim_{N\to+\infty} \frac{1}{N}\sum_{i=1}^{N} x_i(t)\,; \tag{2.13}$$

$$E[x^2] = \lim_{N\to+\infty} \frac{1}{N}\sum_{i=1}^{N} x^2{}_i(t). \tag{2.14}$$

where *N* is the number of assemblies.

2.1.3 CORRELATION FUNCTIONS

The auto-correlation function for a random signal $x\,(t)$ provides information about the degree of dependence of a value of x at a time t with respect to its assumed value at a time $t + \tau$. In section 2.1.1 we have seen how for a stationary random signal, the function of autocorrelation depends only on τ and it is independent from the absolute time.
By expanding the definition given by equation (2.4) we have:

$$R_{xx}(\tau) = E[x(t)x(t+\tau)] = \lim_{T\to+\infty} \frac{1}{T}\int_0^T x(t)x(t+\tau)dt, \qquad (2.15)$$

where $p\,(x)\,dx = dt/T$ has been set, that is, for a sufficiently large value of T, all values of the random signal $x\,(t)$ have the same probability of falling within the interval $[0;\ T]$.

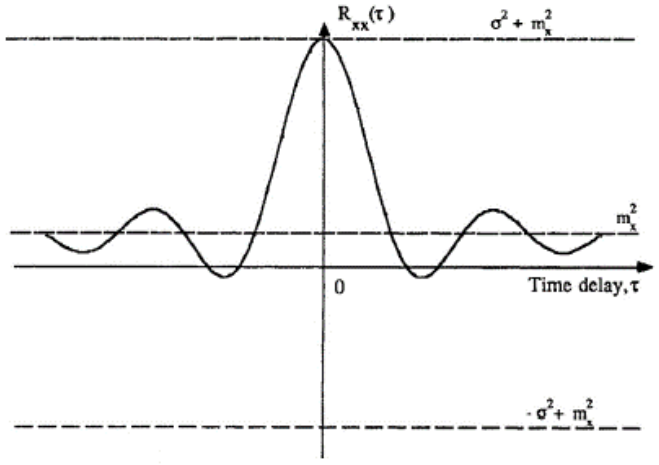

Figure 2.3:An example of the auto-correlation function (adapted from [14])

An example of the auto-correlation function is shown in Figure 2.3. It is possible to normalize a correlation function through a correlation coefficient, defined as:

$$\rho_{xx} = \frac{E[(x(t_1) - m_x)(x(t_2) - m_x)]}{\sigma_x \sigma_x} = \frac{R_{xx}(\tau) - m_x^2}{\sigma_x^2}, \qquad (2.16)$$

where m_x is the signal mean value.
For $\tau \to 0 => \rho_{xx} \to 1$, being $R_{xx}(0) = E[x^2] = \sigma_x^2 - m_x^2$. For $\tau \to \infty => \rho_{xx} \to 0$, because $R_{xx}(\infty) \to m_x^2$. The auto-correlation function is an even function and assumes its maximum value for $\tau = 0$. $R_{xx}(\tau)$ is periodic for periodic signals and decays to 0 for random signals at large values of the delay τ.
Now consider two different stationary random signals $x\,(t)$ and $y\,(t)$. The *cross-correlation function* between the two signals provides information about the similarity between them in function of the time shift τ, and it is defined as:

$$R_{xy}(\tau) = E[x(t)y(t+\tau)] = \lim_{T\to+\infty} \frac{1}{T}\int_0^T x(t)y(t+\tau)dt. \qquad (2.17)$$

Figure 2.4 shows an example of the cross-correlation function.

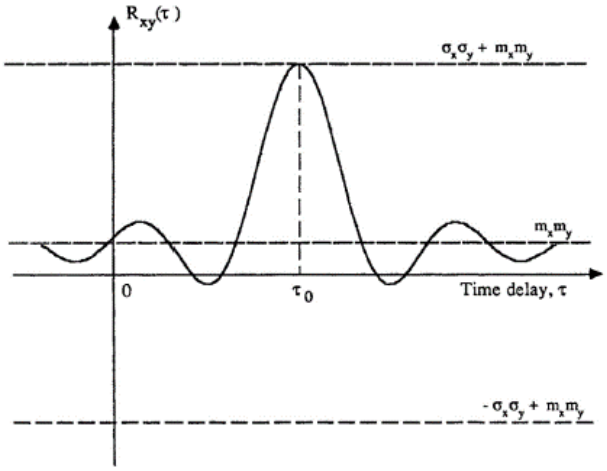

Figure 2.4: An example of the cross-correlation function (adapted from [14])

For each pair of random and stationary signals, we can define two cross-correlation functions:

$$\begin{aligned} R_{xy}(\tau) &= E[x(t)y(t+\tau)], \\ R_{yx}(\tau) &= E[y(t)x(t+\tau)]; \end{aligned} \tag{2.18}$$

Moreover, being these processes defined as stationary, it is also true that:

$$\begin{aligned} R_{xy}(\tau) &= E[x(t-\tau)y(t)] = R_{yx}(-\tau), \\ R_{yx}(\tau) &= E[y(t-\tau)x(t)] = R_{xy}(-\tau). \end{aligned} \tag{2.19}$$

Differently from the auto-correlation function, because $R_{xy}(\tau) = R_{yx}(-\tau)$the cross-correlation function is not an even function of τ.

2.1.4 AUTO – POWER SPECTRAL DENSITY

The autocorrelation function provides information about the properties of a random variable in the time domain. On the other hand, the PSD (*power spectral density function*) provides the same type of information in the frequency domain. The spectral density function is the Fourier transform of the correlation function. Let $x\,(t)$ be the representative assembly function of an ergodic random process. Indicating with $X\,(\omega)$ the Fourier transform of the function $x\,(t)$, we have:

$$X\,(\omega) = \frac{1}{2\pi}\int_{-\infty}^{+\infty} x(t)e^{-i\omega t}dt, \tag{2.20}$$

and

$$x(t) = \int_{-\infty}^{+\infty} X\,(\omega)e^{i\omega t}d\omega. \tag{2.21}$$

Note that $X\ (\omega)$ is a complex quantity.
The classical Fourier analysis introduces the following condition:

$$\int_{-\infty}^{+\infty} |x(t)|dt < \infty, \tag{2.22}$$

and so it is valid for any function whose absolute value is integrable and tends to *0* for$|t| \to \infty$. Since stationary random signals do not respect this last condition unlike the correlation functions (we have seen how the correlation function of a random signal tends to *0* as τ increases), that's why the latter are used for the Fourier analysis; in this way we have:

$$S_{xx}(\omega) = \frac{1}{2\pi}\int_{-\infty}^{+\infty} R_{xx}(\tau)e^{-i\omega\tau}d\tau, \tag{2.23}$$

and

$$R_{xx}(\tau) = \int_{-\infty}^{+\infty} S_{xx}(\omega)e^{i\omega\tau}d\omega. \tag{2.24}$$

$S_{xx}(\omega)$ represent the auto-power spectral density of $x(t)$.
One of its most important properties can be underlined setting $\tau = 0$ in the equation (2.24):

$$R_{xx}(\tau = 0) = \int_{-\infty}^{+\infty} S_{xx}(\omega)d\omega. \tag{2.25}$$

Considering the definition given by equation (2.15), we obtain:

$$E[x^2] = R_{xx}(\tau = 0) = \int_{-\infty}^{+\infty} S_{xx}(\omega)d\omega. \tag{2.26}$$

So, as it is shown in the next figure, the mean square value of a random and stationary process can be given by the area under the curve of the ω-dependent power spectral density.

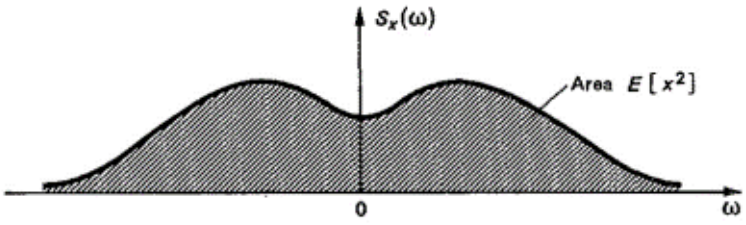

Figure 2.5: The graphic explanation of the $E[x^2]$ value matching the area under the $S_{xx}(\omega)$ curve (adapted from [12])

It is proved now that $S_{xx}(\omega)$is a real and even function. The complex value of a Fourier transform function can be split into real and imaginary part:

$$X\ (\omega) = A\ (\omega) - iB\ (\omega), \tag{2.27}$$

Applying the same definition to the PSD:

$$S_{xx}(\omega) = A\,(\omega) - iB\,(\omega), \tag{2.28}$$

where

$$A\,(\omega) = \frac{1}{2\pi}\int_{-\infty}^{+\infty} R_{xx}(\tau)\cos(\omega\tau)\,d\tau, \tag{2.29}$$

and

$$B\,(\omega) = \frac{1}{2\pi}\int_{-\infty}^{+\infty} R_{xx}(\tau)\sin(\omega\tau)\,d\tau, \tag{2.30}$$

Since $R_{xx}(\tau)$ is an even function of τ and $sin\,(\omega\tau)$ is an odd function, their product is an odd function and for this reason we have that the integral in (2.30) in the range $[-\infty;\ 0]$ is exactly equal and of opposite sign to its value in the range $[\,0; +\infty]$. Therefore, $B\,(\omega)$ is null and so the PSD is defined as:

$$S_{xx}(\omega) = A\,(\omega). \tag{2.31}$$

Moreover, according to (2.29), it is a real and even function of ω, and it is always non-negative.

There are two alternative but equivalent ways to define the same PSD. In figure 2 .6a we have the so-called *double-sided spectral density function*, defined in the interval $[-\infty;\ +\infty]$. Figure 2.6b shows the same PSD in the form of *one-sided spectral density function* (also called *half spectrum*), defined in the interval $[\,0; +\infty]$.

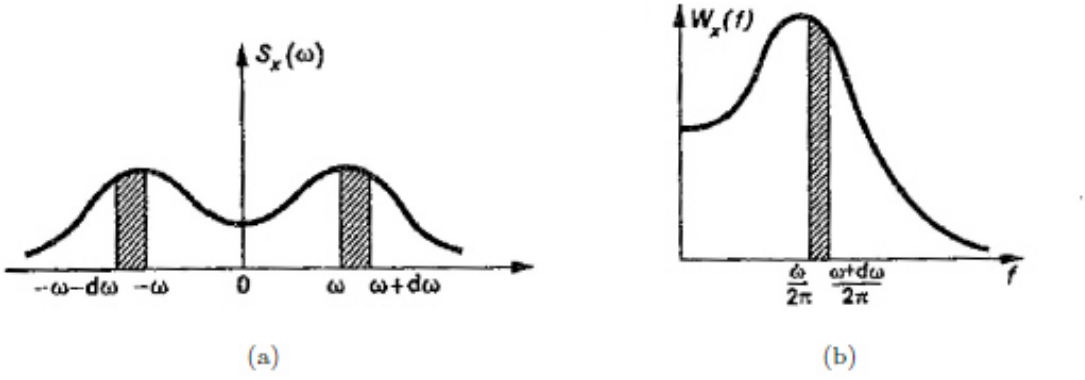

Figure 2.6: Double-sided (a) and one-sided (b) spectral density function (adapted from [12])

By referring on the previous figure and according to (2.26), which states:

$$E[x^2] = \int_{-\infty}^{+\infty} S_x(\omega)d\omega, \tag{2.32}$$

it follows:

$$E[x^2] = \int_0^{+\infty} W_x(f)df, \tag{2.33}$$

where f is the frequency in *Hz*. The band $[\omega; \omega + d\omega]$ in rad/s in figure 2.6a corresponds to the band $[\frac{\omega}{2\pi}; \frac{\omega+d\omega}{2\pi}]$ in *Hz* in figure 2.6b; therefore, because of the hatched areas in the two figures must be equal according to (2.32) and (2.33), it follows that:

$$2S_x(\omega)d\omega = W_x\left(f = \frac{\omega}{2\pi}\right)\frac{d\omega}{2\pi}. \tag{2.34}$$

In conclusion, the half-spectrum is linked to the continuous-spectrum by the following relations:

$$\begin{aligned} W_x\left(f = \frac{\omega}{2\pi}\right) &= 4\pi S_x(\omega); \\ W_x(f) &= 4\pi S_x(\omega = 2\pi f). \end{aligned} \tag{2.35}$$

2.1.5 BROADBAND AND NARROWBAND RANDOM PROCESSES

We have seen how the PSD function provides information about a random process in the frequency domain. In particular, the random processes can be divided into random processes with a *narrowband of frequencies* and a *broadband of frequencies*. In the first case, $S_x(\omega)$ has significant values only for a narrow band of frequencies with the peak-frequency at its centre. In the second case $S_x(\omega)$ assumes significant values for a wider range of frequencies. The two extreme cases are:

- spectrum consisting of two symmetrical delta functions with respect to the ordinate axis, corresponding to a sinusoidal assembly function;
- spectrum consisting of a uniform function, corresponding to an assembly function in which all frequencies are equally represented.

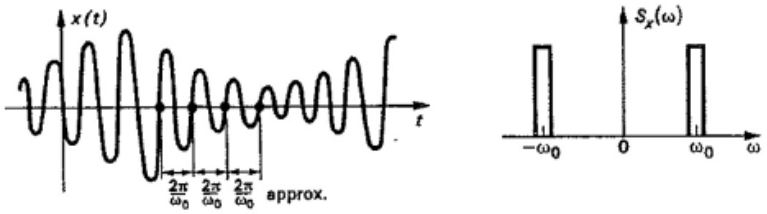

(a) *Storico di una funzione d'assieme di un processo a banda stretta*

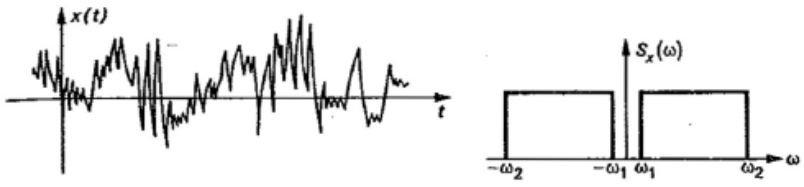

(b) *Storico di una funzione d'assieme di un processo a banda larga*

Figure 2.7: Examples of a narrowband assembly function (a) and a broadband assembly function (b) (adapted from [12])

With reference to figure 2.7b, in the broadband process limit case, when $\omega_1 = 0$ and $\omega_2 \to \infty$, we refer to the *ideal white noise*. Basing on (2.26), the root mean square value of a random process consisting of an ideal white noise would be infinite, that is the reason why it is only a theoretical concept.
However, if we consider a broadband noise that extends well beyond the frequencies of interest, we can talk about white noise or *narrow-band white noise*.
The shape of the autocorrelation function of a white noise can be obtained with simple steps. In general, from (2.26) we have that:

$$E[x^2] = \int_{-\infty}^{+\infty} S_x(\omega) d\omega = 2S_0(\omega_2 - \omega_1),$$

where S_0 is the constant amplitude peak value of $S_x(\omega)$. From the (2.24) and, because the $S_x(\omega)$ is an even function in ω, it results that:

$$\begin{aligned} R_x(\tau) \quad &= \int_{-\infty}^{+\infty} S_x(\omega) e^{i\omega\tau} d\omega = \int_{-\infty}^{+\infty} S_x(\omega) \cos(\omega\tau)\, d\omega = \\ &= 2\int_{\omega_1}^{\omega_2} S_0 \cos(\omega\tau)\, d\omega = \\ &= 2S_0 \left[\frac{1}{\tau}\sin(\omega\tau)\right]_{\omega_1}^{\omega_2} = \\ &= \frac{2S_0}{\tau}(\sin(\omega_2\tau) - \sin(\omega_1\tau)) = \\ &= \frac{4S_0}{\tau}\cos\left[\left(\frac{\omega_1 + \omega_2}{2}\right)\tau\right] \cdot \sin\left[\left(\frac{\omega_2 - \omega_1}{2}\right)\tau\right]. \end{aligned}$$

Setting now $\omega_1 = 0$, we obtain:

$$R_x(\tau) = \frac{4S_0}{\tau}\cos\frac{\omega_2\tau}{2}\sin\frac{\omega_2\tau}{2} = 2S_0\frac{\sin(\omega_2\tau)}{\tau}.$$

This function is represented in figure 2.8a. Moreover, setting $\omega_2 \to \infty$ the curve is reduced to a single vertical peak with zero width, infinite hight and finite area (that could be easily demonstrated to be equal to $2\pi S_0$), as shown in figure 2.8b.

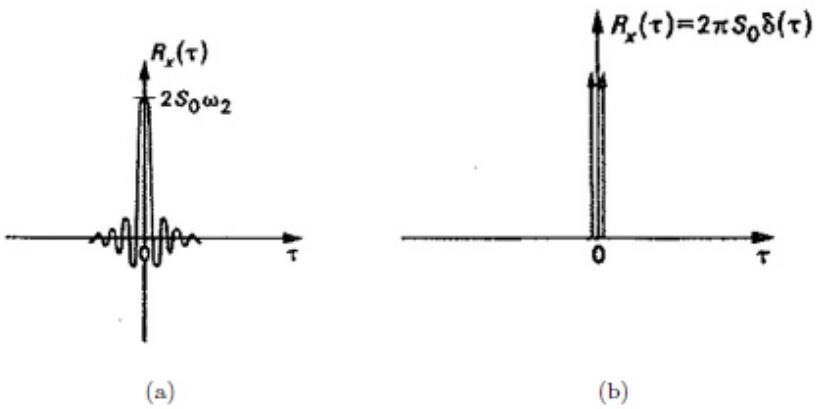

Figure 2.8: Auto-correlation functions of a generic signal (a) and of a white noise (b) (adapted from [12])

To mathematically describe this behaviour we can use the *Dirac delta function* $\delta(\tau)$, which is defined as null everywhere except in $\tau = 0$ where it is infinite:

$$\int_{-\infty}^{+\infty} \delta(\tau) d\tau = 1.$$

To be more generic, the function $\delta(\tau - T)$ is null everywhere except in $\tau = T$; denoting by $g(\tau)$a generic continuous function of τ we have that:

$$\int_{-\infty}^{+\infty} \delta(\tau - T) g(\tau) d\tau = g(\tau = T). \tag{2.36}$$

In this way the autocorrelation function for a white, random, and stationary signal with spectral density S_0 will be:

$$R_x(\tau) = 2\pi S_0 \delta(\tau), \tag{2.37}$$

and therefore, as we have seen in figure 2.8b, $R_x(\tau)$ is null everywhere except in $\tau = 0$ where it assumes an infinite value. The area subtended by $R_x(\tau)$ is then equal to $2\pi S_0$.

2.1.6 POWER SPECTRAL DENSITY OF THE DERIVATIVE OF A PROCESS

Let us assume that we know the PSD $S_x(\omega)$ of the stationary random process $x(t)$. Starting from this, it is possible to calculate the power spectral density of processes derived from the first, e.g., speed ($S_{\dot{x}}(\omega)$) and acceleration ($S_{\ddot{x}}(\omega)$). The assembly autocorrelation function of the process $x(t)$ can be written as:

$$R_x(\tau) = E[x(t)x(t+\tau)] = \lim_{N \to +\infty} \frac{1}{N} \sum_{k=1}^{N} x_k(t) x_k(t+\tau).$$

Differentiating with respect to τ, we have:

$$\frac{dR_x(\tau)}{d\tau} = \lim_{N \to +\infty} \frac{1}{N} \sum_{k=1}^{N} \frac{d}{d\tau} [x_k(t) x_k(t+\tau)]. \tag{2.38}$$

Knowing that:

$$\begin{aligned} \frac{d}{d\tau}[x_k(t)x_k(t+\tau)] &= x_k(t) \frac{d}{d\tau} x_k(t+\tau) = \\ &= x_k(t) \frac{d}{d(t+\tau)} x_k(t+\tau) \cdot \frac{d(t+\tau)}{d\tau} = \\ &= x_k(t) \dot{x}_k(t+\tau); \end{aligned}$$

We obtain:

$$\frac{d}{d\tau}\big(R_x(\tau)\big) = E[x(t)\dot{x}(t+\tau)]. \tag{2.39}$$

For a stationary process, we know that the assembly means are independent of time t, so:

$$\frac{d}{d\tau}\big(R_x(\tau)\big) = E[x(t)\dot{x}(t+\tau)] = E[x(t-\tau)\dot{x}(t)], \tag{2.40}$$

Differentiating one more time with respect to τ, we have:

$$\frac{d^2}{d\tau^2}\big(R_x(\tau)\big) = -E[\dot{x}(t-\tau)\dot{x}(t)] = -R_{\dot{x}}(\tau), \tag{2.41}$$

where $R_{\dot{x}}(\tau)$ is the autocorrelation function of $\dot{x}(t)$.

The integral in the equation (2.24),

$$R_x(\tau) = \int_{-\infty}^{+\infty} S_x(\omega)e^{i\omega\tau}d\omega,$$

is defined with respect toω, with τ kept constant and with the integration limits independent of τ. Therefore it is possible to differentiate with respect to τ inside the integral sign, obtaining:

$$\frac{d}{d\tau}\big(R_x(\tau)\big) = \int_{-\infty}^{+\infty} i\omega S_x(\omega)e^{i\omega\tau}d\omega, \tag{2.42}$$

and

$$\frac{d^2}{d\tau^2}\big(R_x(\tau)\big) = -\int_{-\infty}^{+\infty} \omega^2 S_x(\omega)e^{i\omega\tau}d\omega. \tag{2.43}$$

Combining now the equations (2.41) and (2.43), it is possible to express the autocorrelation function of the derivative of a process as:

$$R_{\dot{x}}(\tau) = \int_{-\infty}^{+\infty} \omega^2 S_x(\omega)e^{i\omega\tau}d\omega. \tag{2.44}$$

But it is also true that $R_{\dot{x}}(\tau)$ can be identified as the inverse transform of $S_{\dot{x}}(\omega)$, so:

$$R_{\dot{x}}(\tau) = \int_{-\infty}^{+\infty} S_{\dot{x}}(\omega)e^{i\omega\tau}d\omega. \tag{2.45}$$

In conclusion, combining the equation (2.44) and (2.45), we obtain:

$$S_{\dot{x}}(\omega) = \omega^2 S_x(\omega); \tag{2.46}$$

So the PSD of a process $\dot{x}(t)$ can be easily obtained by multiplying by ω^2 the PSD of the known $x(t)$.

The obtained results allow us to also calculate the following values:

$$E[\dot{x}^2] = \int_{-\infty}^{+\infty} S_{\dot{x}}(\omega)d\omega = \int_{-\infty}^{+\infty} \omega^2 S_x(\omega)d\omega, \tag{2.47}$$

and

$$E[\ddot{x}^2] = \int_{-\infty}^{+\infty} S_{\ddot{x}}(\omega)d\omega = \int_{-\infty}^{+\infty} \omega^4 S_x(\omega)d\omega. \tag{2.48}$$

2.1.7 CROSS-POWER SPECTRAL DENSITY

For consistency with what we have seen with the auto-power spectral density of a process $x(t)$, if we consider a pair of processes $x(t)$ and $y(t)$ we have two cross-correlations ($R_{xy}(\tau)$ and $R_{yx}(\tau)$) and the relative cross-power spectral densities are obtained as follows:

$$S_{xy}(\omega) = \frac{1}{2\pi}\int_{-\infty}^{+\infty} R_{xy}(\tau)e^{-i\omega\tau}d\tau, \tag{2.49}$$

and

$$S_{yx}(\omega) = \frac{1}{2\pi}\int_{-\infty}^{+\infty} R_{yx}(\tau)e^{-i\omega\tau}d\tau. \tag{2.50}$$

According to equation (2.19), the cross-correlation functions are linked together. Setting now $R_{xy}(\tau) = R_{yx}(-\tau)$ in the (2.49), we obtain:

$$S_{xy}(\omega) = \frac{1}{2\pi}\int_{-\infty}^{+\infty} R_{yx}(-\tau)e^{-i\omega\tau}d\tau,$$

Therefore, setting $\tau' = -\tau$:

$$S_{xy}(\omega) = \frac{1}{2\pi}\int_{-\infty}^{+\infty} R_{yx}(\tau')e^{i\omega\tau'}(-d\tau') = \frac{1}{2\pi}\int_{+\infty}^{-\infty} R_{yx}(\tau')e^{i\omega\tau'}d\tau' \tag{2.51}$$

So it is equal to (2.50) except for the sign of $i\omega$. Now, according to (2.27), we have:

$$S_{xy}(\omega) = A(\omega) - iB(\omega),$$

and

$$S_{yx}(\omega) = C(\omega) - iD(\omega),$$

Where $A\ (\omega)$, $B\ (\omega)$, $C\ (\omega)$ and $D\ (\omega)$ are real function of ω. By comparing the equations (2.49) and (2.51) we obtain:

$$A(\omega) = C(\omega)$$

and

$$B(\omega) = -D(\omega)$$

since the definite integrals are independent of the integration variables. Consequently $S_{xy}(\omega)$ and $S_{yx}(\omega)$ are equal except for the opposite sign of the imaginary part. In other words, $S_{xy}(\omega)$ is the complex conjugate of $S_{yx}(\omega)$ and vice versa:

$$\begin{aligned} S_{xy}(\omega) &= S_{yx}^{*}(\omega) \\ S_{yx}(\omega) &= S_{xy}^{*}(\omega) \end{aligned} \tag{2.52}$$

There is an interesting property of the cross-power spectral densities, which concerns the case in which the two signals $x(t)$ and $y(t)$ (two realizations of random and ergodic processes) are equal to each other but out of phase by a certain time T, that is:

$$y(t+T) = x(t).$$

Let us also assume that these are white noises, whose auto-correlation function, as we have seen, is just the Dirac delta function in zero. By cross-correlating the two signals, it is possible to observe what happens in terms of cross-spectral densities. In particular, the Dirac delta function will be out of phase with the time T (figure 2.9).

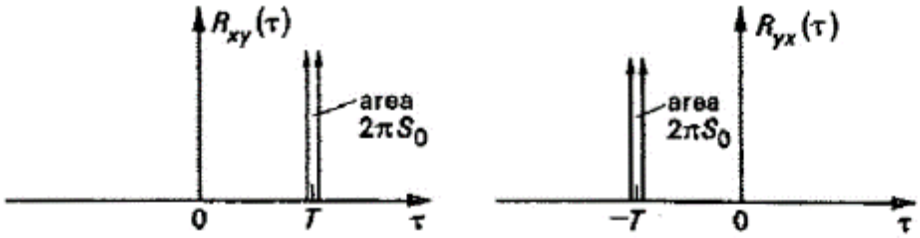

Figure 2.9: Cross-correlation functions for out of phase white noises (adapted from [12])

Starting from (2.49), we can obtain:

$$S_{xy}(\omega) = \frac{1}{2\pi}\int_{-\infty}^{+\infty} 2\pi S_0 \delta(\tau - T) e^{-i\omega\tau} d\tau = S_0 e^{-i\omega T} \tag{2.53}$$

while from (2.50) we obtain:

$$S_{yx}(\omega) = \frac{1}{2\pi}\int_{-\infty}^{+\infty} 2\pi S_0 \delta(\tau + T) e^{-i\omega\tau} d\tau = S_0 e^{i\omega T} \tag{2.54}$$

that is a further confirm of the (2.52). Setting now $S_{xy}(\omega) = A\ (\omega) - iB\ (\omega)$:

$$A(\omega) = S_0 cos(\omega t)$$

$$B(\omega) = S_0 sin(\omega t)$$

So it is possible to represent the modulus $\left|S_{xy}(\omega)\right|$ and phase $\theta = \tan^{-1}[B(\omega)/A(\omega)]$ as shown in the next figure.

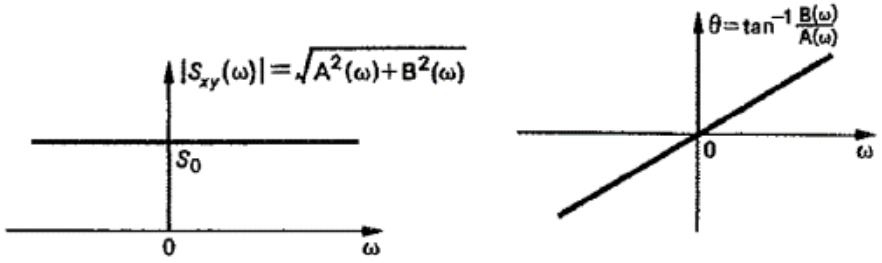

Figure 2.10: Modulus and phase representation for out of phase white noises cross-PSD (adapted from [12])

In particular, the trend of phase θ is represented by a straight line, whose angular coefficient is precisely the delay time T. In the case of a non-white noise, such as the cases analyzed in this PhD thesis, also if some relations change slightly, a very similar trend is expected.

2.2 *RAIL PROFILES CHARACTERIZATION*

In the literature there are many approximations that allow to characterize the road profiles by means of PSD, that makes it possible to cover a wide range of road types. The ISO 8608:2016 standard provides a general method for characterizing road surfaces.
The road profile can be described based on:

- PSD of its vertical displacement;
- PSD of acceleration, i.e. in terms of speed which the slope of the road surface varies per unit of distance travelled.

For the graphic representation of the PSDs it is possible to use a double-logarithmic scale in the spatial frequency $n\ [cycles/m]$ (or angular spatial frequency $\Omega = 2\pi n\ [rad/m]$) or alternatively in the temporal frequency $f\ [Hz]$ (or angular frequency $\omega = 2\pi f\ [rad/s]$). The relationship between the PSD of the displacements and that of the accelerations is the following:

$$G_{acc}(n) = (2\pi n)^4 G_s(n). \tag{2.55}$$

2.2.1 STANDARD ISO 8608

ISO 8608: 2016 provides the means to roughly characterize specific road profiles in order to facilitate their subdivision into general classes, using Fourier analysis. A general classification is also provided.
As previously mentioned, it is possible to measure the roughness of road surfaces using suitable measuring instruments. When reporting PSDs of measured surfaces, they should be limited to the spatial frequency range permitted by the measuring equipment. In general, as regards the lower limit, generally they are not performed below a spatial frequency $n_{min} = 0.01\ [cycles/m]$; the recommended upper limit is instead of $n_{max} = 10\ [cycles/m]$.

The ISO 8608 procedure consists first of all in the estimation of the PSD of the road/track profile; to do this, it is possible to use the *Welch Periodogram* method, which will be better specified later, by windowing the signal appropriately (for example with the *Hanning* window). This method is based on the calculation of the FFT (*Fast Fourier Transform*) of the road profile. The FFT is an algorithm that allows to calculate the *discrete Fourier transform*, therefore in the case in which the starting signal is discrete. The windowing operation, as will be seen below, allows to contain the so-called *leakage* phenomenon.
Because of, if the PSDs are calculated using a constant bandwidth method, in their representation in a double logarithmic diagram it is possible to see at high frequencies the fluctuations generated by the real power distribution and by the noise present, it is convenient to use a smoothed form (*smoothed PSD*) to represent them, for example considering the assumed value in the following value bands:

- Single octave bands, from the lowest frequency measured (except 0) up to a central frequency of 0.0312 $[cycles/m]$;
- One third of octave bands, from the last octave band up to a central frequency of 0.25$[cycles/m]$;
- For the remaining frequency range, one twelfth of octave bands up to the highest frequency measured.

This process is defined as a *smoothing* process. At this point, a fitting of the *smoothed PSD* is performed. The general formula is the following:

$$G_d(n) = G_d(n_0)(n/n_0)^{-w}. \tag{2.56}$$

where $G_d(n)$ indicates the PSD of the vertical displacements (sometimes referred to in the literature as the *irregularity indexC*), $n_0 = 0.1\ [cycles/m]$ is the spatial reference frequency and $w = 2$ is the exponent of the fitting (in some cases referred to as *waviness*). Therefore, using this procedure it is possible to describe the entire frequency content by means of only two parameters: n_0 and w. According to the value assumed by the parameter $G_d(n_0)$, the roughness profiles are cataloged as belonging to one of the 8 classes (from A to H) defined in ISO 8608; the values of this parameter according to the corresponding class are shown in table 2.1.

Class	Roughness Level		
	Lower Limit	Geometric Mean $G_d(n_0)$ $10^{-6}m^3$	Upper Limit
A	-	16	32
B	32	64	128
C	128	256	512
D	512	1024	2048
E	2048	4094	8192
F	8192	16384	32768
G	32768	65536	131072
H	131072	262144	-

Table 2.1: Profiles classification according to ISO 8608 [17]

The graph of figure 2.11 shows the limits of the different classes. To report the limits of the different classes as a function of the temporal frequency, it is possible to use the relation:

$$f = 2\pi\omega = n \cdot u,$$

with u the constant vehicle speed. In this way it is possible to graphically represent the classification for a given speed, as in the graph of figure 2.12, in which the temporal frequencies are shown on the abscissas.

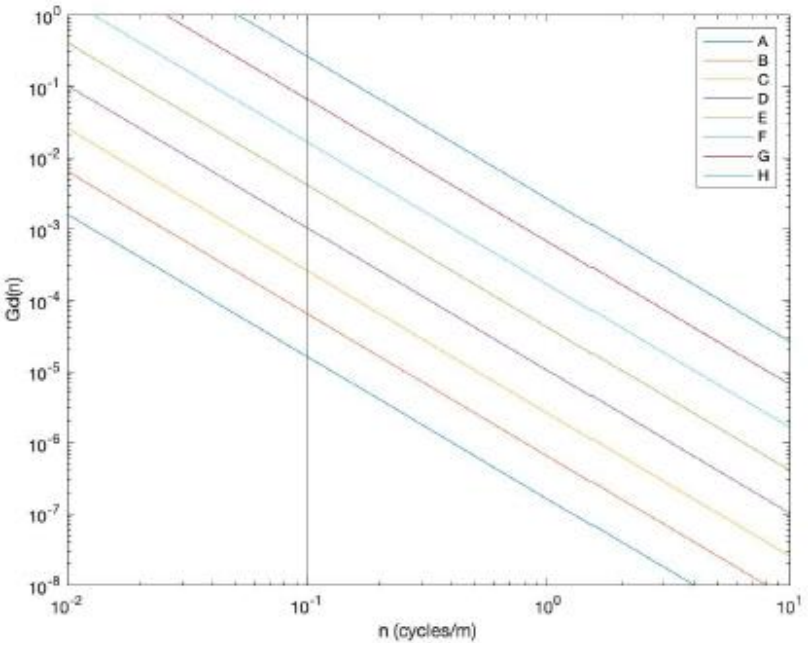

Figure 2.11: Graphic profiles classification according to ISO 8608

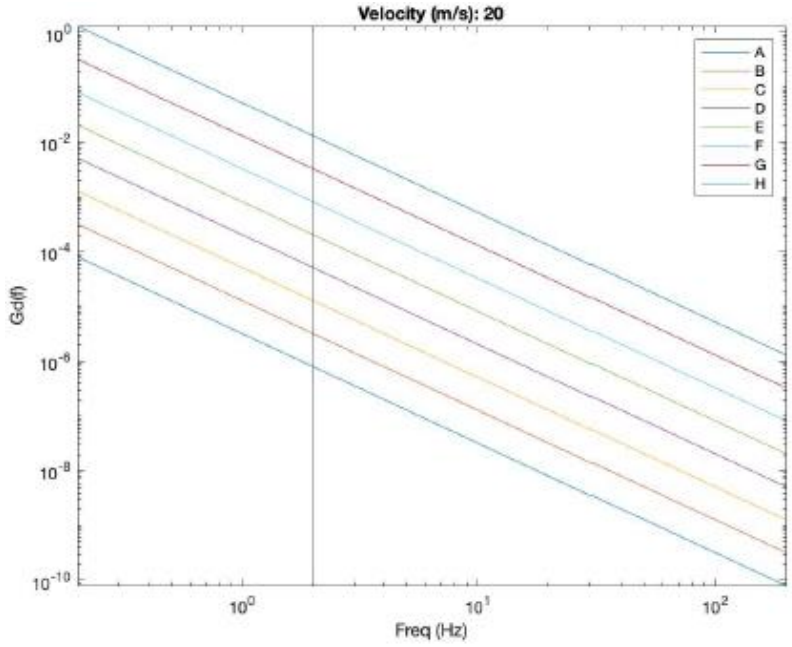

Figure 2.12: Graphic profiles classification according to ISO 8608 for a vehicle speed of 20 m/s

In the same way, once a class has been set, it is possible to plot the PSDs at different speed values in a same graph, as in figure 2.13.

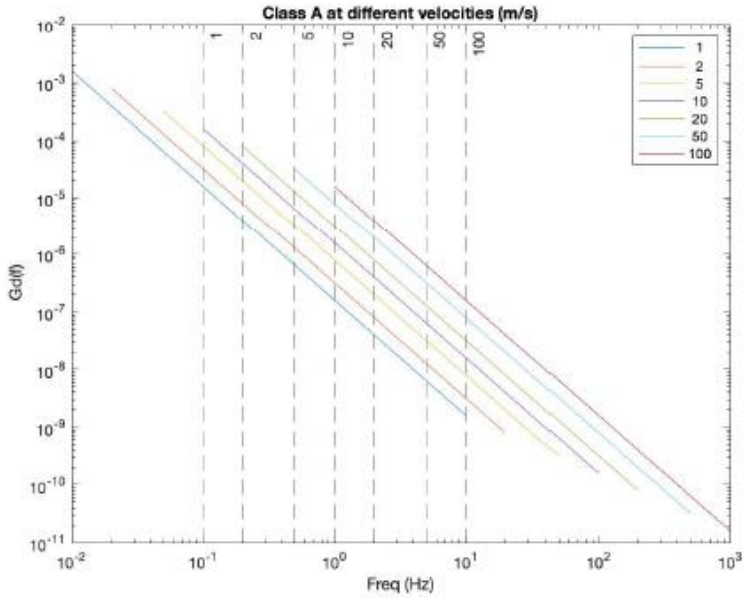

Figure 2.13: Class A PSD profiles according to ISO 8608 for different vehicle speed values

There are also other possible formulas to use alternatively to (2.56). One example could be the following bi-linear function (figure 2.14 and 2.15):

$$G_d(n) = \begin{cases} G_d(n_0)(2\pi n)^{-2}, & for\ n \leq \dfrac{1}{2\pi} \\ G_d(n_0)(2\pi n)^{-1.5}, & for\ n > \dfrac{1}{2\pi} \end{cases} \tag{2.57}$$

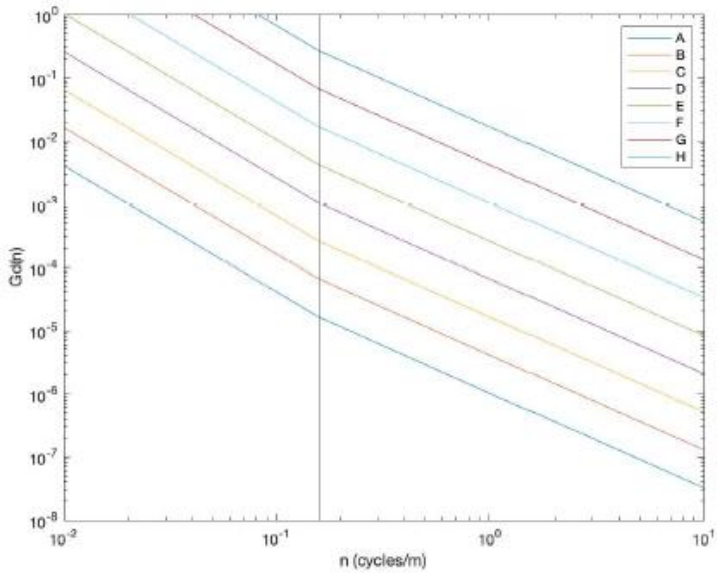

Figure 2.14: Bi-linear profiles classification according to ISO 8608

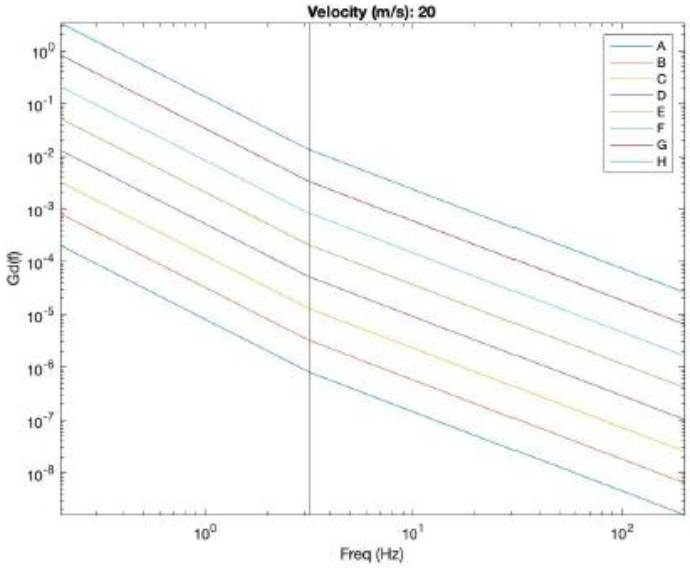

Figure 2.15: Bi-linear profiles classification according to ISO 8608 for a vehicle speed of 20 m/s

Finally, another type of classification is that proposed by the United States Federal Railroad Administrations (FRA), specifically designed for the profiles of railway tracks [8]:

$$G_d(n) = \frac{An_2^2(n^2 + n_1^2)}{n^4(n^2 + n_2^2)}. \tag{2.58}$$

The next figures show the graphic representation of the FRA classification:

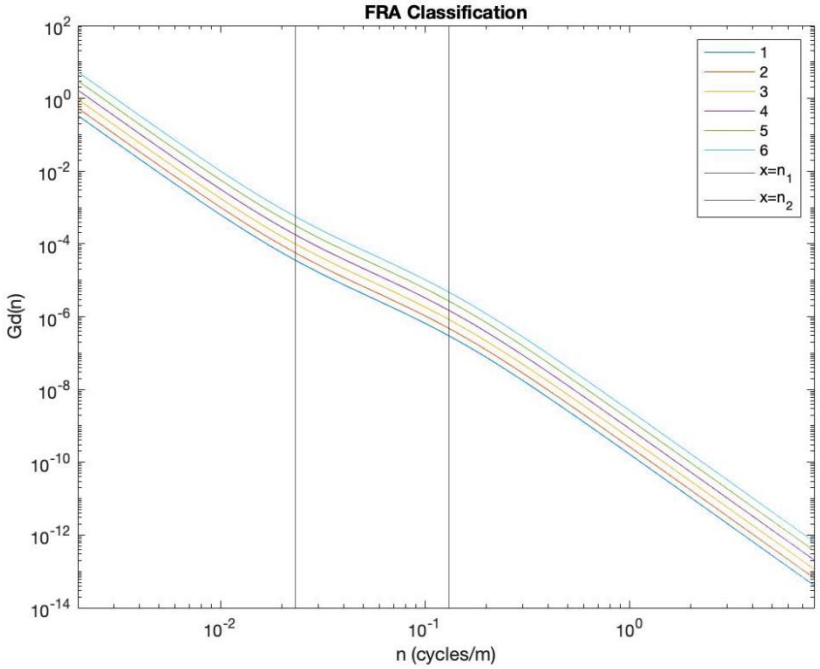

Figure 2.16: Profiles classification according to FRA

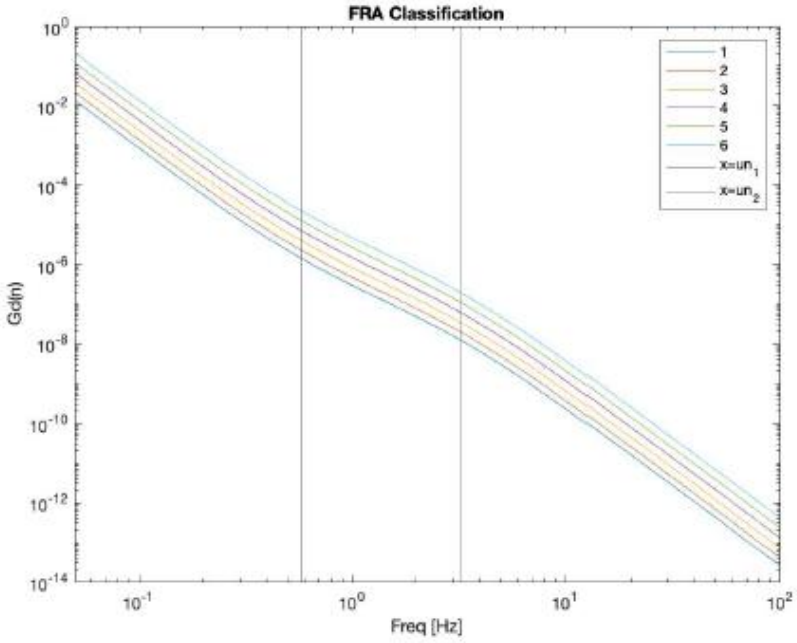

Figure 2.17: Profiles classification according to FRA for a vehicle speed of 25 m/s

2.2.2 SUSSMAN

Among all the approximations seen above, the most suitable for the description of railway profiles is certainly (2.58). In this regard, another approximation often used in the case of railway tracks is the one developed by Sussman (1974):

$$G_d(n) = \frac{G_d(n_0)}{n^2 + n_0^2}. \tag{2.59}$$

To obtain the subdivision into different classes, the value of $G_d(n_0)$ is based on the variance, so that for each class its value, therefore the area under the curve according to (2.26), in the range of frequency $[0.011; 2.83]$ $[cycles/m]$ is equal to the one calculated for (2.56). Therefore we have:

$$\sigma^2 = \int_{n_{inf}}^{n_{sup}} G_d(n)dn = G_d(n_0)\left[\frac{\tan^{-1}\left(\frac{n}{n_0}\right)}{n_0}\right]_{n_{inf}}^{n_{sup}} = G_d(n_0)\left[\frac{\tan^{-1}\left(\frac{n_{sup}}{n_0}\right)}{n_0} - \frac{\tan^{-1}\left(\frac{n_{inf}}{n_0}\right)}{n_0}\right]$$

from which:

$$G_d(n_0) = \frac{\sigma^2}{\left[\frac{\tan^{-1}\left(\frac{n_{sup}}{n_0}\right)}{n_0} - \frac{\tan^{-1}\left(\frac{n_{inf}}{n_0}\right)}{n_0}\right]} = n_0 \frac{\sigma^2}{\left[\tan^{-1}\left(\frac{n_{sup}}{n_0}\right) - \tan^{-1}\left(\frac{n_{inf}}{n_0}\right)\right]}. \tag{2.60}$$

The values of $G_d(n_0)$ obtained from (2.60) for each class are shown in table 2.2:

Class	RMS ISO (mm)	RMS Sussman (mm)	$G_d(n_0)$
A	4.2735	4.2737	0.0013
B	8.5469	8.5474	0.0051
C	17.0938	17.0948	0.0204
D	34.1876	34.1896	0.0814
E	68.3753	68.3792	0.03256
F	136.7505	136.7583	1.3025
G	273.5010	273.5166	5.2098
H	547.0021	547.0333	20.8392

Table 2.2: Profiles classification and $G_d(n_0)$ values according to ISO 8608 and Sussman

A comparison between the classifications (2.56) and (2.59) is shown in figure 2.18, where the limits for the frequency band n_{inf} and n_{sup} are underlined; in figure 2.19 is shown the classification according to (2.59) at a vehicle speed equal to 20 m/s.

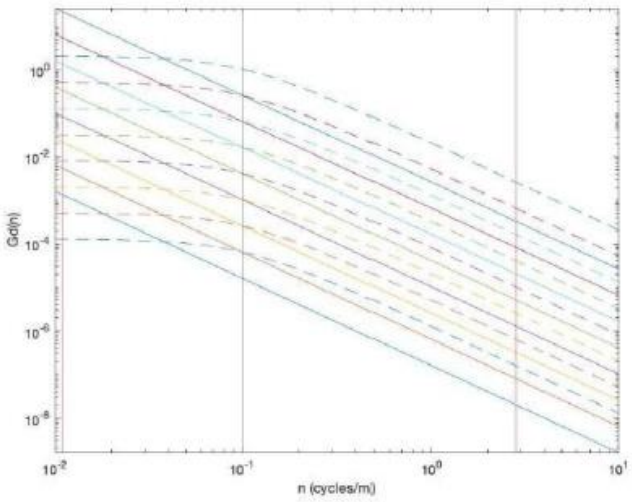

Figure 2.18: Profiles classifications comparison between ISO 8608 and Sussman

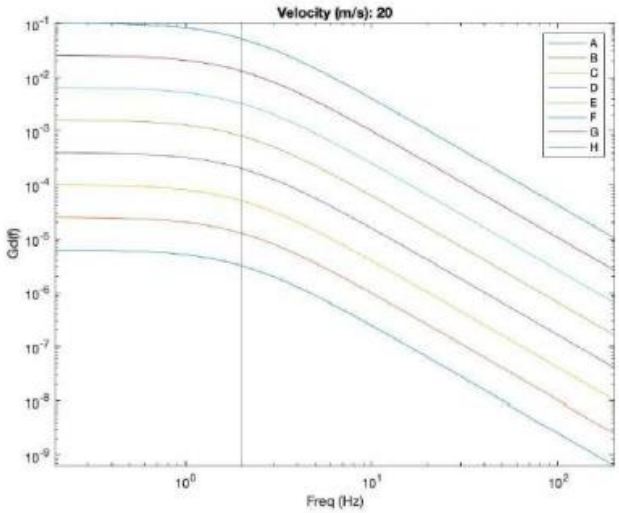

Figure 2.19: Graphic profiles classification according to Sussman for a vehicle speed of 20 m/s

2.3 *SIMULATION OF RAIL PROFILES*

To obtain the history of the roughness profile over time, it is possible to start from the discrete PSD in the temporal frequency domain. It must be considered, first of all, that land vehicles, and in particular railway vehicles, as will be seen in chapter 3, can be schematized with *half-train* or *full-train* models. In the first case, one half (right or left) of the vehicle is considered; therefore for each axle only one wheel is considered. In the second case, the vehicle is taken into consideration in its entirety. For simplicity, the diagram in figure 2.20 is considered, where L is the distance between the two axles, B the distance between two wheels belonging to the same axis, and u the forward speed; the wheels are numbered from 1 to 4. In case you want to use a half-car model the only points of contact are wheels 1 and 3. The inputs on the two wheels, due to the road (rail) roughness, are considered identical (as if they moved on a track), but with the one on wheel 3 lagging behind the one on wheel 1 for a time value equal to:

$$\tau = \frac{L}{u}. \tag{2.61}$$

If, on the other hand, you want to use a full-car model, you must still take into account the time lag between the front and rear axles, but in addition it is necessary to consider that the vehicle is subject to stresses due to road roughness on both the right and left wheels. These two road profiles have a *spatial correlation*.

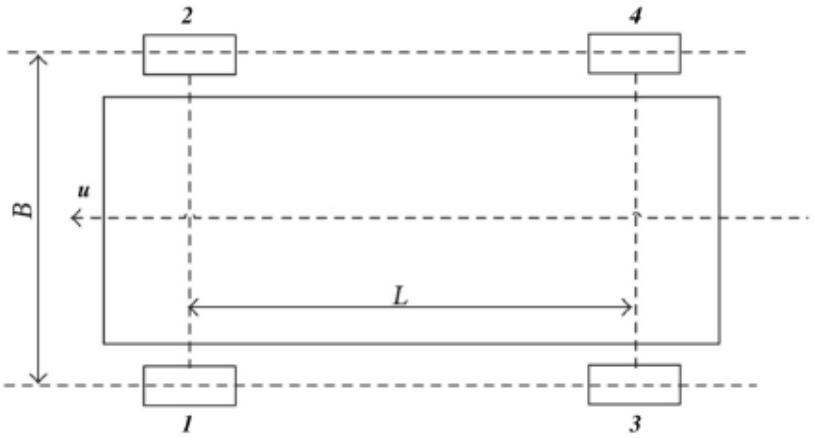

Figure 2.20: Top view of a 4-wheeled vehicle (adapted from [6])

2.3.1 SIMULATION OF A WHEEL

To obtain the frequency transform of the road/rail profile, it is possible to construct the module and phase starting from the expression of the discrete PSD. At that point, it is sufficient to apply the inverse Fourier transform to obtain the time history of the profile.
It is shown that $G_d(\omega)$ is linked to the assembly mean on n repetitions of the product of the module of the transform of the process and its conjugate in ω through the following relationship:

$$G_d(\omega) = \frac{< Y(\omega)Y^*(\omega) >}{2\pi\delta(0)}. \tag{2.62}$$

where $\delta(0)$ is a constant value that is proportional to the observation time of the process.
In paragraph 2.1 we saw how a road/rail process can be considered as a stationary, Gaussian, and ergodic process. In particular, for equations (2.5) and (2.6), we have that a single realization of the process is representative of the same. Consequently, the numerator of (2.62) can be written as:

$$< Y(\omega)Y^*(\omega) > \approx Y(\omega)Y^*(\omega) = |Y(\omega)|^2,$$

So the (2.62) becomes:

$$G_d(\omega) = \frac{|Y(\omega)|^2}{2\pi\delta(0)}. \tag{2.63}$$

So the modulus of the transform is:

$$|Y(\omega)| = \sqrt{G_d(\omega)2\pi\delta(0)}. \tag{2.64}$$

Once the modulus has been determined, to obtain the transform it is necessary to determine the phase, in which the stochasticity of the process is found. To do this, a certain probability density function is assumed for the phase, and in particular it is made to vary in the interval $[-\pi; \pi]$ with a uniform probability (Figure 2.21).

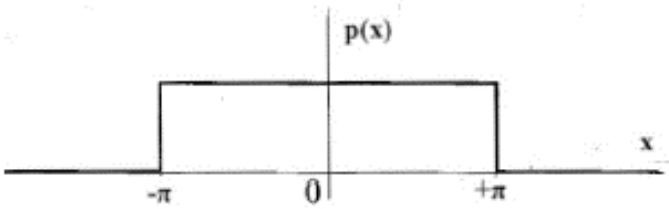

Figure 2.21: Probability density function of the phase, constant in the interval $[-\pi; \pi]$

At this point, once the transform $Y(\omega)$ has been obtained, it is possible to pass from the frequency domain to the time one through the inverse Fourier transform:

$$Y(t) = \int_{-\infty}^{+\infty} Y(\omega)e^{i\omega\tau}d\omega \tag{2.65}$$

As already mentioned in subsection 2.2.1, it should be emphasized that the experimental estimate of the spectra starting from measured and therefore sampled data does not follow the formal mathematical course described; in fact, with the development of the *fast Fourier transform* (FFT) technique, the digital estimates of the spectra can be obtained directly from the histories by means of suitable algorithms. We must therefore pay attention to the construction of the transform. Since the signal is discretely sampled, it is not possible to think about the entire frequency axis, but it is limited to a certain frequency band. By indicating the sampling frequency of the signal with f_c, this can be represented up to the frequency $f_{max} = f_c/2$; and so:

$$Y(t) = \frac{1}{f_c}\int_{-f_c/2}^{+f_c/2} Y(\omega)e^{i\omega t_i}d\omega \tag{2.66}$$

where the subscript i indicates the number of time intervals in which the signal has been divided. The sampling frequency is the inverse of the sampling interval Δt, and so we have $t_i = i\Delta t = i/f_c$. The largest period that can be described in the discrete case is obviously equal to the time of observation of the phenomenon t_0 and so the minimum appreciable frequency is $f_{min} = 1/t_0$. In this way it is possible to construct a *half spectrum* (spectrum of positive frequencies), which goes from f_{min} to f_{max}. Being in the case of a discrete signal of a real process, also the *half spectrum of the negative frequencies* is translated and considered at positive frequencies. It is shown that there is a symmetry between the two spectra, and in particular that the modules of the two half spectra are symmetrical with respect to the vertical line passing through f_{max}, while the phases are symmetrical with respect to the point $[f_{max}, \theta(f_{max})]$. This also affects the relationship that links the PSD to the modulus of the transform (equation (2.62)). In particular, due to the different definition of transform of the analytic Fourier transform compared to the discrete one (DFT), in which the sampling frequency is present in place of the factor 2π, we have that (2.64) becomes:

$$|Y(\omega)| = f_c\sqrt{G_d(\omega)t_0}. \tag{2.67}$$

Figure 2.22 shows the module and phase (a restricted interval of frequencies has been represented for the phase to highlight the symmetry) of the transform obtained as just described, starting from the PSD of the road according to Sussman Class A. A sampling frequency $f_c = 1000\ Hz$, a resolution in frequency $\Delta f = 1 \cdot 10^{-3}\ Hz$, and then an observation time of $t_0 = 1/\Delta f = 1000\ s$ were used.

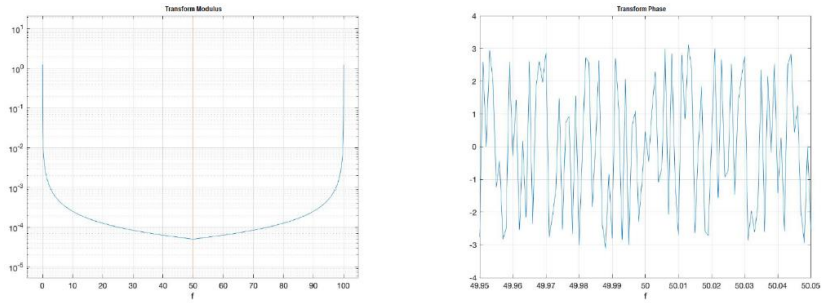

(a) Transform Modulus (b) Transform Phase

Figure 2.22: Frequency domain representation of the Transform of a realization of a Sussman Class A profile

In figure 2.23 is represented the same profile realization but in the time domain:

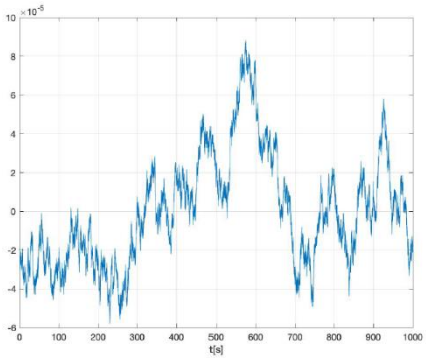

Figure 2.23: Time domain representation of a realization of a Sussman Class A profile

2.3.2 COMPLETE WHEELSET SIMULATION

Consider the case in figure 2.20. Obviously, any subsequent explanation is also extensible to the case of a railway wagon, in which the wheels are double in respect of the full-car case, i.e. 8.
A model for the simulation of the profile on all the contact points (and therefore the wheels) is based on the following assumptions:

- the wheel's contact area of the front axle and the rear axle of the vehicle are the same and the vehicle moves in a straight line with constant speed;
- the statistical properties of the left and right profiles are the same, i.e. they have the same PSD.

However, although the left and right wheels are statistically equivalent, the actual profiles are not identical. To take into account these differences, which generate noise mainly in terms of roll, a coherence function defined as:

$$\Gamma(n) = \frac{|G_{LR}(n)|}{\sqrt{G_{LL}(n) \cdot G_{RR}(n)}}, \tag{2.68}$$

where $G_{LL}(n)$ and $G_{RR}(n)$ are respectively the auto-PSD of the left and right profiles, while $G_{LR}(n)$ is the cross-PSD of the two profiles. From studies and measurements carried out on the coherence data for different types of road surfaces or railway tracks it emerged that the coherence function, included in the interval $[0; 1]$, has higher values at low frequencies and very low values at higher frequencies. In particular, if $\Gamma(n) = 0$ it means that the left and right profiles are totally uncorrelated, while when $\Gamma(n) = 1$ they are perfectly correlated. Furthermore, it has been seen that for different types of roads the coherence functions are very similar. The fitting model proposed by Bogsjö [3] is based on the use of a decreasing exponential function with the parameters μ and depending on the distance B between two wheels of the same axle, according to the following relationship:

$$\Gamma(n) = e^{-\mu B|n|}. \tag{2.69}$$

Assuming $\mu = 3.80$ and plotting the results in temporal frequency instead of spatial frequency, we obtain the curve shown in figure 2.24:

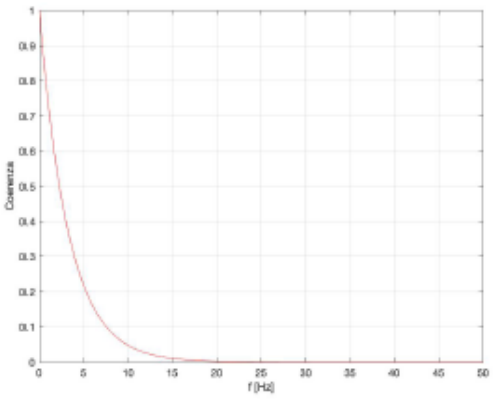

Figure 2.24: Bogsjö coherence function

With reference to figure 2.20, the cross-PSD can be written as a product of module and phase; for example between wheels 1 and 2 we have:

$$G_{12}(f) = |G_{12}(f)|e^{i\varphi_{12}(f)}, \tag{2.70}$$

where $\varphi_{12}(f)$ is the phase shift between the two wheels. Since wheels 1 and 2 are on the same axis, we have that $\varphi_{12}(f) = 0$. Therefore:

$$G_{12}(f) = |G_{12}(f)| = \Gamma(f)\sqrt{G_{11}(f) \cdot G_{22}(f)}, \tag{2.71}$$

But $G_{11}(f) = G_{22}(f) = G_d(f)$, so:

$$G_{12}(f) = G_d(f) \cdot \Gamma(f), \tag{2.72}$$

For the cross-PSD between wheels 1 and 4, a time delay given by (2.61) must be considered, that is $\tau = L/u$. In this case we have:

$$\begin{aligned} G_{14}(f) \quad &= |G_{14}(f)|e^{i\varphi_{14}(f)} = \\ &= \sqrt{G_{11}(f) \cdot G_{22}(f)} \cdot \Gamma(f) \cdot e^{i2\pi f\tau_{14}} = \\ &= G_d(f) \cdot \Gamma(f) \cdot e^{i2\pi f\tau}; \end{aligned} \tag{2.73}$$

So it is possible to wright the input matrix as:

$$G_{in}(f) = \begin{bmatrix} G_{11}(f) & G_{12}(f) & G_{13}(f) & G_{14}(f) \\ G_{21}(f) & G_{22}(f) & G_{23}(f) & G_{24}(f) \\ G_{31}(f) & G_{32}(f) & G_{33}(f) & G_{34}(f) \\ G_{41}(f) & G_{42}(f) & G_{43}(f) & G_{44}(f) \end{bmatrix}, \tag{2.74}$$

that becomes:

$$G_{in}(f) = G_d(f)\begin{bmatrix} 1 & \Gamma(f) & e^{i2\pi f\tau} & \Gamma(f)e^{i2\pi f\tau} \\ \Gamma(f) & 1 & \Gamma(f)e^{i2\pi f\tau} & e^{i2\pi f\tau} \\ e^{-i2\pi f\tau} & \Gamma(f)e^{-i2\pi f\tau} & 1 & \Gamma(f) \\ \Gamma(f)e^{-i2\pi f\tau} & e^{-i2\pi f\tau} & \Gamma(f) & 1 \end{bmatrix}. \tag{2.75}$$

About the spectra:

$$Y_2(f) = Y_1(f) \cdot \Gamma(f), \tag{2.76}$$

and

$$Y_4(f) = Y_1(f) \cdot \Gamma(f) \cdot e^{-i2\pi f\tau_{14}}. \tag{2.77}$$

Applying what we have just seen to a model similar to that of figure 2.20, we obtain:

- for the correlation of the left front wheel and the left rear wheel (figure 2.25), it can be seen that the two signals are actually equal over time but out of phase with time τ, therefore the method is accurate;
- for the correlation of the front left wheel and the front right wheel (figure 2.26), it can be seen that there is a difference in amplitude between the two signals over time.

Due to the smaller amplitude of the signal over time of the front right wheel compared to the front left, there will be a variation of the PSD of the profile between the two same wheels starting from the medium-high frequencies (figure 2.27). This difference is attributable to the fact that the coherence function, which varies between 0 and 1, assumes values close to 0 at high frequencies.

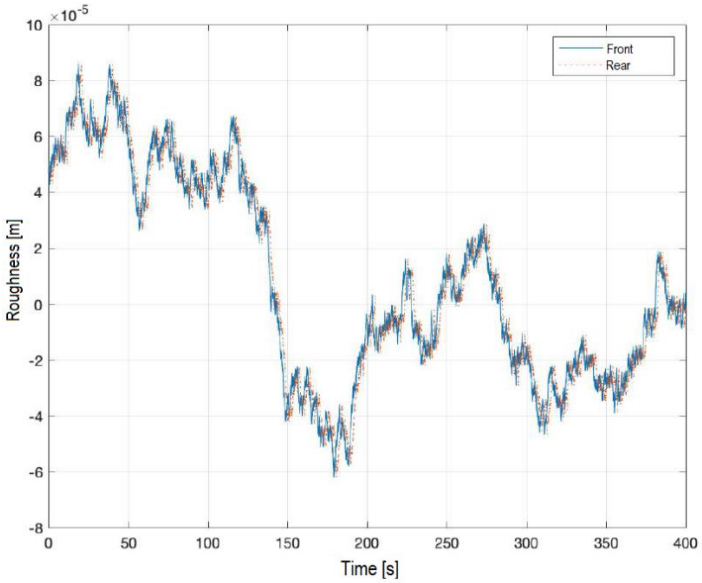

Figure 2.25: Front-Rear time domain comparison

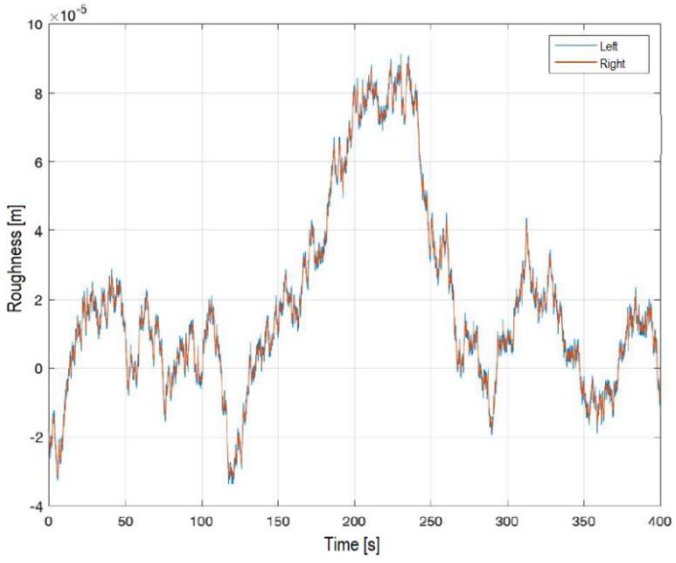

Figure 2.26: Left-Right time domain comparison

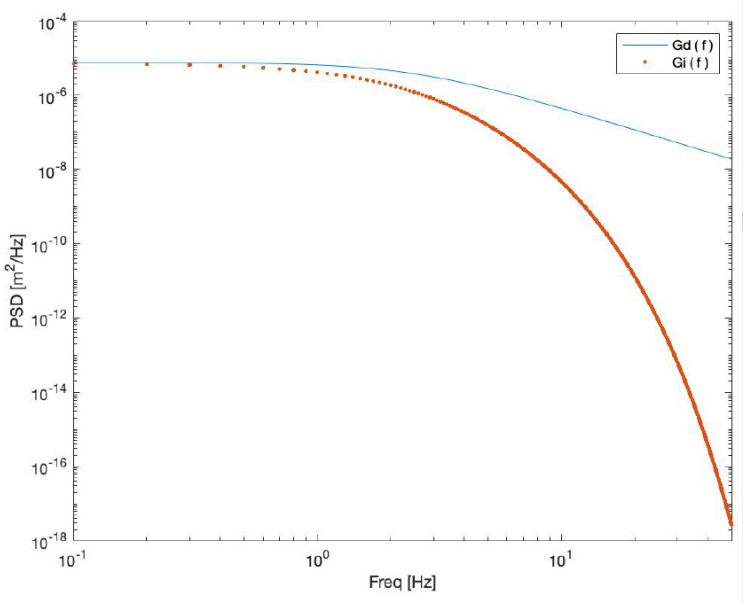

Figure 2.27: Standard-Simulated PSD comparison

In other words, the PSD of the rolling profile of one wheel is lower than the PSD of the profile of the other wheel on the same axis, which is consistent with the standard PSD characterized with one of the methods described in paragraph 2.2. To solve this problem, in the first place, it is possible to consider the roughness of the profile divided into a perturbed ($\delta Y_i(t)$, where $i = l, r$) and an unperturbed part ($Y_0(t)$). The unperturbed part is assumed to be equivalent for the right and left profiles, while the perturbed part of one profile is independent of the other. Secondly, the auto-PSDs of the roughness of the profile unperturbed and perturbed are derived through the coherence function. Finally, the roughness of the profile is obtained by combining theoretical and perturbed roughness [9].
Based on what has been said for the two profiles, the historical signals are:

$$Y_l(t) = Y_0(t) + \delta Y_l(t),$$

And

$$Y_r(t) = Y_0(t) + \delta Y_r(t).$$

The realization over time of the unperturbed component can be obtained as seen in subsection 2.3.1, being:

$$Y_0(\omega) = |Y_0(\omega)|e^{i\varphi(\omega)},$$

whose Fourier transform is:

$$Y_0(\omega) = |Y_0(\omega)|e^{i\varphi(\omega)} = Y_d(\omega)\Gamma(\omega).$$

So the PSD is given by:

$$G_0(\omega) = G_d(\omega)\Gamma(\omega).$$

For the perturbed components it is considered that $\delta Y_i(t)$ (where $i = l, r$) is the inverse Fuorier transform of the quantity:

$$\Delta Y_i(\omega) = |\Delta Y_i(\omega)| e^{i\rho_i(\omega)},$$

whose PSD can be written as:

$$\Delta G_i(\omega) = G_d(\omega) - G_0(\omega) = G_d(\omega) - G_d(\omega)\Gamma(\omega) = G_d(\omega)\big(1 - \Gamma(\omega)\big). \qquad (2.78)$$

Therefore, starting from 2.78 using the procedure seen in subsection 2.3.1 it is possible to construct the transform of the compensations $\Delta Y_l(\omega)$ and $\Delta Y_r(\omega)$ and their realization over time, shown in figure 2.28.

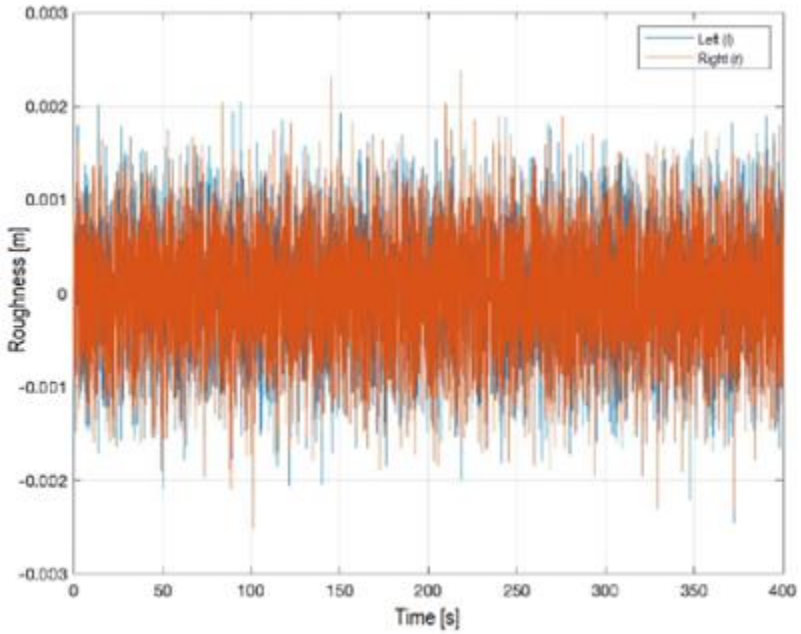

Figure 2.28: Time domain representation of $\delta Y_l(t)$ and $\delta Y_r(t)$

In the construction, however, attention must be paid to the fact that the randomly generated phases $\rho_i(\omega)$ must be uncorrelated with each other and with respect to $\varphi(\omega)$. Once the compensation is applied it is possible to obtain the PSDs of the left and right profiles. Figures 2.29 and 2.30 show the module and phase of the auto-PSD and cross-PSD of the two profiles.
Note how the auto-PSD of the roughness of the left and right profiles are in good agreement with the starting PSD. This is also true for cross-PSDs at low frequencies, while at high frequencies there is a greater deviation. As previously mentioned, the proposed method assumes that the perturbed roughness constructed are independent of each other and independent of the original profile roughness.

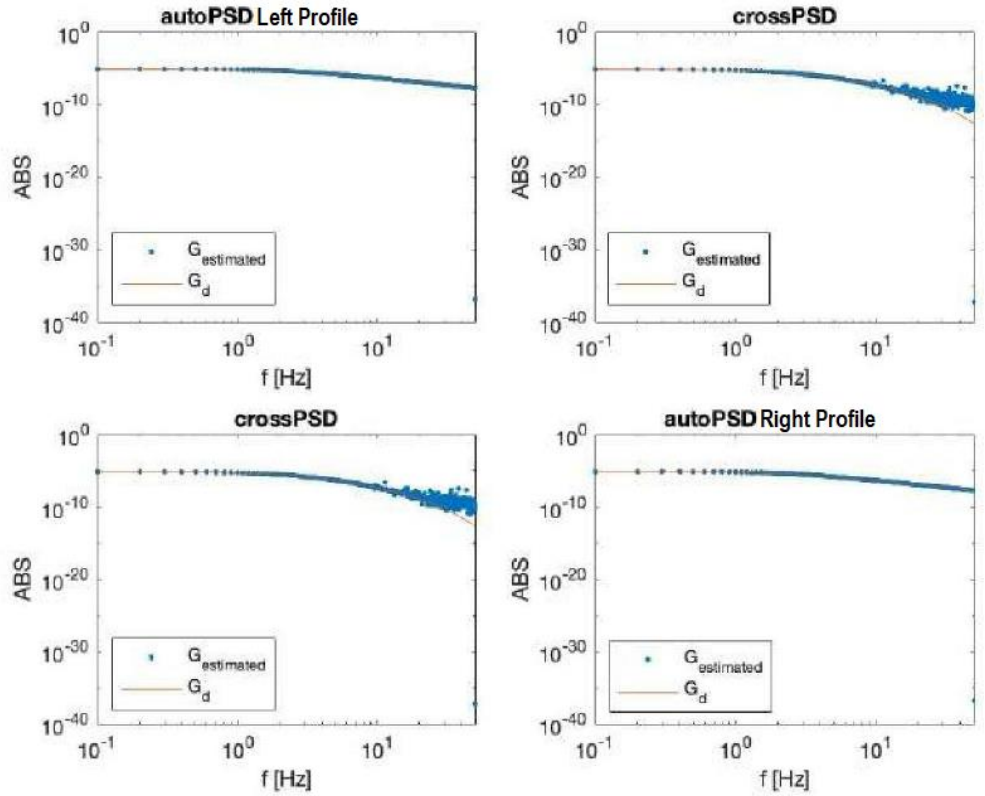

Figure 2.29: Modulus of the PSD of the profile

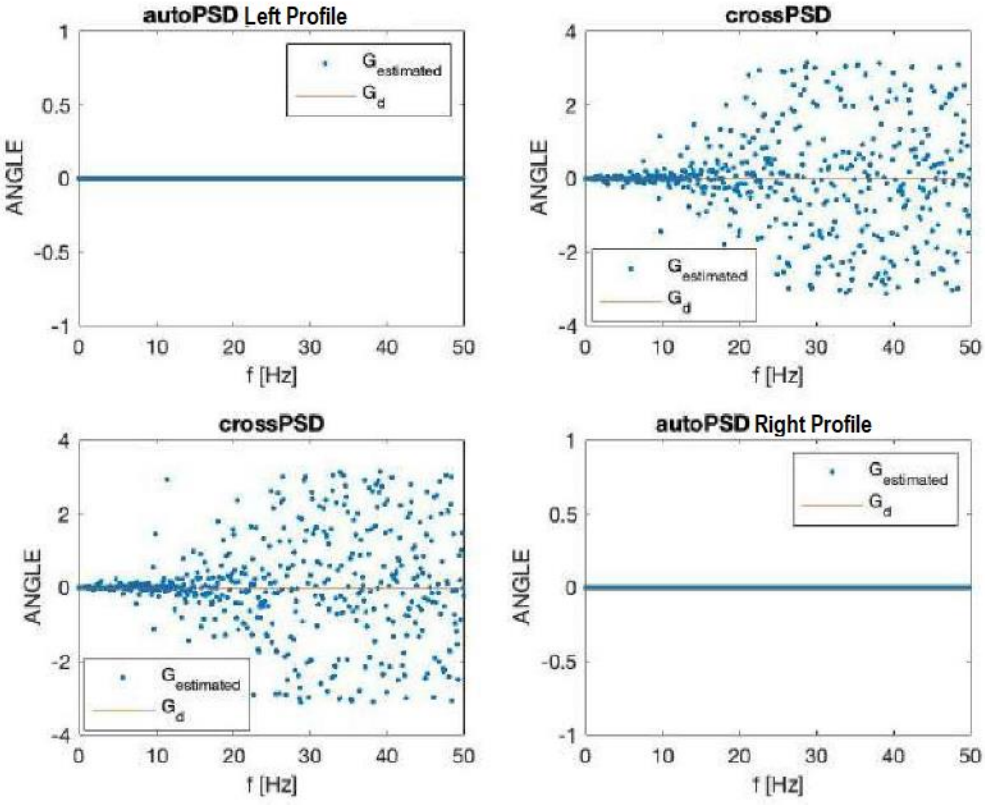

Figure 2.30: Phase of the PSD of the profile

In figure 2.31 it is possible to see how the coherence function between the left and right profiles, obtained through the definition (2.68), has the same trend as the coherence function specified in (2.69).

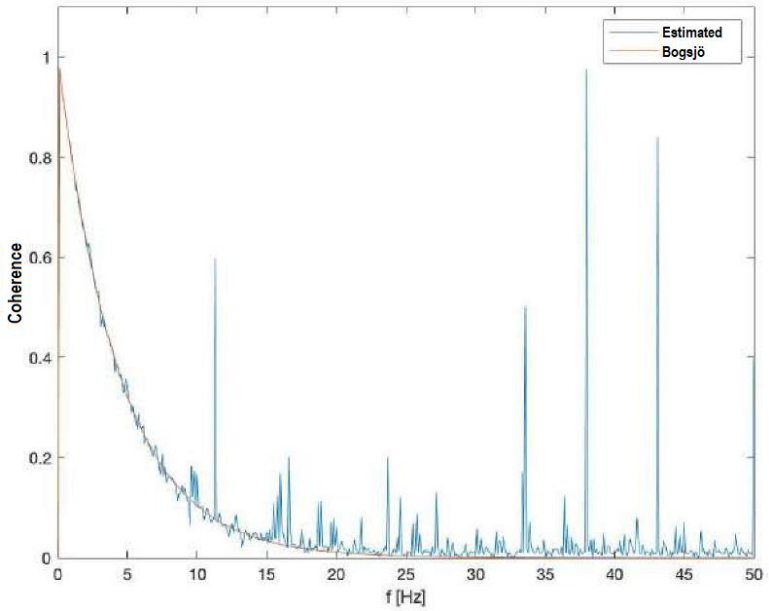

Figure 2.31: Comparison between the estimated and the Bogsjö's coherence

2.4 *IDENTIFICATION OF RAIL PROFILES*

From a mechanical point of view, the road/rail profile is a boundary condition applied to the vehicle's wheels and, at a given speed, represents a dynamic stress for the vehicle-system. The estimation of the excitation that acts on a system starting from its response is the so-called inverse problem. In this specific case, it is a matter of finding a way to estimate the profile from the vehicle's responses. There are several methods in the literature, some of which will be proposed in this section.

2.4.1 OPERATIONAL MODAL ANALYSIS FOR THE RAIL PROFILES IDENTIFICATION

A method that can be used for solving the inverse problem, falls into the category of Operational Modal Analysis (OMA) and it allows to estimate the modal parameters of road/rail vehicle systems in working conditions and to indirectly characterize the statistical properties of roughness of the rolling profiles of road or railway surfaces and therefore to classify them.
The Operational Modal Analysis, in general, allows an experimental structural identification under the real operating conditions: passing directly from the output data, leading to linearized modal models around the most interesting working points and, in the case of controlled systems, providing the information necessary for design and verification. All these characters are necessary for the experimental evaluation of vehicle suspension systems. The strength of this technique lies in the fact that in most cases only the response data can be measured and the actual loads are not

available. Therefore, system identification must be based on output data only. However, some problems arise when the operational identification of a vehicle system is performed, substantially linked to the nature of the loads induced by the roughness of the profiles on which the vehicle itself moves. The forces applied on the wheels, in fact, depending on their location, as already discussed in the previous section, are influenced by the temporal and/or spatial correlation, and, moreover, they do not adapt to the shape of the white noise sequences. Therefore, the nature of these stresses strongly violates the hypotheses on which the formulation of the classical OMA modal model is based. The salient points of a method that manages to overcome this obstacle will be shown below [4]. Consequently, it is possible to carry out an indirect characterization of the roughness of the rolling surface, which can be used to improve comfort and safety.
Modal parameters are important because they describe the intrinsic dynamic properties of a structure. Since these dynamic properties are directly related to mass and stiffness, the modal parameters obtained experimentally provide information on these two physical properties of a structure. The experimental identification of a linear system with N degrees of freedom, subjected to stresses, aims to estimate the so-called operative modal parameters:

- Poles of the system λ_n;
- Modal vectors ψ_n;
- Reference operational vectors φ_n.

The poles of the system, in particular, allow to obtain information regarding the natural frequencies ω_n and the damping ratios ζ_n of the system, in fact:

$$\lambda_n = \left(-\zeta_n + i\sqrt{1-\zeta_n^2}\right)\omega_n \quad with\ n = 1, \dots, N \tag{2.79}$$

It is possible to extract, in the frequency domain, the modal parameters directly from the output auto and cross-spectral densities of the system. At the basis of the OMA there are the NExT hypotheses (Natural Excitation Techniques), so that the loads acting on the system must have a trend attributable to a sequence of strictly unrelated white noises; the latter hypothesis translates into the fact that the PSD matrix of the inputs is devoid of the extra-diagonal elements, that is:

$$S_{in} = \begin{bmatrix} S_1 & \cdots & 0 \\ 0 & \ddots & 0 \\ 0 & \cdots & S_N \end{bmatrix}. \tag{2.80}$$

Given these assumptions, it is possible to obtain an expression of the modal model of the PSD of the system outputs. In other words, once the PSD of the outputs $S_{q_i q_j}(\omega)$ has been obtained, this can be written as a function of the modal parameters as:

$$S_{q_k q_l}(\omega) = \sum_{n=1}^{2N} \frac{\varphi_{ln}\psi_{kn}}{i\omega - \lambda_n} + \frac{\psi_{kn}\varphi_{ln}}{-i\omega - \lambda_n}. \tag{2.81}$$

So it is possible to estimate the modal parameters and compare them with the design ones.
Equation 2.81 can be rewritten in matrix form as:

$$S_q(\omega) = \sum_{n=1}^{2N} \frac{\varphi_n \psi_n^T}{i\omega - \lambda_n} + \frac{\psi_n \varphi_n^T}{-i\omega - \lambda_n}. \tag{2.82}$$

Since power spectral density and correlation function are related by the Fourier transform, it is written in an equivalent way:

$$R_q(\tau) = \sum_{n=1}^{2N} \varphi_n \psi_n^T e^{\lambda_n \tau} h(\tau) + \psi_n \varphi_n^T e^{-\lambda_n \tau} h(-\tau), \tag{2.83}$$

Where $R_q(\tau)$ is the system output correlation matrix and $h(\tau)$ is the Heaviside step function.
This method contemplates the use of a polynomial model before the fitting operation for the modal parameters extraction through the modal model. The definition (2.82) can be rewritten as a generic ratio between polynomial functions:

$$S_q(\omega) = \frac{\boldsymbol{B}(\boldsymbol{\omega})}{A(\omega)}, \tag{2.84}$$

So every matrix element of $S_q(\omega)$ is a polynomial ratio, where$B_{ij}(\omega)$ is the polynomial associated at each matrix element, while $A(\omega)$ is a common denominator among all elements.
For what concerns the study of rail/road profiles, the input PSD matrix is different with respect to the Classical OMA one that we have just seen. Here, as described in section 2.3.2, the extra-diagonal elements are in general not-null (basing on how they correlate to each other).
Knowing that a generic input matrix element could be written as:

$$S_{kl}(\omega) = \sqrt{S_{kk}(\omega) \cdot S_{ll}(\omega)} \cdot \Gamma(\omega) \cdot e^{i\omega\tau_{kl}} = S_d(\omega) \cdot \Gamma(\omega) \cdot e^{i2\omega\tau_{kl}}, \tag{2.85}$$

So the modal model in (2.82), in the case of correlated inputs, can be rewritten as:

$$S_q(\omega) = \sum_{n=1}^{2N} \frac{\varphi_n(\omega) \psi_n^T}{i\omega - \lambda_n} + \frac{\psi_n \varphi_n^T(-\omega)}{-i\omega - \lambda_n} \tag{2.86}$$

where $\varphi(\omega)$ is an operational vector dependent on the frequency ω, on the coherence function $\Gamma(\omega)$, on the time shift τ and defined as:

$$\varphi(\omega) = S_d(\omega) \left[\sum_{m=0}^{N_w} \Gamma_{\mathrm{m}}(\omega) \left(\alpha_n^m + \sum_{l=1}^{N_L} \left(\beta_n^{ml} e^{i\omega\tau_l} + \chi_n^{ml} e^{-i\omega\tau_l} \right) \right) \right] \tag{2.87}$$

where N_w is the number of coherence functions, coinciding with the number of carriageways ($\Gamma_0 = 1$), N_L is the number of time lags between the axles and α, β and χ are operational vectors which can be determined by solving a non-linear problem.

Equivalent to the case of non-correlated inputs, the polynomial model corresponding to (2.86) is:

$$S_q(\omega) = \frac{S_d(\omega)\left[\sum_{m=0}^{N_w} \Gamma_{\mathrm{m}}(\omega)\left(\boldsymbol{B_n^m}(\omega) + \sum_{l=1}^{N_L}\left(\boldsymbol{C_n^{ml}}(\omega)e^{i\omega\tau_l} + \boldsymbol{D_n^{ml}}(\omega)e^{-i\omega\tau_l}\right)\right)\right]}{A(\omega)} \qquad (2.88)$$

From the polynomial model it is possible to obtain the coefficients of the polynomials $A(\omega)$, $\boldsymbol{B_n^m}(\omega)$, $\boldsymbol{C_n^{ml}}(\omega)$ and $\boldsymbol{D_n^{ml}}(\omega)$, which can be reworked to obtain the values λ_n and ψ_n of (2.86).
The method just described can be used to solve the inverse problem and therefore to estimate and characterize the road profile knowing only the vehicle responses or, as in the specific case, the modal parameters.

For the analysis of the cases reported in chapter 4, some resulting tools will be exploited for better understanding the results. In the first step of the method described for the identification, the polynomial model ((2.84) or (2.88)) is exploited to obtain the poles and the modal vectors. To do this, polynomials of different degrees can be used. In this sense, the first tool that can be used is the stabilization diagram.
The stabilization diagram allows to monitor the frequency, damping and modal shape estimates as a function of the increasing order of the model for each pole. As the order of the model increases, as the number of poles increases, an increasing number of modal frequencies are estimated but at the same time the estimates of the physical modal parameters tend to stabilize as the template reaches the correct order. For modes that are very active in the measured data, the modal parameters will stabilize at a very low order model. For modes that have been little excited in the measured data, the modal parameters cannot stabilize until a very high model order is chosen. However, non-physical (computational) modes will not stabilize at all during this process and can be more easily distinguished from the modal parameter data set [1].
In this way it is possible to select the physical parameters and select the degree of the polynomial model for the minimum squares fitting on the model of equations 2.84 and 2.88.
To verify the validity of the results obtained in the identification, the comparison between the theoretical and estimated modal parameters is fundamental. If in the case of frequencies and damping ratios an immediate understanding can be made by calculating the relative error between theoretical and estimated parameters, in the case of modal forms the so-called *modal assurance criterion* or simply *MAC* can be used. The MAC is a scalar constant that relates the causal relationship between two modal vectors:

$$MAC[(\psi_n^1)(\psi_n^2)] = \frac{|(\psi_n^1)^H(\psi_n^2)|^2}{[(\psi_n^1)^H(\psi_n^1)][(\psi_n^2)^H(\psi_n^2)]} \qquad (2.89)$$

which takes values ranging from zero, i.e. no match, to one, which represents maximum consistency. In this way, if the modal vectors under consideration actually have a coherent relationship, the MAC should approach unity. The *COMAC* (*coordinates modal assurance criterion*), represents an extension of the MAC and allows to identify which degrees of freedom contribute negatively to a low value of MAC. The COMAC is calculated on a set of pairs of modes: analytical/analytical, experimental/experimental, or experimental/analytical. The two modal vectors in each pair represent the same modal vector, but the set of mode pairs represent all modes of interest in a given frequency range.
For two sets of modes to be compared, there will be a COMAC value calculated for each degree of freedom.

2.4.2 THE GONZALEZ METHOD

Gonzalez proposes a method [7] for estimating the roughness of road profiles using measurements carried out by means of accelerometers on a vehicle. This method is based on the fact that vibrations and rolling profile can be related to a linear system through a transfer function:

$$H_t(n) = \frac{PSD_{out}(n)}{PSD_r(n)} \tag{2.90}$$

where $PSD_{out}(n)$ and $PSD_r(n)$ are the power spectral densities related to the measurements made on the vehicle and to the profile. The method consists of a first calibration phase to obtain the transfer function $H_t(n)$ by making the vehicle move on an already measured profile. Once the transfer function has been obtained, this can be used to classify any other profile of the same type, again using equation (2.90). However, it is possible to operate a theoretical approach for calibration by applying a theoretical road profile to a vehicle model, generated as described in section 2.3. Therefore, the road profile of the chosen ISO class (in general, class i) is applied to the vehicle model, obtaining the PSDs at the output (with one of the methods described in chapter 3), that is the response of the vehicle-system. Using (2.90) we calculate the transfer function $H_t(n)$. At this point, to verify the effectiveness of the application of the method, a second road profile is generated (this time of class k, with $k \neq i$) and the PSD of the outputs of the same model of the previous vehicle are calculated. Finally, using the latter and the transfer function obtained in calibration, it is possible to extract (again through (2.90)) the PSD of the road profile and compare it with that of class k used. Figure 2.32 schematically shows what has just been described.

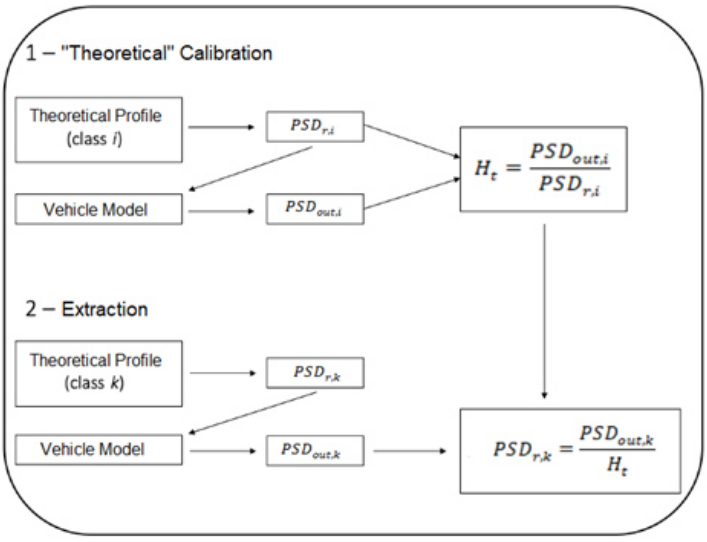

Figure 2.32: Application scheme of the Gonzalez method

In chapters 4 and 5 we will see its application to the case of railway vehicles, although it has been developed for automotive. In the case of real measurements data, as will be seen, the steps performed differ from those of figure 2.32. However, it should be noted that, with respect to the OMA, the method proposed by Gonzalez needs the knowledge of the calibration profile, which therefore must be measured in other ways. In the analyzes carried out, the theoretical models have been stressed with a theoretical profile and the responses were calculated. In the real case, the calibration profile was hypothesized, considering a theoretical profile that came as close as possible to the real case.

2.4.3 STANDARD EN 13848

The European Standard EN 13848, especially in its parts 1, 2 and 5 (respectively [18], [19] and [20]), sets the definition and classification of some track geometry parameters and explains the guide lines to perform a track geometry based maintenance strategy.
It is called *running table* the upper surface of the head of the rail, while with the terms *running surface* it is identified the curved surface defined by the longitudinal displacement of a straight line perpendicular to the centre-line of the track and tangential to both running tables.

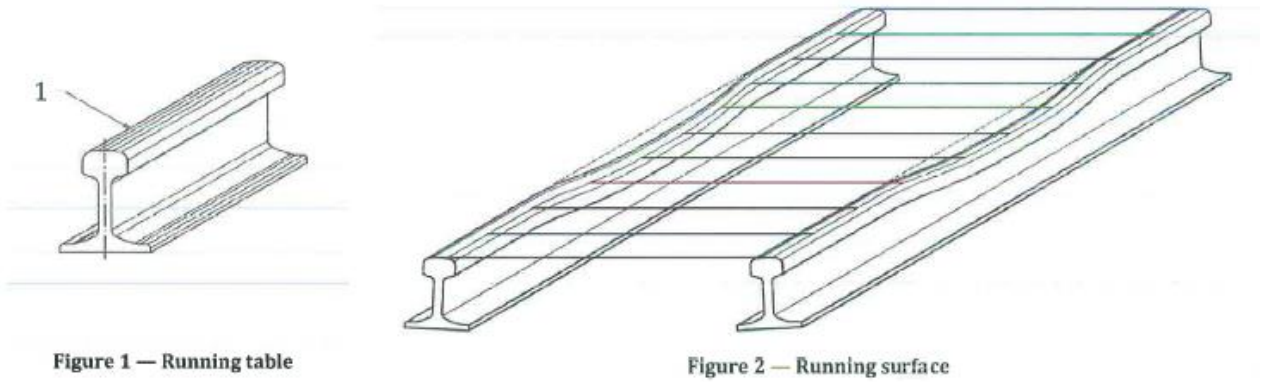

Figure 2.33: Running table and running surface (adapted from [18])

Define now two track geometry parameters on which we will focus in the next results paragraph:

- *Longitudinal Level*: the deviation z_{II} in z-direction (vertical) of running table levels on any rail from the smoothed vertical position (reference line) expressed in defined wavelength ranges;

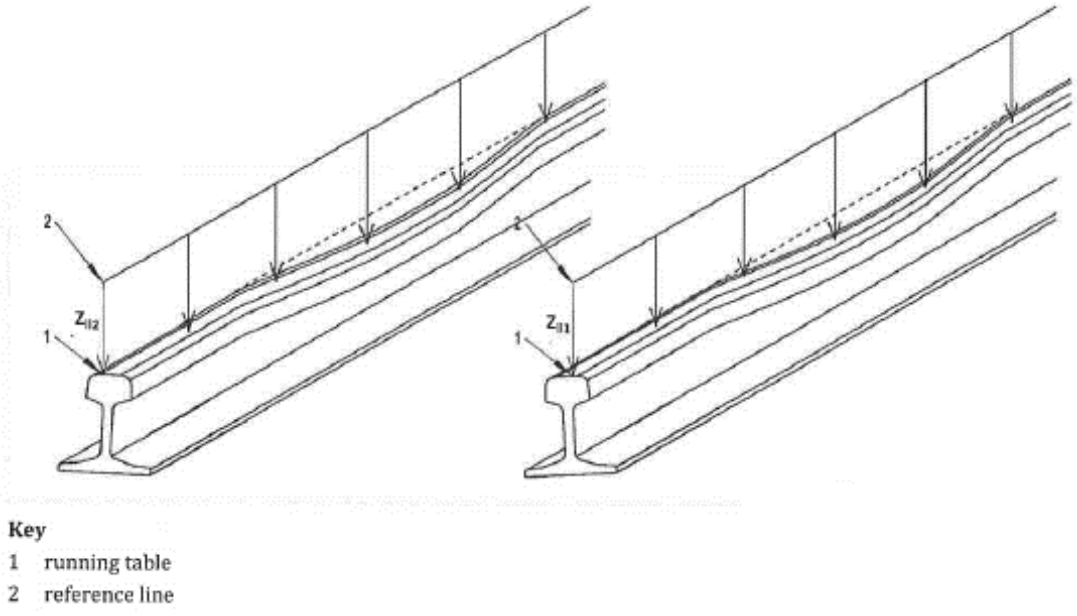

Figure 2.34: Longitudinal Level (adapted from [18])

- *Alignment*: the deviation y_p in y-direction (transverse) of the position of point P (refer to §6.1.1 of [18]) on any rail from the smoothed lateral position (reference line) expressed in defined wavelength range of interest.

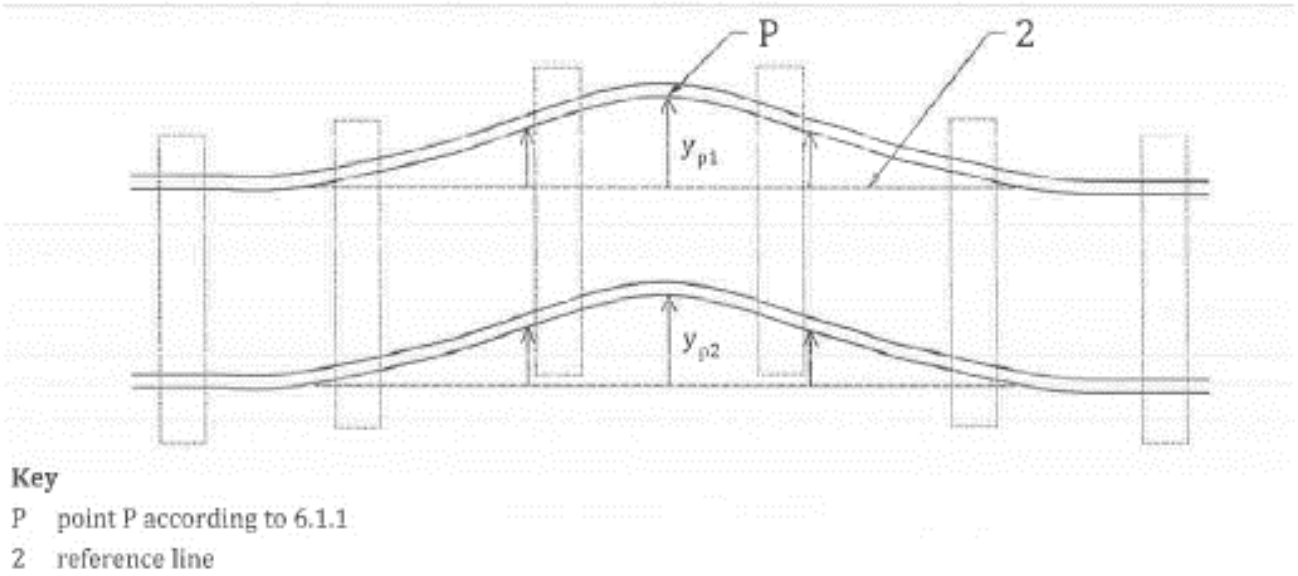

Figure 2.35: Alignment (adapted from [18])

Next table summarizes the different wavelength classification.

Range Denomination	Longitudinal Level [m]	Alignment [m]
$\boldsymbol{D0}$	$1 < \lambda \leq 5$	$1 < \lambda \leq 5$
$\boldsymbol{D1}$	$3 < \lambda \leq 25$	$3 < \lambda \leq 25$
$\boldsymbol{D2}$	$25 < \lambda \leq 70$	$25 < \lambda \leq 70$
$\boldsymbol{D3}$	$70 < \lambda \leq 150$	$70 < \lambda \leq 200$

Table 2.3: Longitudinal Level and Alignment wavelength classification

To validate the measured data, the standard [19] suggest the evaluation of repeatability and/or reproducibility among records through the following parameters:

- Transfer function, evaluated as a ratio between the measured output of two different records:

$$H = \frac{Y_2}{Y_1} \tag{2.91}$$

where Y_1 and Y_2 are the quantity measured during the runs 1 and 2;

- Coherence function, evaluated through the auto-PSD and the cross-PSD of two different measures of the same object:

$$\Gamma = \frac{|S_{xy}|^2}{S_{xx} \times S_{yy}} \tag{2.92}$$

Next table summarizes the transfer function and coherence tolerances for the different wavelength ranges:

Table C.6 — Frequency analysis — Repeatability — Longitudinal level and alignment — Tolerances

Parameter	Function	Wavelength range		
		D1	***D2***	***D3***
Longitudinal level	**Transfer function**	± 5 %	± 7%	± 10 %
	Coherence function	> 0,97	> 0,95	> 0,90
Alignment	**Transfer function**	± 7 %	± 10 %	± 15 %
	Coherence function	> 0,95	> 0,90	> 0,85

Table C.14 — Frequency analysis — Reproducibility — Longitudinal level and alignment — Tolerances

Parameter	Function	Wavelength range		
		D1	***D2***	***D3***
Longitudinal level	**Transfer function**	± 7 %	± 10 %	± 15 %
	Coherence function	> 0,95	> 0,90	> 0,85
Alignment	**Transfer function**	± 10 %	± 15 %	± 20 %
	Coherence function	> 0,90	> 0,85	> 0,80

Table 2.4: Repeatability and Reproducibility tolerance values for measuring campaign validation (adapted from [19])

3 RAILWAY VEHICLES MODELING

In this chapter some models for the study of railway vehicles will be shown and analyzed. Then we will proceed to the analysis of how the stress inputs from the road are correlated and how to obtain the responses of the dynamic system.
The main elements of a railway vehicle are the following:

- **body** (chassis): represents the body of the vehicle;
- **secondary suspension**: interposed between the bogies and the body frame;
- **bogies**: they can be equipped with traction motors and are usually two-axled;
- **primary suspension**: it is the proper suspension of the bogie, the reciprocal movement between the axles and the bogie frame is constrained through vertical prismatic guides;
- **wheels**: they represent the point of contact with the tracks.

The models that will be analyzed are:

- **6 dof** (degrees of freedom) **half-train model**: simplified model in which there are no wheels and contact with the rails occurs directly through the primary suspension. To the body and the two bogies, each of which is characterized by a mass and a moment of inertia, 2 dof each (vertical displacement, or shaking, and pitch) have been associated while for the 4 contact points only the vertical displacement. Each suspension element consists of a spring and damper in parallel;
- **10 dof half-train model**: a more complete model than the previous one with respect to which the wheels are also present (with their own mass) and the contact points are schematized with a spring;
- **17 dof full-train model**: it is the most complete model analyzed. To the body and the two bogies, 3 dof each one (vertical displacement, pitch and roll) have been associated. The wheels are 8 and are modeled as in the previous case.

3.1 *VEHICLE MODELS*

3.1.1 6 DOF HALF-TRAIN MODEL

In figure 3.1 the half-train model at 6 dof is represented while table 3.1 lists its parameters' values.

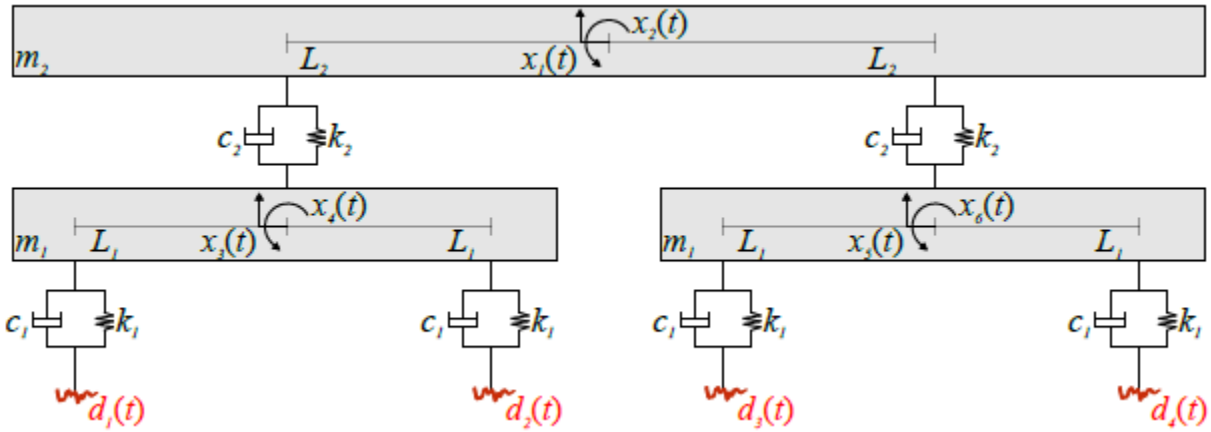

Figure 3.1: 6 dof Half-train model

Parameter	Symbol	Value
Chassis' mass	m_2	$32804\ [kg]$
Chassis' inertia (pitch)	J_{x2}	$0.67 \cdot 10^6\ [kgm^2]$
Bogie's mass	m_1	$2363.5\ [kg]$
Bogie's inertia (pitch)	J_{x1}	$1026.36\ [kgm^2]$
Primary suspension's stiffness	k_1	$5.56 \cdot 10^6\ [N/m]$
Primary suspension's damping	c_1	$1.80 \cdot 10^4\ [Ns/m]$
Secondary suspension's stiffness	k_2	$2.20 \cdot 10^6\ [N/m]$
Secondary suspension's damping	c_2	$4.00 \cdot 10^4\ [Ns/m]$
Half bogie's wheelbase	L_1	$1.25\ [m]$
Chassis' half length	L_2	$7.00\ [m]$

Table 3.1: 6 dof model numerical Parameters

The matrices of the masses (M), stiffness (K), and damping (C) are respectively:

$$M = \begin{bmatrix} m_2 & 0 & 0 & 0 & 0 & 0 \\ 0 & J_{x2} & 0 & 0 & 0 & 0 \\ 0 & 0 & m_1 & 0 & 0 & 0 \\ 0 & 0 & 0 & J_{x1} & 0 & 0 \\ 0 & 0 & 0 & 0 & m_1 & 0 \\ 0 & 0 & 0 & 0 & 0 & J_{x1} \end{bmatrix}$$

$$K = \begin{bmatrix} 2k_2 & 0 & -k_2 & 0 & -k_2 & 0 \\ 0 & 2k_2l_2^2 & k_2l_2 & 0 & -k_2l_2 & 0 \\ -k_2 & k_2l_2 & 2k_1 + k_2 & 0 & 0 & 0 \\ 0 & 0 & 0 & 2k_1l_1^2 & 0 & 0 \\ -k_2 & -k_2l_2 & 0 & 0 & 2k_1 + k_2 & 0 \\ 0 & 0 & 0 & 0 & 0 & 2k_1l_1^2 \end{bmatrix}$$

$$C = \begin{bmatrix} 2c_2 & 0 & -c_2 & 0 & -c_2 & 0 \\ 0 & 2c_2l_2^2 & c_2l_2 & 0 & -c_2l_2 & 0 \\ -c_2 & c_2l_2 & 2c_1 + c_2 & 0 & 0 & 0 \\ 0 & 0 & 0 & 2c_1l_1^2 & 0 & 0 \\ -c_2 & -c_2l_2 & 0 & 0 & 2c_1 + c_2 & 0 \\ 0 & 0 & 0 & 0 & 0 & 2c_1l_1^2 \end{bmatrix}$$

Table 3.2 shows the degrees of freedom of the system with the respective index.

Index	Degree of Freedom
1	Chassis' shaking
2	Chassis' pitch
3	Bogie's shaking
4	Bogie's pitch
5	Bogie's shaking
6	Bogie's pitch

Table 3.2: DOF of the model

The modal parameters of the system can be obtained from the eigenvectors of the system. Figure 3.2 shows the map of the poles of the system (there are poles with double multiplicity).

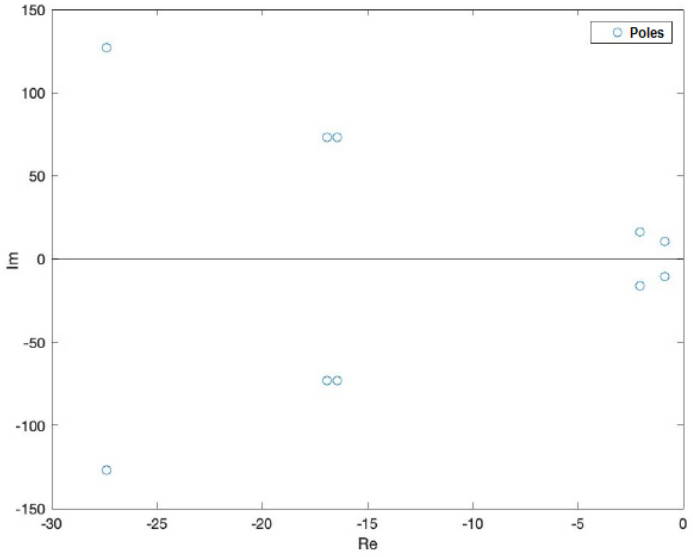

Figure 3.2: Map of the 6 dof model poles

Table 3.3 shows the natural frequencies and the damping ratios associated with the relative modes, modulus and phase are shown in figure 3.3. Modes 1 and 2 refer to shaking and pitching of the body, while Modes 3 and 4 (or 5 and 6) refer to shaking and pitching of the front (or rear) bogie.

Mode	Natural Frequency $f_n\ [Hz]$	Damping Ratio ζ_n
1	1.6839	8.2485
2	2.6081	12.6280
3	11.9501	21.8747
4	11.9503	22.5526
5	20.7077	21.0611
6	20.7077	21.0611

Table 3.3: 6 dof model Modal Parameters

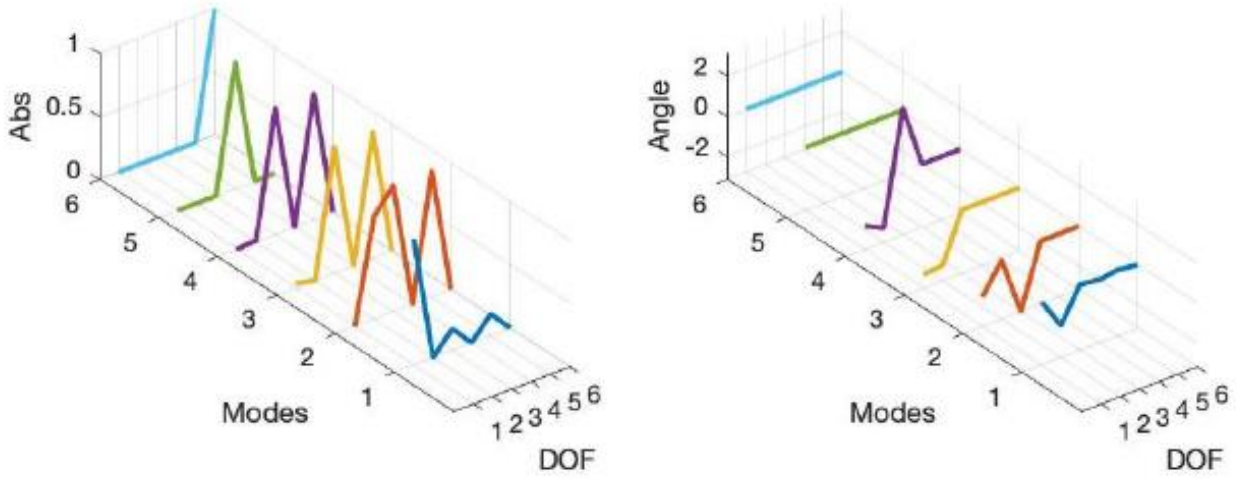

Figure 3.3: Modulus and Phase of the 6 dof model's modal vectors

3.1.2 10 DOF HALF-TRAIN MODEL

Figure 3.4 shows the 10 dof half-train model, while table 3.4 shows the respective numerical data. As anticipated, it can be seen that compared to the previous case there are the masses m_h of the wheels, with stiffness k_h and with zero damping coefficient.

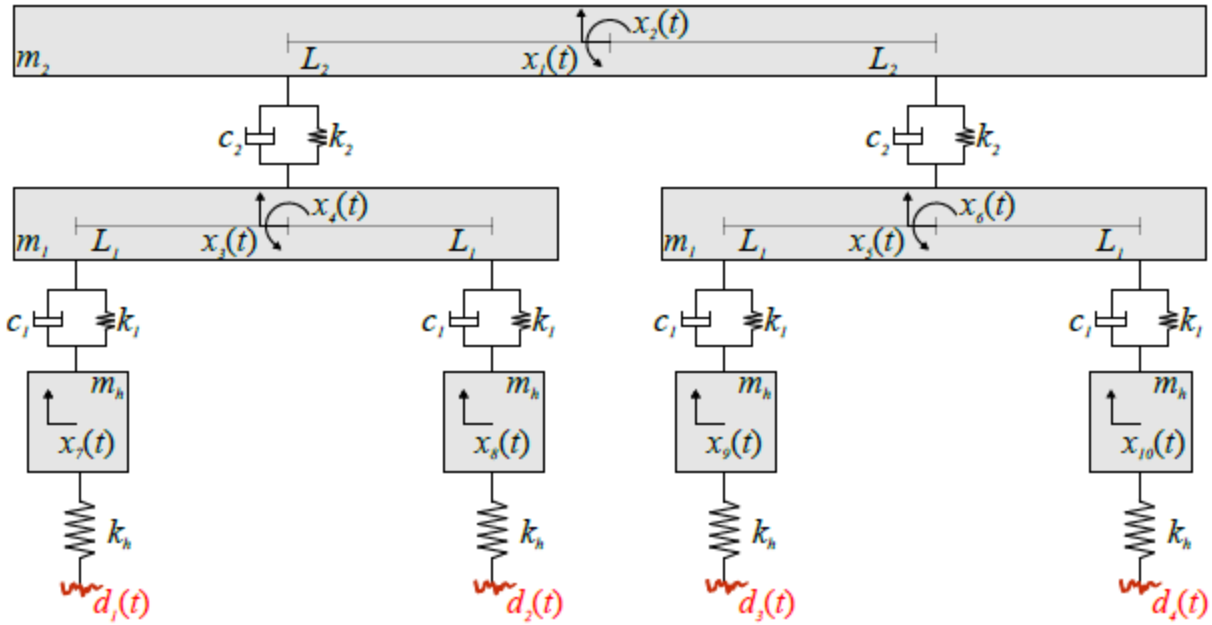

Figure 3.4: 10 dof Half-train model

Parameter	Symbol	Value
Chassis' mass	m_2	$32804\ [kg]$
Chassis' inertia (pitch)	J_{x2}	$0.67 \cdot 10^6\ [kgm^2]$
Bogie's mass	m_1	$2363.5\ [kg]$
Bogie's inertia (pitch)	J_{x1}	$1026.36\ [kgm^2]$
Wheel's mass	m_h	$1000\ [kg]$
Primary suspension's stiffness	k_1	$5.56 \cdot 10^6\ [N/m]$
Primary suspension's damping	c_1	$1.80 \cdot 10^4\ [Ns/m]$
Secondary suspension's stiffness	k_2	$2.20 \cdot 10^6\ [N/m]$
Secondary suspension's damping	c_2	$4.00 \cdot 10^4\ [Ns/m]$
Wheel's stiffness	k_h	$2.7284 \cdot 10^9\ [N/m]$
Wheel's damping	c_h	$0\ [Ns/m]$
Half bogie's wheelbase	L_1	$1.25\ [m]$
Chassis' half length	L_2	$7.00\ [m]$

Table 3.4: 10 dof model numerical Parameters

The matrices of the masses (M), stiffness (K), and damping (C) are respectively:

$$M = \begin{bmatrix} m_2 & 0 & 0 & 0 & 0 & 0 & 0 & 0 & 0 & 0 \\ 0 & J_{x2} & 0 & 0 & 0 & 0 & 0 & 0 & 0 & 0 \\ 0 & 0 & m_1 & 0 & 0 & 0 & 0 & 0 & 0 & 0 \\ 0 & 0 & 0 & J_{x1} & 0 & 0 & 0 & 0 & 0 & 0 \\ 0 & 0 & 0 & 0 & m_1 & 0 & 0 & 0 & 0 & 0 \\ 0 & 0 & 0 & 0 & 0 & J_{x1} & 0 & 0 & 0 & 0 \\ 0 & 0 & 0 & 0 & 0 & 0 & m_h & 0 & 0 & 0 \\ 0 & 0 & 0 & 0 & 0 & 0 & 0 & m_h & 0 & 0 \\ 0 & 0 & 0 & 0 & 0 & 0 & 0 & 0 & m_h & 0 \\ 0 & 0 & 0 & 0 & 0 & 0 & 0 & 0 & 0 & m_h \end{bmatrix}$$

$$K = \begin{bmatrix} 2k_2 & 0 & -k_2 & 0 & -k_2 & 0 & 0 & 0 & 0 & 0 \\ 0 & 2k_2l_2^2 & k_2l_2 & 0 & -k_2l_2 & 0 & 0 & 0 & 0 & 0 \\ -k_2 & k_2l_2 & 2k_1+k_2 & 0 & 0 & 0 & -k_1 & -k_1 & 0 & 0 \\ 0 & 0 & 0 & 2k_1l_1^2 & 0 & 0 & k_1l_1 & -k_1l_1 & 0 & 0 \\ -k_2 & -k_2l_2 & 0 & 0 & 2k_1+k_2 & 0 & 0 & 0 & -k_1 & -k_1 \\ 0 & 0 & 0 & 0 & 0 & 2k_1l_1^2 & 0 & 0 & k_1l_1 & -k_1l_1 \\ 0 & 0 & -k_1 & k_1l_1 & 0 & 0 & k_1+k_h & 0 & 0 & 0 \\ 0 & 0 & -k_1 & -k_1l_1 & 0 & 0 & 0 & k_1+k_h & 0 & 0 \\ 0 & 0 & 0 & 0 & -k_1 & k_1l_1 & 0 & 0 & k_1+k_h & 0 \\ 0 & 0 & 0 & 0 & -k_1 & -k_1l_1 & 0 & 0 & 0 & k_1+k_h \end{bmatrix}$$

$$C = \begin{bmatrix} 2c_2 & 0 & -c_2 & 0 & -c_2 & 0 & 0 & 0 & 0 & 0 \\ 0 & 2c_2l_2^2 & c_2l_2 & 0 & -c_2l_2 & 0 & 0 & 0 & 0 & 0 \\ -c_2 & c_2l_2 & 2c_1+c_2 & 0 & 0 & 0 & -c_1 & -c_1 & 0 & 0 \\ 0 & 0 & 0 & 2c_1l_1^2 & 0 & 0 & c_1l_1 & -c_1l_1 & 0 & 0 \\ -c_2 & -c_2l_2 & 0 & 0 & 2c_1+c_2 & 0 & 0 & 0 & -c_1 & -c_1 \\ 0 & 0 & 0 & 0 & 0 & 2c_1l_1^2 & 0 & 0 & c_1l_1 & -c_1l_1 \\ 0 & 0 & -c_1 & c_1l_1 & 0 & 0 & c_1 & 0 & 0 & 0 \\ 0 & 0 & -c_1 & -c_1l_1 & 0 & 0 & 0 & c_1 & 0 & 0 \\ 0 & 0 & 0 & 0 & -c_1 & c_1l_1 & 0 & 0 & c_1 & 0 \\ 0 & 0 & 0 & 0 & -c_1 & -c_1l_1 & 0 & 0 & 0 & c_1 \end{bmatrix}$$

Table 3.5 shows the degrees of freedom of the system with the respective index.

Index	Degree of Freedom	Index	Degree of Freedom
1	Chassis' shaking	**6**	Bogie's pitch
2	Chassis' pitch	**7**	Wheel's shaking
3	Bogie's shaking	**8**	Wheel's shaking
4	Bogie's pitch	**9**	Wheel's shaking
5	Bogie's shaking	**10**	Wheel's shaking

Table 3.5: DOF of the model

The modal parameters of the system can be obtained from the eigenvectors of the system. Figure 3.5 shows the map of the poles of the system (there are poles with double multiplicity). Table 3.6 shows the natural frequencies and the damping ratios associated with the relative modes; modulus and phase of the modal vectors are shown in figure 3.6 for chassis and bogies and in figure 3.7 for wheels.

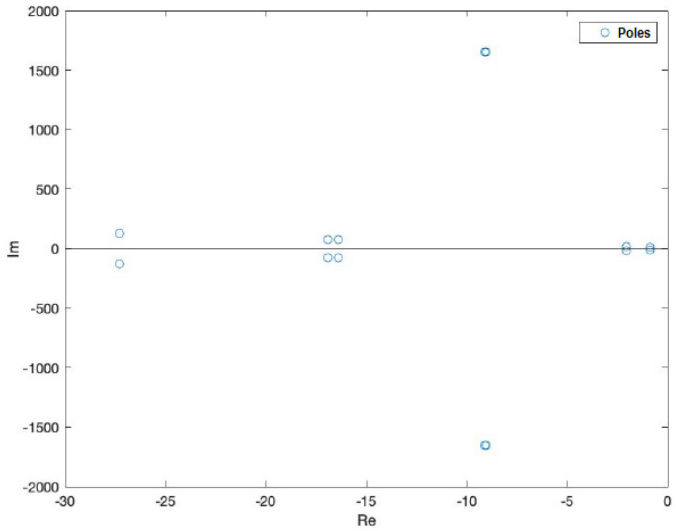

Figure 3.5: Map of the 10 dof model poles

Mode	Natural Frequency $f_n\ [Hz]$	Damping Ratio ζ_n	Mode	Natural Frequency $f_n\ [Hz]$	Damping Ratio ζ_n
1	1.6839	8.2441	**6**	20.6903	21.0001
2	2.6081	12.6207	**7**	263.1113	0.5506
3	11.9406	21.8537	**8**	263.1113	0.5506
4	11.9408	22.5334	**9**	263.1450	0.5461
5	20.6903	21.0001	**10**	263.1450	0.5461

Table 3.6: 10 dof model Modal Parameters

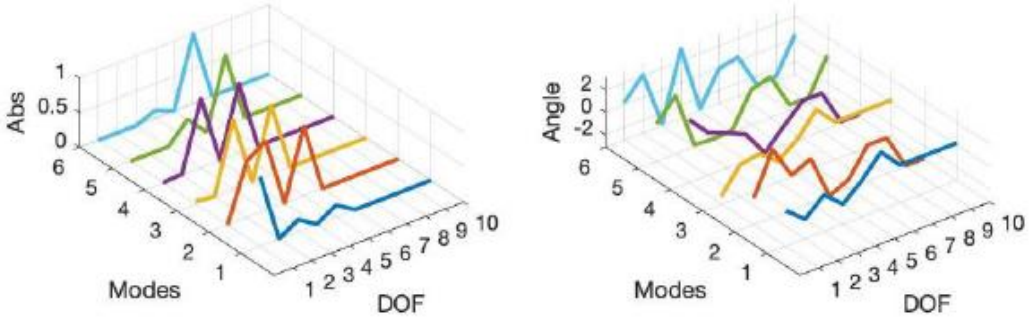

Figure 3.6: Modulus and Phase of the 10 dof model's modal vectors for Body and Bogies

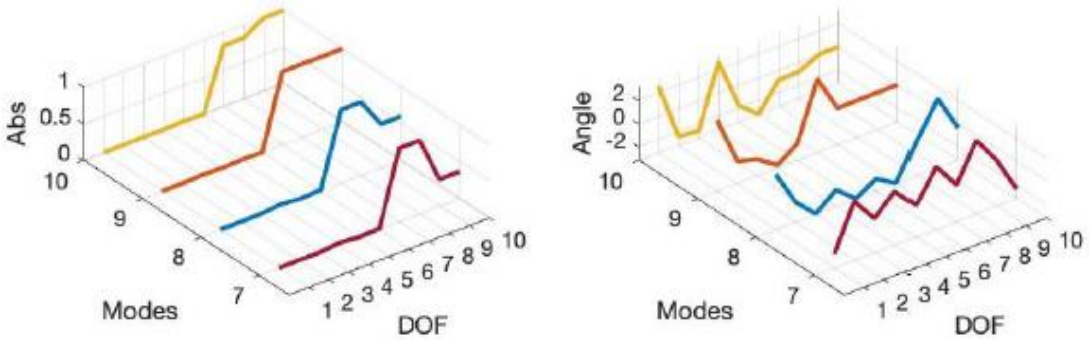

Figure 3.7: Modulus and Phase of the 10 dof model's modal vectors for Wheels

3.1.3 17 DOF FULL-TRAIN MODEL

Figure 3.8 shows the 17 dof full-train model, while table 3.7 shows the respective numerical data.

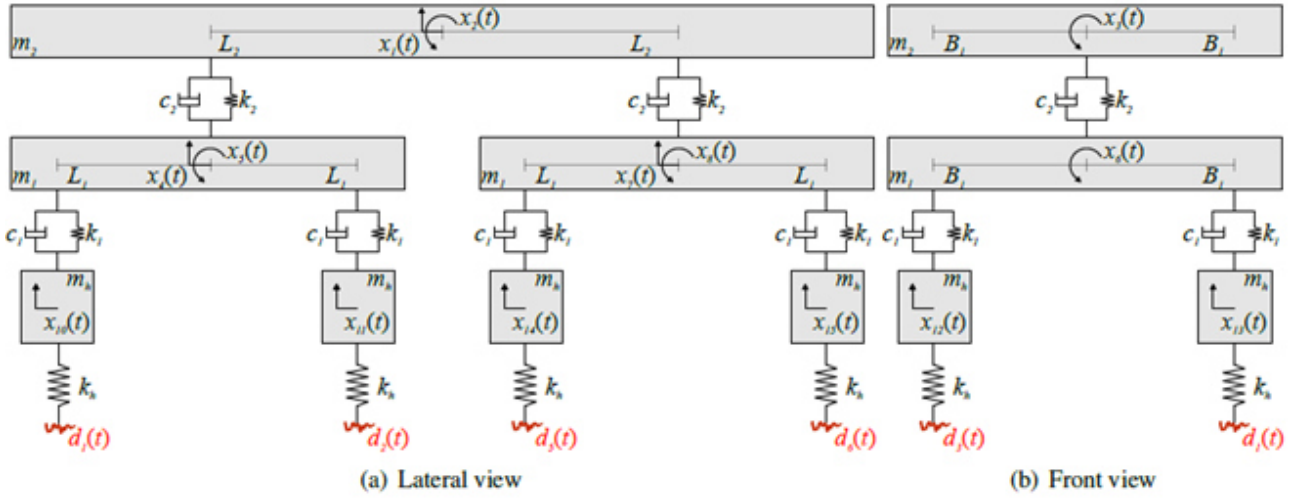

Figure 3.8: 17 dof full-train model

Parameter	Symbol	Value
Chassis' mass	m_2	$40000\ [kg]$
Chassis' inertia (pitch)	J_{x2}	$2.56 \cdot 10^6\ [kgm^2]$
Chassis' inertia (roll)	J_{y2}	$9 \cdot 10^4\ [kgm^2]$
Bogie's mass	m_1	$2100\ [kg]$
Bogie's inertia (pitch)	J_{x1}	$2100\ [kgm^2]$
Bogie's inertia (roll)	J_{y1}	$1710\ [kgm^2]$
Wheel's mass	m_h	$1950\ [kg]$
Primary suspension's stiffness	k_1	$6 \cdot 10^5\ [N/m]$
Primary suspension's damping	c_1	$1 \cdot 10^4\ [Ns/m]$
Secondary suspension's stiffness	k_2	$2.60 \cdot 10^5\ [N/m]$
Secondary suspension's damping	c_2	$2.00 \cdot 10^4\ [Ns/m]$
Wheel's stiffness	k_h	$2.44535 \cdot 10^9\ [N/m]$
Wheel's damping	c_h	$0\ [Ns/m]$
Half bogie's wheelbase	L_1	$1.28\ [m]$
Chassis' half length	L_2	$9.00\ [m]$
Gauge half length	B_1	$0.7465\ [m]$
Chassis' half thickness	B_2	$1.00\ [m]$

Table 3.7: 17 dof model numerical Parameters

Appendix A shows the matrices of damping C (A.1) and stiffness K (A.2).
The matrix of the masses (M) is:

$$M = \begin{bmatrix} m_2 & 0 & 0 & 0 & 0 & 0 & 0 & 0 & 0 & 0 & 0 & 0 & 0 & 0 & 0 & 0 & 0 \\ 0 & J_{x2} & 0 & 0 & 0 & 0 & 0 & 0 & 0 & 0 & 0 & 0 & 0 & 0 & 0 & 0 & 0 \\ 0 & 0 & J_{y2} & 0 & 0 & 0 & 0 & 0 & 0 & 0 & 0 & 0 & 0 & 0 & 0 & 0 & 0 \\ 0 & 0 & 0 & m_1 & 0 & 0 & 0 & 0 & 0 & 0 & 0 & 0 & 0 & 0 & 0 & 0 & 0 \\ 0 & 0 & 0 & 0 & J_{x1} & 0 & 0 & 0 & 0 & 0 & 0 & 0 & 0 & 0 & 0 & 0 & 0 \\ 0 & 0 & 0 & 0 & 0 & J_{y1} & 0 & 0 & 0 & 0 & 0 & 0 & 0 & 0 & 0 & 0 & 0 \\ 0 & 0 & 0 & 0 & 0 & 0 & m_1 & 0 & 0 & 0 & 0 & 0 & 0 & 0 & 0 & 0 & 0 \\ 0 & 0 & 0 & 0 & 0 & 0 & 0 & J_{x1} & 0 & 0 & 0 & 0 & 0 & 0 & 0 & 0 & 0 \\ 0 & 0 & 0 & 0 & 0 & 0 & 0 & 0 & J_{y1} & 0 & 0 & 0 & 0 & 0 & 0 & 0 & 0 \\ 0 & 0 & 0 & 0 & 0 & 0 & 0 & 0 & 0 & m_h & 0 & 0 & 0 & 0 & 0 & 0 & 0 \\ 0 & 0 & 0 & 0 & 0 & 0 & 0 & 0 & 0 & 0 & m_h & 0 & 0 & 0 & 0 & 0 & 0 \\ 0 & 0 & 0 & 0 & 0 & 0 & 0 & 0 & 0 & 0 & 0 & m_h & 0 & 0 & 0 & 0 & 0 \\ 0 & 0 & 0 & 0 & 0 & 0 & 0 & 0 & 0 & 0 & 0 & 0 & m_h & 0 & 0 & 0 & 0 \\ 0 & 0 & 0 & 0 & 0 & 0 & 0 & 0 & 0 & 0 & 0 & 0 & 0 & m_h & 0 & 0 & 0 \\ 0 & 0 & 0 & 0 & 0 & 0 & 0 & 0 & 0 & 0 & 0 & 0 & 0 & 0 & m_h & 0 & 0 \\ 0 & 0 & 0 & 0 & 0 & 0 & 0 & 0 & 0 & 0 & 0 & 0 & 0 & 0 & 0 & m_h & 0 \\ 0 & 0 & 0 & 0 & 0 & 0 & 0 & 0 & 0 & 0 & 0 & 0 & 0 & 0 & 0 & 0 & m_h \end{bmatrix}$$

Table 3.8 shows the degrees of freedom of the system with the respective index.

Index	Degree of Freedom	Index	Degree of Freedom
1	Chassis' shaking	**10**	1-L Wheel's shaking
2	Chassis' pitch	**11**	2-L Wheel's shaking
3	Chassis' roll	**12**	1-R Wheel's shaking
4	Bogie's shaking	**13**	2-R Wheel's shaking
5	Bogie's pitch	**14**	3-L Wheel's shaking
6	Bogie's roll	**15**	4-L Wheel's shaking
7	Bogie's shaking	**16**	3-R Wheel's shaking
8	Bogie's pitch	**17**	4-R Wheel's shaking
9	Bogie's roll	-	-

Table 3.8: DOF of the model

Figure 3.9 shows the map of the poles of the system (there are poles with double multiplicity). Table 3.9 shows the natural frequencies and the damping ratios associated with the relative modes; modulus and phase of the modal vectors are shown in figure 3.10, 3.11, 3.12 and 3.13.

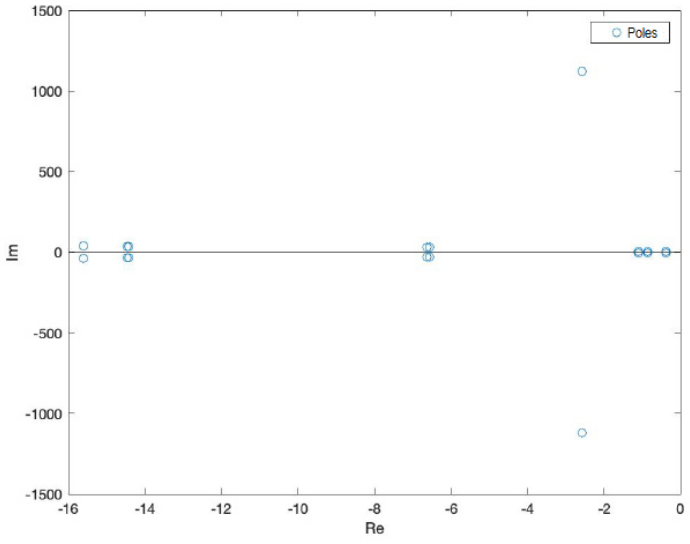

Figure 3.9: Map of the 17 dof model's poles

Mode	Natural Frequency $f_n\ [Hz]$	Damping Ratio ζ_n
1	0.4586	12.8315
2	0.7351	18.7565
3	0.8268	21.0855
4	5.2589	19.8207
5	5.2642	20.0267
6	5.9393	38.6299
7	5.9404	38.7205
8	6.8865	36.0489
9	6.8865	36.0489
10	178.2374	0.2295
11	178.2374	0.2295
12	178.2419	0.2293
13	178.2419	0.2293
14	178.2440	0.2292
15	178.2440	0.2292
16	178.2488	0.2289
17	178.2488	0.2289

Table 3.9: 17 dof model Modal Parameters

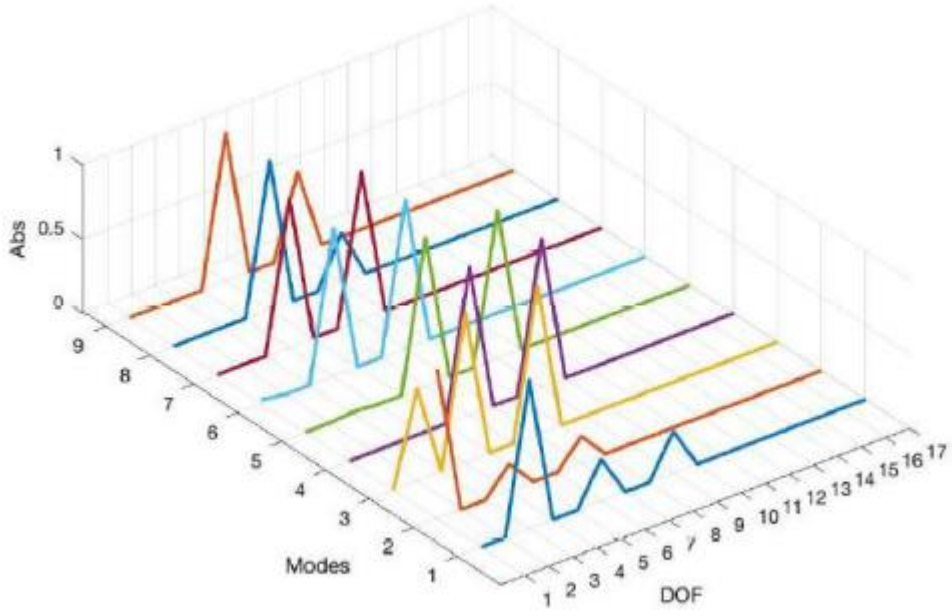

Figure 3.10: Modulus of the 17 dof model's modal vectors for Body and Bogies

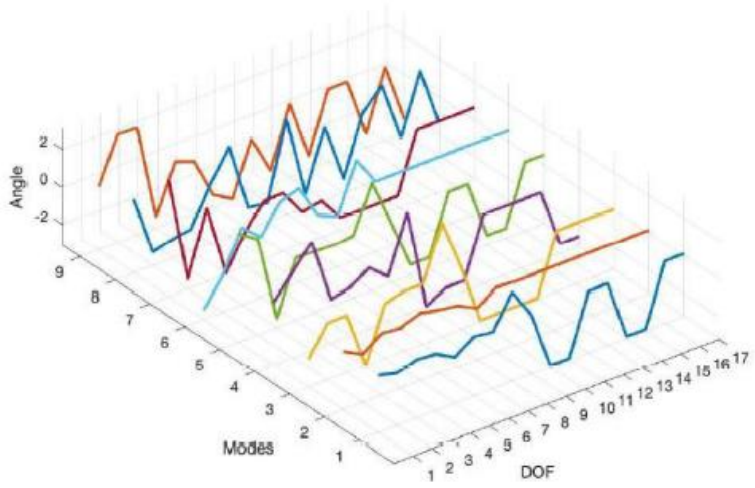

Figure 3.11: Phase of the 17 dof model's modal vectors for Body and Bogies

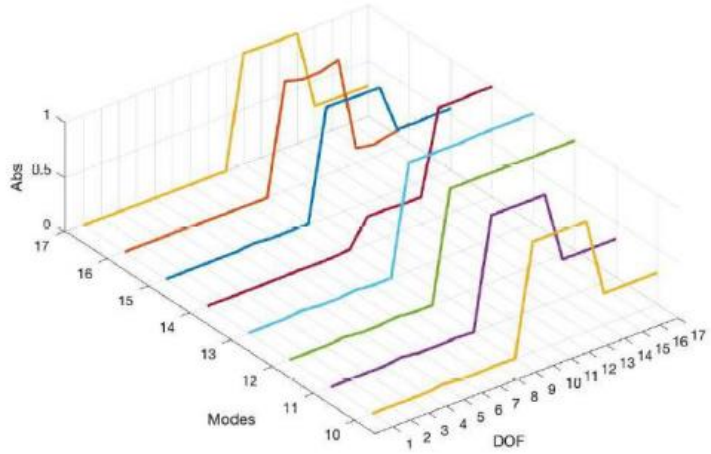

Figure 3.12: Modulus of the 17 dof model's modal vectors for Wheels

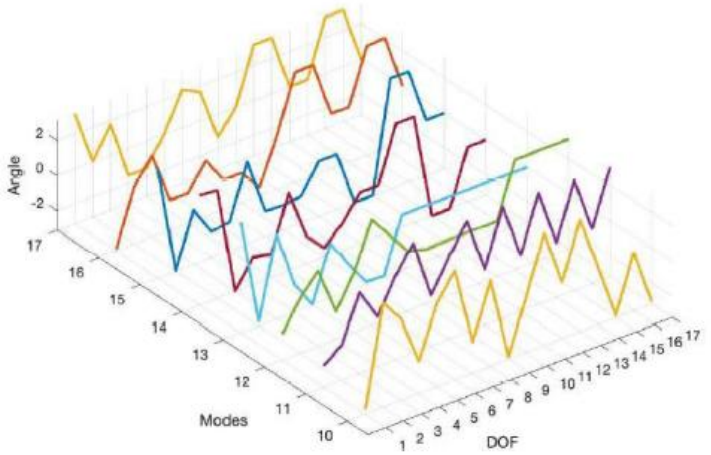

Figure 3.13: Phase of the 17 dof model's modal vectors for Wheels

3.2 *DYNAMIC PROBLEM: FREQUENCY DOMAIN RESOLUTION*

The equation of motion of a n-dof damped system can be written in matrix form such as:

$$M\ddot{x}(t) + C\dot{x}(t) + Kx(t) = F(t) \tag{3.1}$$

where M, C and K are the mass, damping and stiffness matrices of the system, while $F(t)$ is the applied forces matrix. Moving on to the frequency domain we obtain:

$$-M\omega^2\boldsymbol{X}(\omega) + j\omega C\boldsymbol{X}(\omega) + K\boldsymbol{X}(\omega) = \boldsymbol{F}(\omega) \tag{3.2}$$

That can be rewritten as:

$$(-M\omega^2 + j\omega C + K)\boldsymbol{X}(\omega) = \boldsymbol{F}(\omega) \tag{3.3}$$

Defining:

$$K_d(\omega) = -M\omega^2 + j\omega C + K \tag{3.4}$$

which represents the dynamic stiffness matrix (or impedance matrix of the system), it is possible to obtain the solution of equation (3.2) as:

$$\boldsymbol{X}(\omega) = K_d^{-1}(\omega)\boldsymbol{F}(\omega) = H(\omega)\boldsymbol{F}(\omega) \tag{3.5}$$

where $H(\omega) = K_d^{-1}(\omega)$ is the *frequency response matrix* of the system. Appendix B describes how to proceed to obtain the matrix $\boldsymbol{F}(\omega)$ for the three models studied. At this point, the transforms of the system outputs are available, as well as the time histories, which can be obtained in the discrete case through the IFFT (*inverse fast Fourier transform*).

3.2.1 SYSTEM'S OUTPUT PSD

There are several ways to obtain PSDs of system response signals. First of all, it is possible to get the output auto-PSDs starting from 2.67, that is:

$$\boldsymbol{G_{xx}}^{th}(f) = \frac{1}{t_0}\left(\frac{|\boldsymbol{X}(f)|}{f_c}\right)^2 \tag{3.6}$$

$\boldsymbol{G_{xx}}^{th}(f)$is the system output auto-PSD matrix. It is made up of n columns equal to the number of dofs of the system considered and a number of rows equal to the number of elements of the frequency vector, i.e. $(f_c/\Delta f) + 1$.

3.2.2 RELATIONS BETWEEN INPUT AND OUTPUT

By indicating with $\boldsymbol{Y}(\omega)$ and $\boldsymbol{X}(\omega)$ respectively the Fourier transforms of system's inputs and outputs, (3.5) can be rewritten (incorporating the influence matrices in $\boldsymbol{H}(\omega)$, see appendix B) as:

$$\boldsymbol{X}(\omega) = \boldsymbol{H}(\omega)\boldsymbol{Y}(\omega) \tag{3.7}$$

This concept can be extended to the case of continuous signals. The output signal $x(t)$ can therefore be obtained from the inverse Fourier transform of (3.7):

$$x(t) = \int_{-\infty}^{+\infty} \left[\frac{1}{2\pi} \int_{-\infty}^{+\infty} y(t) e^{-j\omega t} dt \right] e^{j\omega t} d\omega \tag{3.8}$$

The term inside the square brackets is precisely the transform of $y(t)$, that is $\boldsymbol{Y}(\omega)$. However, this formulation is not widely used as the integral of the inverse Fourier transform in $d\omega$ is not easy to solve. Alternatively, the convolution integral technique can be used, which for a continuous random signal, assuming that it is formed by a series of small pulses, is:

$$x(t) = \int_{-\infty}^{+\infty} y(\tau) h(t-\tau) d\tau \tag{3.9}$$

where the impulse occurs at time τ and the response is evaluated at time t. Equivalently, if τ is defined as the time difference between which an impulse occurs and the moment in which its response is calculated, the same relation can be written as:

$$x(t) = \int_{-\infty}^{+\infty} h(\tau) y(t-\tau) d\tau \tag{3.10}$$

Usually the lower limit of the integral is set to zero as for $\tau < 0$ we have $h(\tau) = 0$, as it is not possible to have an output before the impulse occurs. There is an important link between the impulse response function $h(t)$ and the frequency response function $H(\omega)$.
Considering an impulsive input signal, $y(t) = \delta(t)$, and the corresponding output signal, $x(t) = h(t)$, the Fourier transform of the input signal will be:

$$\boldsymbol{Y}(\omega) = \frac{1}{2\pi} \int_{-\infty}^{+\infty} \delta(t) e^{-j\omega t} dt = \frac{1}{2\pi} \tag{3.11}$$

So the Fourier transform of the output is:

$$\boldsymbol{X}(\omega) = \frac{1}{2\pi} \int_{-\infty}^{+\infty} h(t) e^{-j\omega t} dt \tag{3.12}$$

Including (3.11) and (3.12) in (3.7), we obtain:

$$\boldsymbol{H}(\omega) = \int_{-\infty}^{+\infty} h(t) e^{-j\omega t} dt \tag{3.13}$$

Hence, $\boldsymbol{H}(\omega)$ is the Fourier transform of $h(t)$ (up to the factor $1/2\pi$, based on the definition of the Fourier transform).
Now you can get the input-output relationship for a single input single output (SISO) system. Considering a random input signal $y(t)$ and the corresponding output signal $x(t)$, we have:

$$x(t)x(t+\tau) = \int_0^{+\infty} \int_0^{+\infty} h(\xi)h(\eta)y(t-\xi)y(t+\tau-\eta)d\xi\, d\eta \tag{3.14}$$

And so, for the input-output relationship of the auto-correlation functions, we have:

$$R_{xx}(\tau) = \int_0^{+\infty} \int_0^{+\infty} h(\xi)h(\eta)R_{xx}(\tau-\eta)d\xi\, d\eta \tag{3.15}$$

Equivalently, for the cross-correlations we have:

$$y(t)x(t+\tau) = \int_0^{+\infty} h(\eta)y(t)y(t+\tau-\eta)d\eta \tag{3.16}$$

and

$$R_{yx}(\tau) = \int_0^{+\infty} h(\eta)R_{yy}(\tau-\eta)d\eta \tag{3.17}$$

Equations from (3.14) to (3.17) represent the convolution of the input signal with the corresponding impulse response function. Applying the Fourier transform to (3.15) and (3.17), we obtain:

$$S_{xx}(\omega) = |H(\omega)|^2 S_{yy}(\omega) \tag{3.18}$$

and

$$S_{yx}(\omega) = H(\omega)S_{yy}(\omega) \tag{3.19}$$

The first of the two equations is a real function and contains information regarding the magnitude of the frequency response function. $S_{yy}(\omega)$ and $S_{xx}(\omega)$ represent the auto-PSDs of the input and output signals. The second equation, on the other hand, is a complex function and carries information both on the module and on the phase.
If we want to extend equation (3.18) to the case of a system subjected to random vibrations with N inputs, we have:

$$S_{xx}(\omega) = \sum_{p=1}^{N} \sum_{q=1}^{N} H_p^*(\omega)H_q(\omega)S_{y_p y_q}(\omega) \tag{3.20}$$

where $H_p^*(\omega)$ is the complex and conjugate of $H_q(\omega)$.
In the discrete case, and therefore also for the considered train models, it is possible to obtain a matrix relationship that allows to obtain the PSD matrix of the complete outputs starting from the PSD of the road profile. In this case, unlike what we saw in subsection 3.2.1, the PSD matrix contains both auto-correlation and cross-correlation terms.

The relationship is as follows:

$$G_{out}(\omega_i) = H(\omega_i)[j\omega_i T_1' + T_2']G_{in}(\omega_i)[j\omega_i T_1' + T_2']^H H^H(\omega_i) \tag{3.21}$$

where the matrix $H^H(\omega_i)$ is the Hermitian of $H(\omega_i)$ of dimension $n_{dof} \times n_{dof}$. Matrices T_1' and T_2' have dimension $n_{dof} \times n_{input}$ while the PSD matrix of the inputs $G_{in}(\omega_i)$ is an $n_{input} \times n_{input}$. Finally, the PSD matrix of the outputs $G_{out}(\omega_i)$ is a $n_{dof} \times n_{dof}$. The matrices for the different models are shown in appendix *C*. In the construction of the PSD matrix of the inputs, it is necessary to take into account what has been seen in subsection 2.3.2 regarding the temporal phase shift and the correlation between left and right profile.

3.2.3 WELCH PERIODOGRAM AND HALF SPECTRA METHOD

In signal theory, the *periodogram* is a non-parametric estimate of the spectral density of a stationary random signal. It exploits the discrete Fourier transform. For a signal $x(n)$ sampled with a frequency f_c, denoting by $P(f)$ the PSD, the periodogram is defined as:

$$\hat{P}(f) = \frac{\Delta t}{N}\left[\sum_{n=0}^{N-1} x(n)e^{-j2\pi f \Delta t n}\right]^2, \quad -1/2\Delta t < f \leq 1/2\Delta t \tag{3.22}$$

where Δt is the sampling interval. However the periodogram is not a consistent estimate of the PSD. In fact it is shown that by increasing the resolution in frequency, making the number of samples N tend to infinity, the error of the estimate does not tend to 0. This limit is overcome by reducing the resolution in frequency, thus obtaining a reduction in the estimation error, resulting in smoother spectra. To do this, so-called modified periodograms are used, one of which is the Welch periodogram. It consists in operating an explicit windowing of the signal. In other words, the signal made up of N samples is divided into K parts, usually partially overlapping (*overlap*, usually by 50%). Each part into which the signal is divided is multiplied by a suitable window function that joints the edges of each interval to 0. At this point the respective spectra are calculated and the estimate is obtained as the average of the K spectra.
Among the most used window functions, there are the rectangular window function (3.14) and the Hanning window function (3.15).

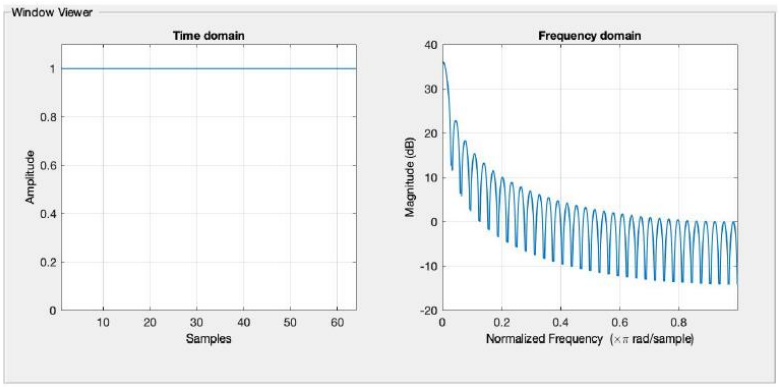

Figure 3.14: Rectangular Windowing function

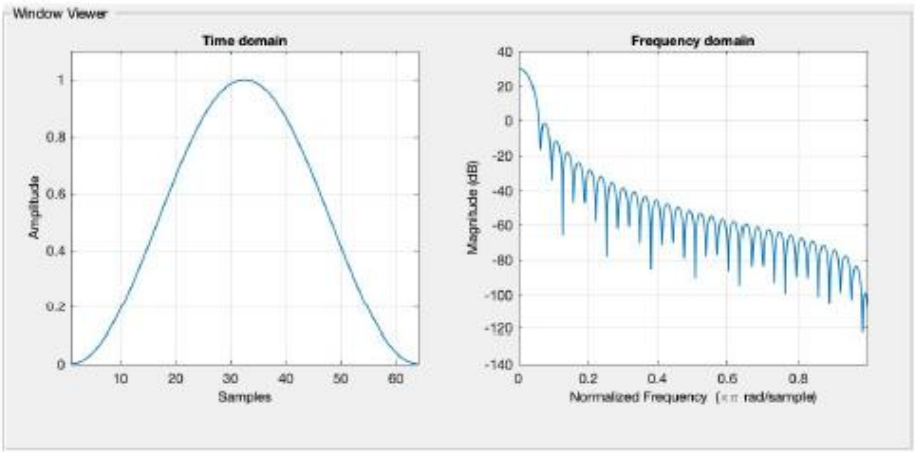

Figure 3.15: Hanning Windowing function

There is also another way to obtain the estimate of the PSD. First of all it is possible to estimate the correlation matrix R_i of the output signals of the system $x(n)$ as:

$$R_i = \frac{1}{N}\sum_{n=1}^{N-1} x(n+i)x^T(n) \tag{3.23}$$

where i indicates the index of the correlation sample (also referring to the time lag). The so-called weighted correlogram can be used as an estimate of the non-parametric spectrum, calculated as the discrete Fourier transform (DFT) of the weighted estimated correlation matrix in equation 3.23:

$$S_{xx}(\omega) = \sum_{n=-L}^{L} \omega_n R(n) e^{-j\omega n\Delta t} \tag{3.24}$$

where L indicates the maximum number of time lags through which the correlation function is estimated, while ω_n indicates the used weighting time window. Since negative time-shift correlation samples contain redundant information, it is sufficient to consider only positive time delays when calculating spectra, leading to so-called *half spectra*:

$$S_{xx}^{+}(\omega) = \frac{\omega_0 R(0)}{2}\sum_{n=1}^{L} \omega_n R(n) e^{-j\omega n\Delta t} \tag{3.25}$$

The advantage of the correlogram approach is that you can avoid the use of windowing operation. This operation through the Hanning function, for example, introduces an error on the damping estimates. Therefore, it is possible to apply an exponential window to the correlation functions before calculating the DFT, to reduce the effect of dispersion and the influence of higher time delays, which have a greater variance.

4 IDENTIFICATION THROUGH MODELS' DATA

To identify the data obtained from the 6 and 10 dof half-train and 17 dof full-train models, we will proceed by analyzing some cases, for each of which the results obtained using the OMA method will be shown [4]. For each case, some elements of the estimated PSD matrix of the rail profile will be shown. The visualization of the results obtained through the OMA will take place by means of:

- stabilization diagram (classic OMA and modified OMA);
- comparison tables between imposed and estimated modal parameters of the model;
- MAC and COMAC charts;
- comparison tables between imposed and estimated profile parameters;
- comparison between the PSDs of the estimated and theoretical profile.

The same cases will be analyzed using the Gonzalez method [7]. We will also see how the results vary when background noise is added to the processed signals with a certain ratio between the signal strength and the noise power (*Signal to Noise Ratio*, or *SNR*) defined as:

$$10 \cdot \log_{10} \frac{\sigma^2_{[Y(t)]}}{\sigma^2_{[Y_{noise}(t)]}} \; [dB] \tag{4.1}$$

4.1 *CASE 1*

The first case analyzed takes into consideration the 6 dof half-train model, with a rail profile obtained using the Sussman approximation as input, a vehicle speed of 25 m/s and a sampling frequency of 200 Hz.

4.1.1 OMA METHOD

In figure 4.1 are shown some elements of the output PSD matrix obtained through the (3.21). The input is a Sussman Class A profile. Note the sawtooth phase trend of the cross-PSD, in particular the term $(3,5)$that correlates the vertical displacements of the two bogies.
The stabilization diagram obtained applying the classic OMA at the polynomial model (2.84) is shown in figure 4.2. Evidently, in the frequency range considered, no poles have been identified. The stabilization diagram obtained applying the modified OMA at the polynomial model (2.88) is shown in figure 4.3, while figure 4.4 shows a focused detail around 11.95 Hz to better recognize two distinct poles that are very close one to another. Each pole is represented through a column of letters, that indicates if the pole stabilizes for that polynomial order. The letter s denotes that the pole stabilizes in terms of frequency, damping ratio and mode shapes, while the letter o denotes a new pole.
Using the modified OMA in a frequency band up to$50\ Hz$we detected 5 poles, differently to the 6 poles obtained through the theoretical model. This happened due to the superimposition of modes 5 and 6, so not easy to be distinguished by the polynomial model. Anyway, all poles detected stabilizes starting from orders even lower than 15.

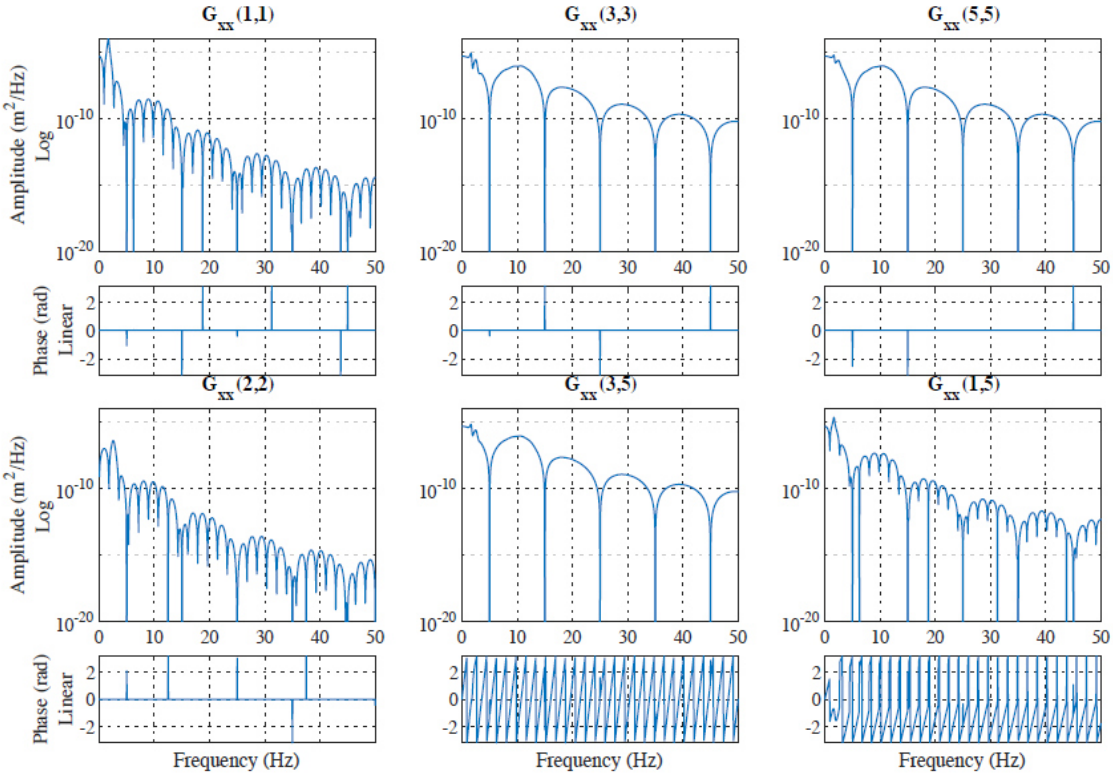

Figure 4.1: Modulus and phase of some elements of the output PSD matrix

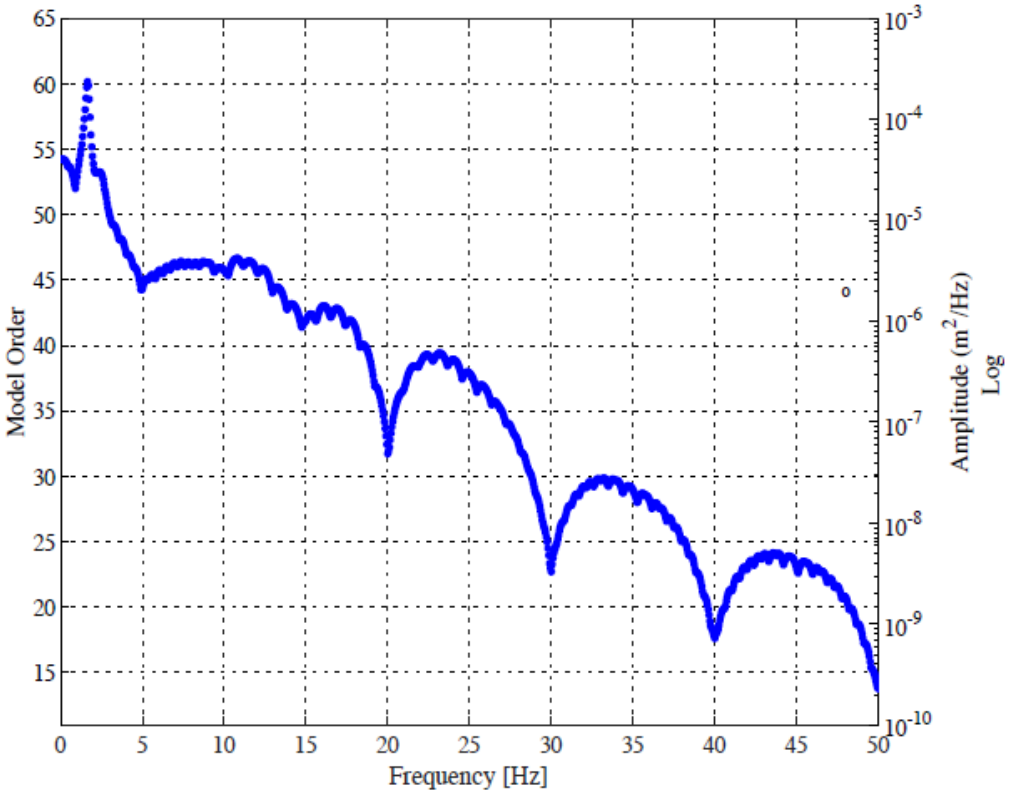

Figure 4.2: Classic OMA stabilization diagram

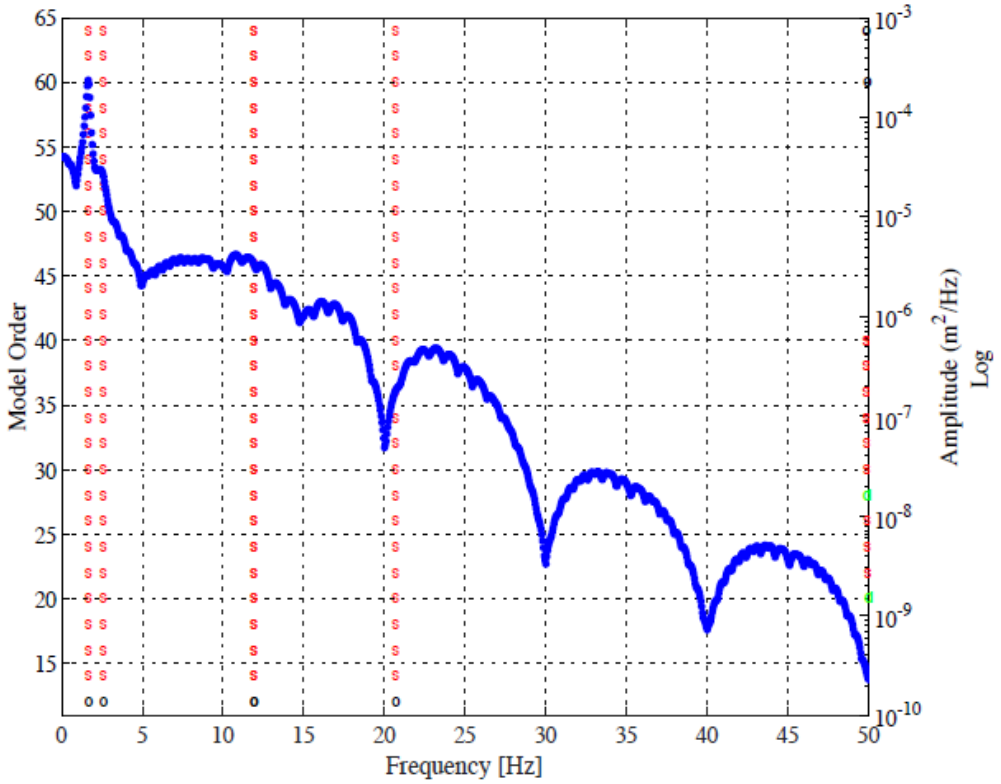

Figure 4.3: Modified OMA stabilization diagram

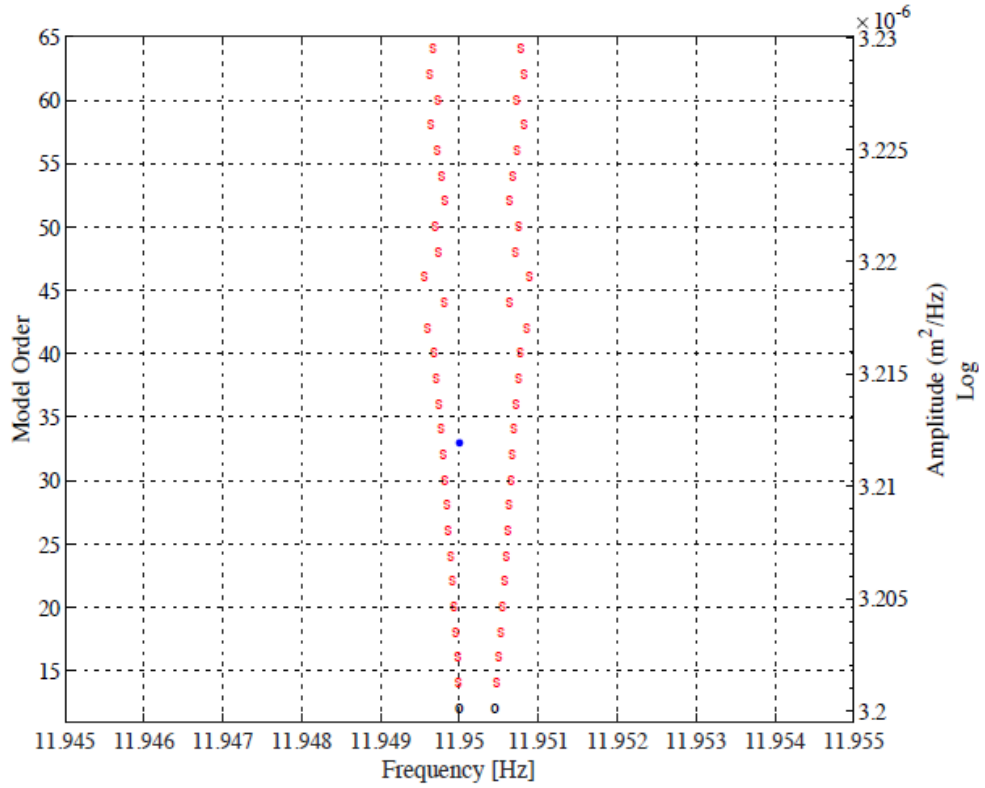

Figure 4.4: Detail of modified OMA stabilization diagram

Table 4.1 shows the natural frequencies and the estimated damping ratios, compared with those obtained from the model and an indication of the relative percentage error. The estimated values have a very small error compared to the reference values.

f_{ref} $[Hz]$	f_{est} $[Hz]$	$err(f)$ [%]	ζ_{ref}	ζ_{est}	$err(\zeta)$ [%]
1.6839	1.6839	$1.1416 \cdot 10^{-6}$	8.2485	8.2485	$2.283 \cdot 10^{-6}$
2.6081	2.6080	$2.7127 \cdot 10^{-5}$	12.628	12.628	0.0002
11.9501	11.9497	0.0036	21.8747	21.8749	0.0013
11.9503	11.9508	0.004	22.5526	22.5527	0.0005
20.7077	20.7078	0.0003	21.0611	21.0607	0.0015

Table 4.1: Comparison between model's and estimated values of natural frequencies and damping ratios

In figure 4.5 it is possible to see the comparison between the system modes of the reference model and the estimated ones, also with the help of the MAC and COMAC graphs.
The MAC assumes values equal to 1 in the terms that relate the estimated modal vectors with the corresponding design vector, therefore the coherence is maximum.
COMAC shows how degree of freedom 4 (front bogie's pitch) contributes negatively to the estimate. This information confirms the problem encountered in the failure to identify a pole. In fact, the coincident poles corresponding to modes 5 and 6 refer to the pitches of the two bogies.

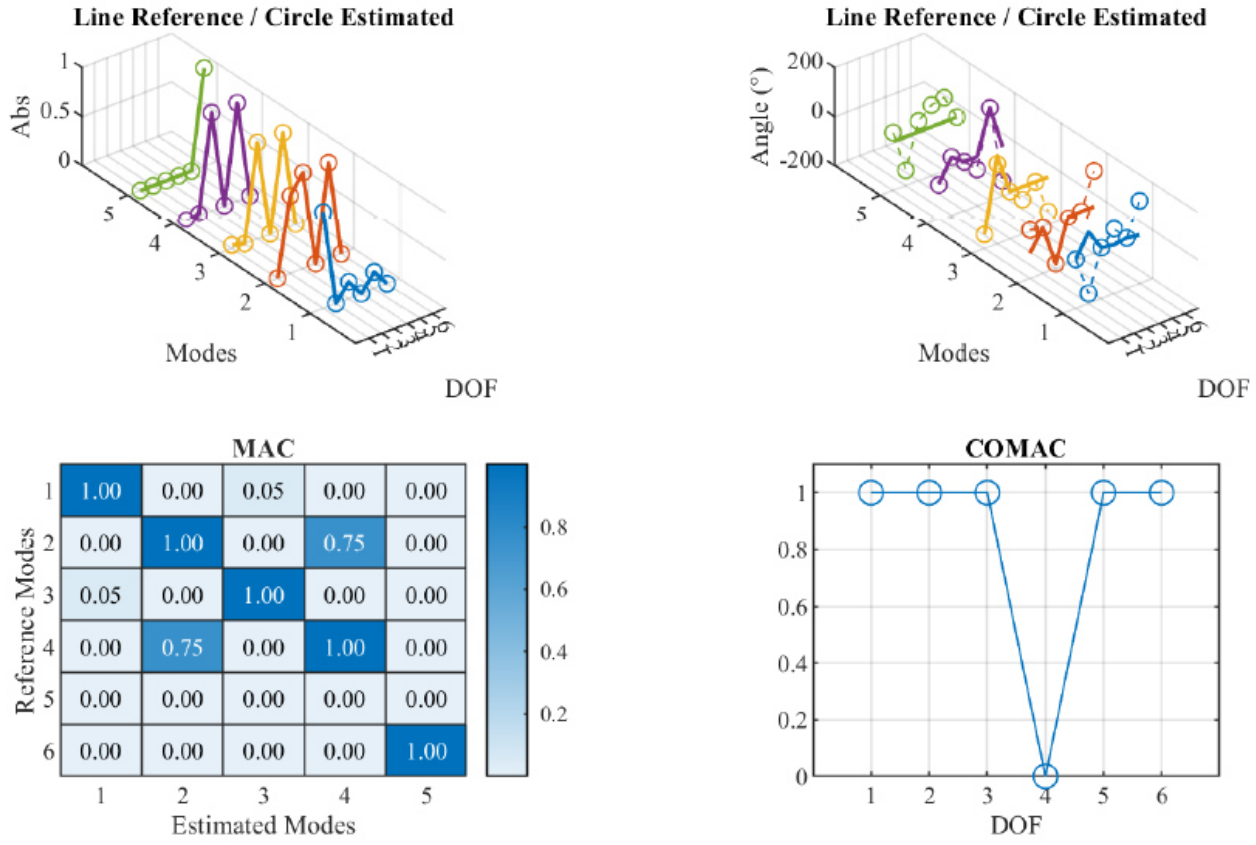

Figure 4.5: Comparison among the model's and estimated modes, MAC and COMAC

Table 4.2 shows the comparison between the parameters of the profile $G_d(f_0) = G_d(n_0) \cdot u$ (with $f_0 = n_0 \cdot u$) used in (2.59) and those estimated with the OMA method with indication of the relative percentage error.

$G_d(f_0)_{ref}$	$G_d(f_0)_{est}$	$err[G_d(f_0)]$ [%]	$f_{0_{ref}}$	$f_{0_{est}}$	$err(f_0)$ [%]
$\mathbf{2.7945 \cdot 10^{-5}}$	$2.7961 \cdot 10^{-5}$	0.05807	2.500	2.500	0.0012

Table 4.2: Comparison between model's and estimated profile's parameters

Finally in figure 4.6 it is possible to see the comparison between the PSD of the theoretical profile and the estimated one. In the same graph there is also the output auto-PSD corresponding to degree of freedom 5, that is the shaking of one of the bogies, which in the 6 dof model represents one of the points of contact with the track. Note how for low frequencies the three curves are practically superimposed, while for higher frequencies the output auto-PSD deviates. As will be reiterated later, in dealing with the interaction between wheels and profile, the PSD of the output signals can often be approximated to the PSD of the profile itself. This is because the stiffness value of the wheels of railway vehicles is very high and therefore there is a nearly unitary transmissibility of the stresses coming from the profile; this implies a high similarity between the input and output PSDs, especially at low frequencies and a greater deviation at higher frequencies. This last effect, in the case of the considered 6 dof system, is much more marked because each contact point is modeled by means of a spring and damper in parallel. As will be seen in the following cases, when the contact point is modeled exclusively with a spring with a high constant k there is a greater similarity even at higher frequencies.

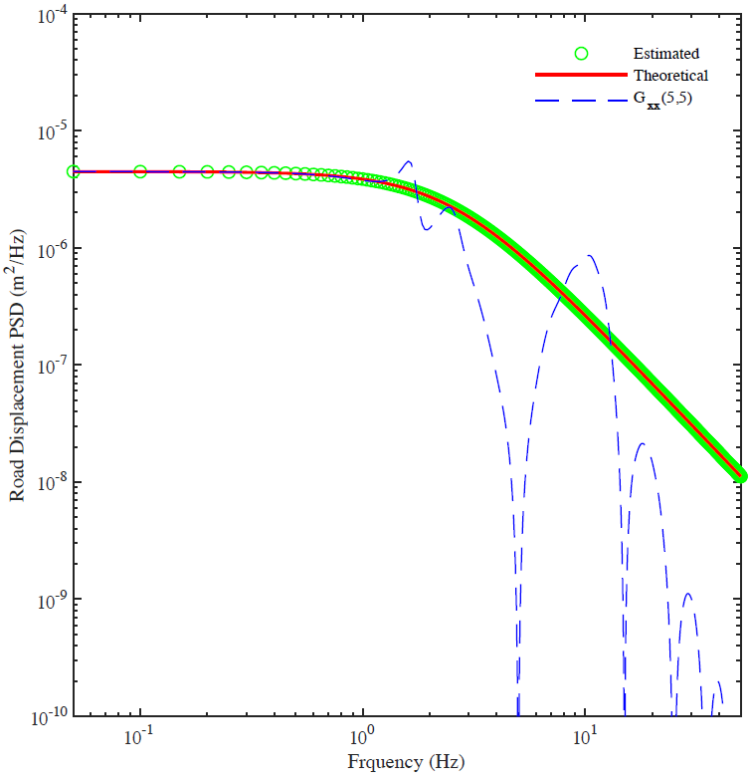

Figure 4.6: Comparison among the theoretical and estimated PSD

4.1.2 GONZALEZ METHOD

With reference to the diagram of figure 2.32, the method is applied considering a rail profile obtained by Sussman approximation of Class A for calibration, and a profile of Class D for verification. To obtain the matrix of the transfer function $\boldsymbol{H_t(f)}$ we use the relation:

$$H_t(f) = \frac{PSD_{out}(f)}{PSD_r(f)} \tag{4.2}$$

For the element $(3,5)$ of figure 4.1 we obtain the transfer function shown in figure 4.7.

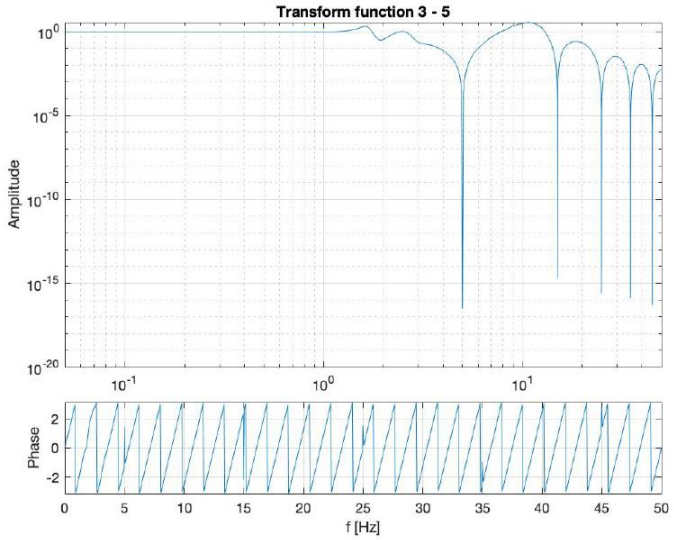

Figure 4.7: Transfer function H_t of the element $(3,5)$

In figure 4.8 it is possible to appreciate the comparison between the PSD of the estimated rail profile and the theoretical one, as well as with the auto-PSD of the element $(5,5)$.

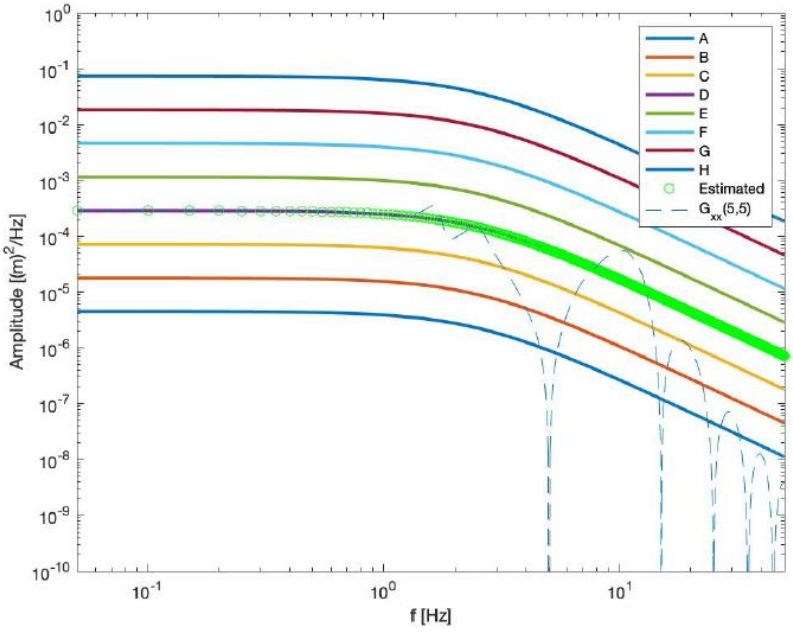

Figure 4.8: Comparison among the theoretical and estimated PSD

By means of a non-linear fitting it is possible to estimate the parameters of the profile and compare them with those of the Class D profile; this comparison is shown in table 4.3.

$G_d(f_0)_{ref}$	$G_d(f_0)_{est}$	$err[G_d(f_0)]$ [%]	$f_{0_{ref}}$	$f_{0_{est}}$	$err(f_0)$ [%]
$\mathbf{1.7885 \cdot 10^{-3}}$	$1.7885 \cdot 10^{-3}$	$2.1559 \cdot 10^{-6}$	2.500	2.500	$9.9713 \cdot 10^{-7}$

Table 4.3: Comparison between model's and estimated profile's parameters

From the comparison of the curves and parameters, the estimates obtained show a very small error compared to the reference values.
At this point it is possible to repeat the same procedure, with the addition of background noise with $SNR = 20dB$ to the historical output signals (figure 4.9). And through equation (4.2) we obtain the matrix $\boldsymbol{H_t}(f)$, of which the element (3, 5) is reported in figure 4.10.

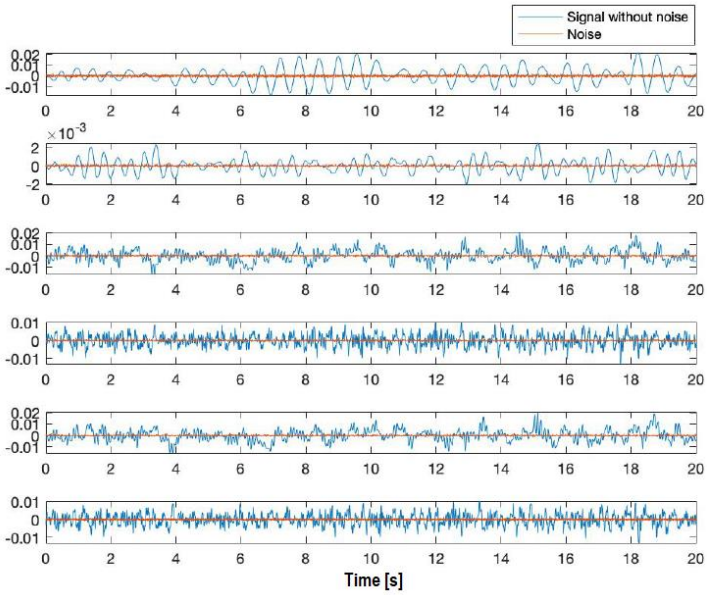

Figure 4.9: Time domain representation of the signal and the noise

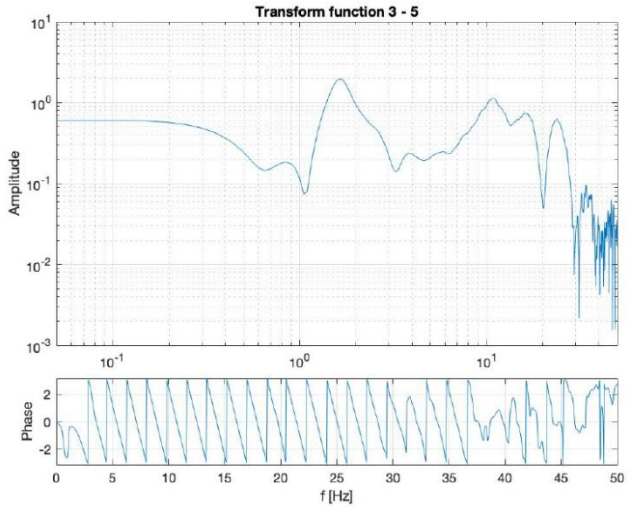

Figure 4.10: Transfer function H_t of the element $(3, 5)$ in case study with addiction of background noise

In table 4.4 is shown the comparison among the imposed and the estimated profile's parameters.

$G_d(f_0)_{ref}$	$G_d(f_0)_{est}$	$err[G_d(f_0)]$ [%]	$f_{0_{ref}}$	$f_{0_{est}}$	$err(f_0)$ [%]
$\mathbf{1.7885 \cdot 10^{-3}}$	$1.7887 \cdot 10^{-3}$	0.1007	2.500	2.4986	0.0568

Table 4.4: Comparison between model's and estimated profile's parameters

Figure 4.11 highlights the comparison between the PSD of the estimated profile, the theoretical one and the auto-PSD of the element $(5,5)$, in the case with background noise. Also in this case, despite the added noise, the estimates do not show large deviations from the reference values.

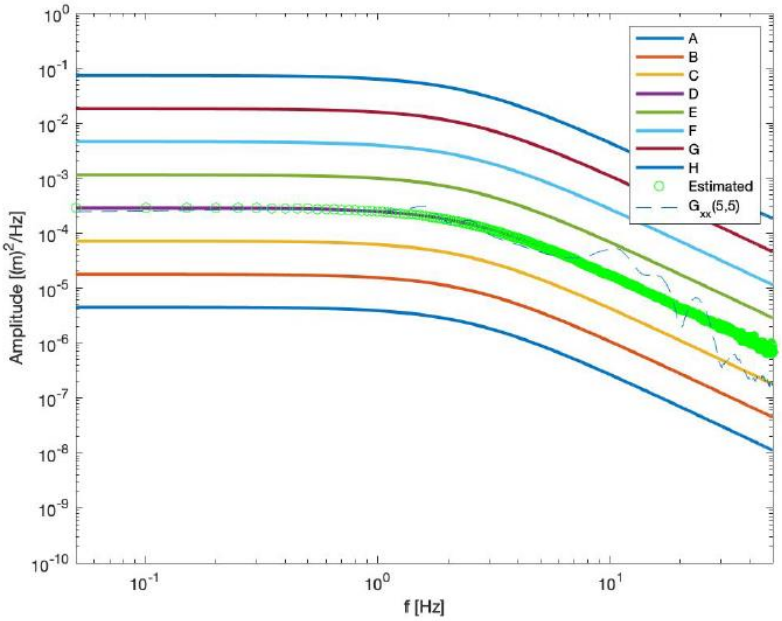

Figure 4.11: Comparison among the theoretical and estimated PSD with addiction of background noise

4.2 *CASE 2*

The second case analyzed takes into consideration the 10 dof half-train model, with a rail profile obtained using the Sussman approximation as input, a vehicle speed of 15 m/s and a sampling frequency of 200 Hz.

4.2.1 OMA METHOD

Figure 4.12 shows some elements of the PSD matrix of the outputs obtained with the relation (3.21). A profile obtained by Class B Sussman approximation was used as system input.

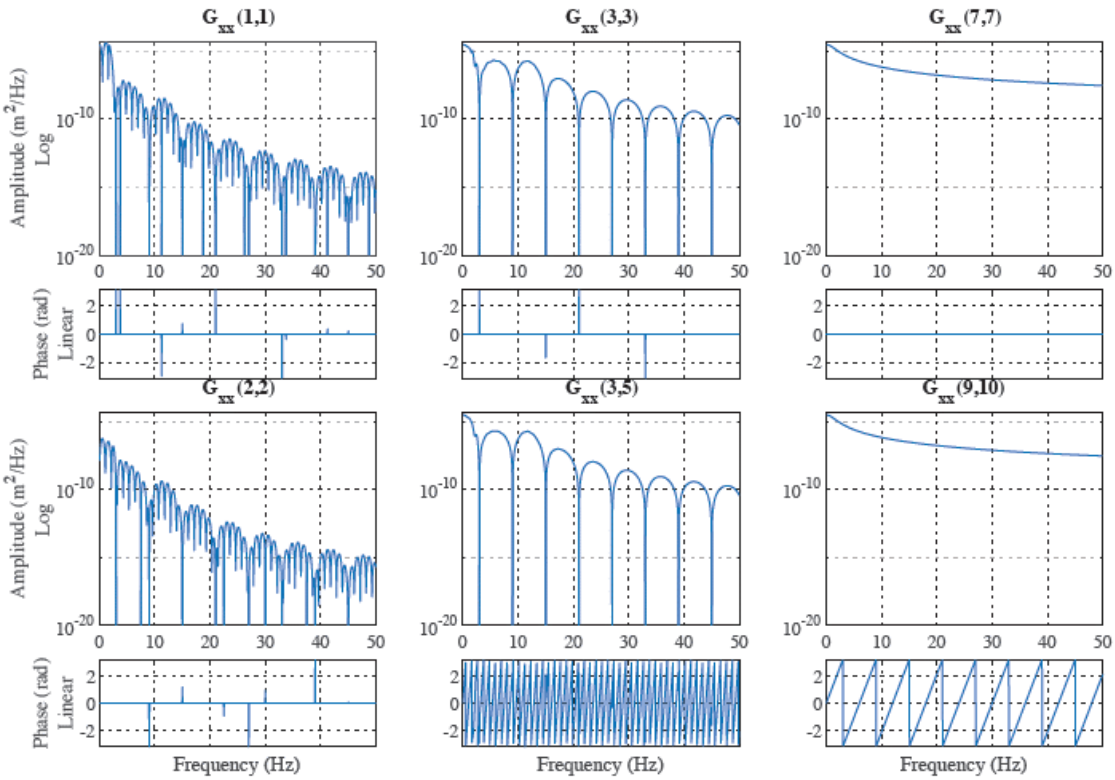

Figure 4.12: Modulus and phase of some elements of the output PSD matrix

The stabilization diagram obtained using the polynomial model of (2.88) of the modified OMA method is shown in figure 4.13.

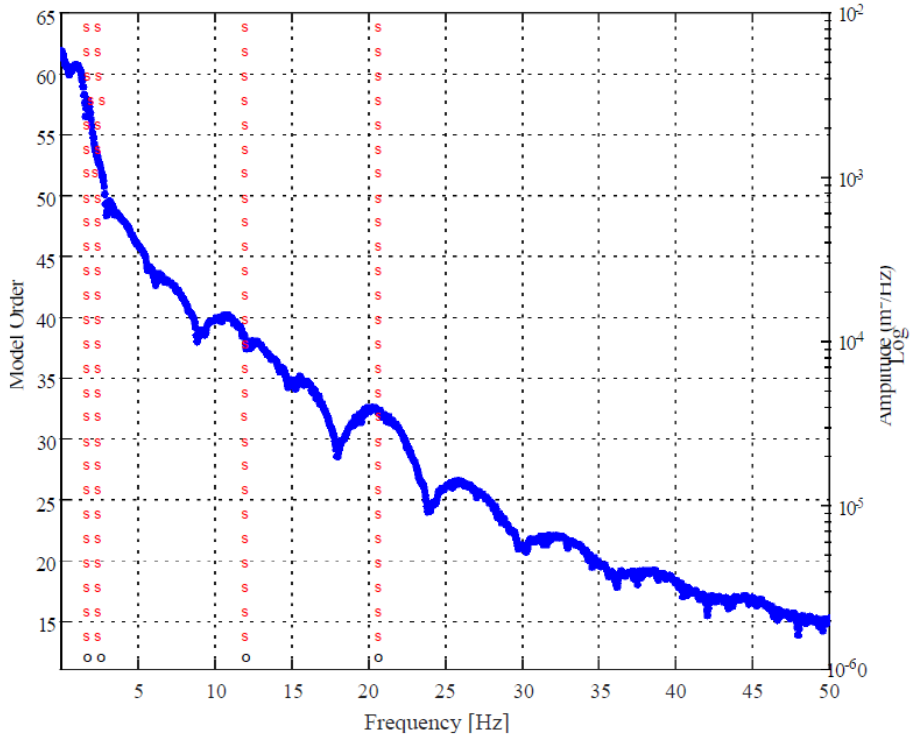

Figure 4.13: Modified OMA stabilization diagram

As in the previous case, the poles identified up to 50 Hz are 5, with the third and fourth very close, and the model was not able to distinguish those corresponding to the coincident modes 5 and 6. All poles stabilize with respect to natural frequencies, damping ratios and modes starting from an order of the polynomial model lower than 15.
Table 4.5 shows the natural frequencies and the estimated damping ratios compared with those obtained from the model and an indication of the relative percentage error.

f_{ref} [Hz]	f_{est} [Hz]	$err(f)$ [%]	ζ_{ref}	ζ_{est}	$err(\zeta)$ [%]
1.6835	1.6835	$5.7867 \cdot 10^{-7}$	8.2441	8.2441	$1.4483 \cdot 10^{-5}$
2.6076	2.6076	$1.3681 \cdot 10^{-5}$	12.6206	12.6207	0.0001
11.9406	11.9404	0.0011	21.8537	21.8527	0.0044
11.9408	11.9409	0.0011	22.5334	22.5346	0.0053
20.6903	20.6903	$1.2425 \cdot 10^{-5}$	21.0000	21.0000	$1.3571 \cdot 10^{-4}$

Table 4.5: Comparison between model's and estimated values of natural frequencies and damping ratios

In figure 4.14 it is possible to see the comparison between the system modes of the reference model and the estimated ones, also with the help of the MAC and COMAC graphs.
The MAC shows unitary coherence between vector and design modals, except for mode 5, which has $MAC = 0.22$ with reference to mode 5 and $MAC = 0.73$ with reference to mode 6; in fact, as anticipated, the poles of modes 5 and 6 are coincident and are not distinguished by the polynomial model. This is confirmed by the value $COMAC = 0$ for the pitch degree of freedom of the front bogie.

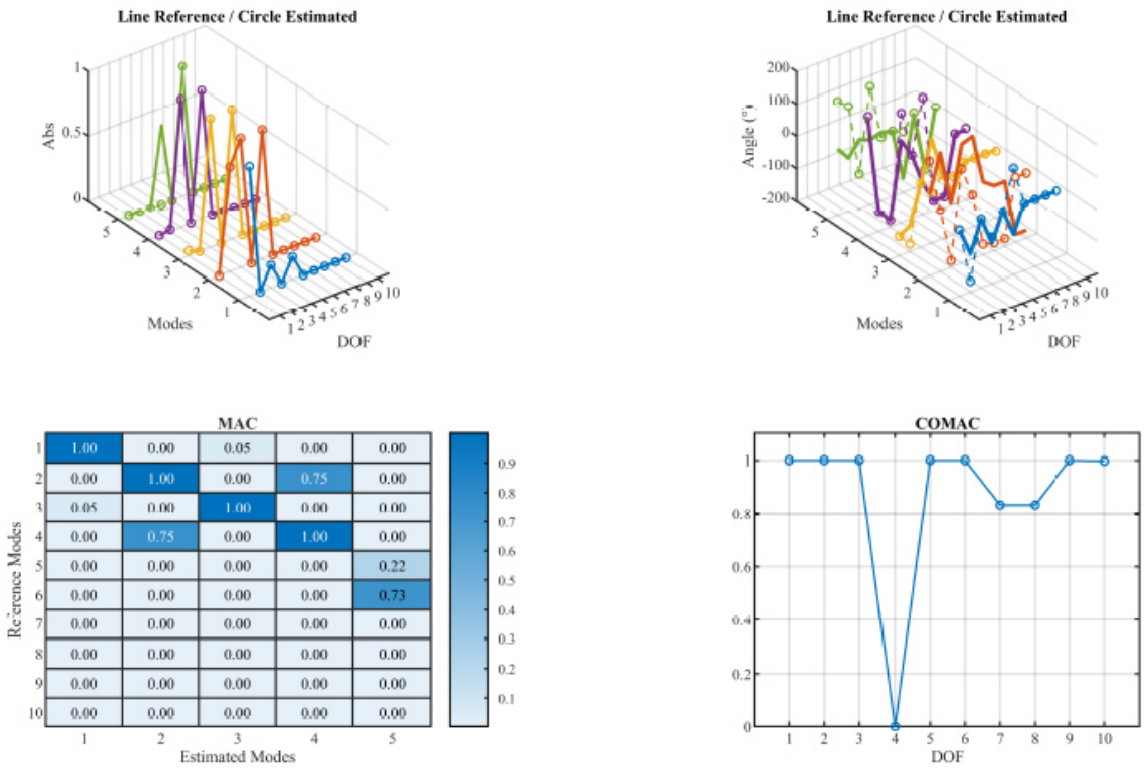

Figure 4.14: Comparison among the model's and estimated modes, MAC and COMAC

Table 4.6 shows the comparison between the parameters of the $G_d(f_0)$ and f_0 profile used in (2.59) and those estimated with the OMA method with indication of the relative percentage error.

$G_d(f_0)_{ref}$	$G_d(f_0)_{est}$	$err[G_d(f_0)]$ [%]	$f_{0_{ref}}$	$f_{0_{est}}$	$err(f_0)$ [%]
$\mathbf{2.7135 \cdot 10^{-4}}$	$2.3943 \cdot 10^{-4}$	11.7621	1.500	1.4082	6.1171

Table 4.6: Comparison between model's and estimated profile's parameters

As in the previous case, in figure 4.15 it is possible to see the comparison between the PSD of the theoretical profile, the estimated one and the output auto-PSD corresponding to degree of freedom 7, i.e. the shaking of the wheel on the front axle. Note how compared to the previous case, the three curves are practically superimposed for the whole range of frequencies considered. As previously mentioned, since the contact point between the profile and the vehicle is modeled by means of a spring with very high stiffness (and in this case without a damper), the transmissibility of the stresses is near to one.

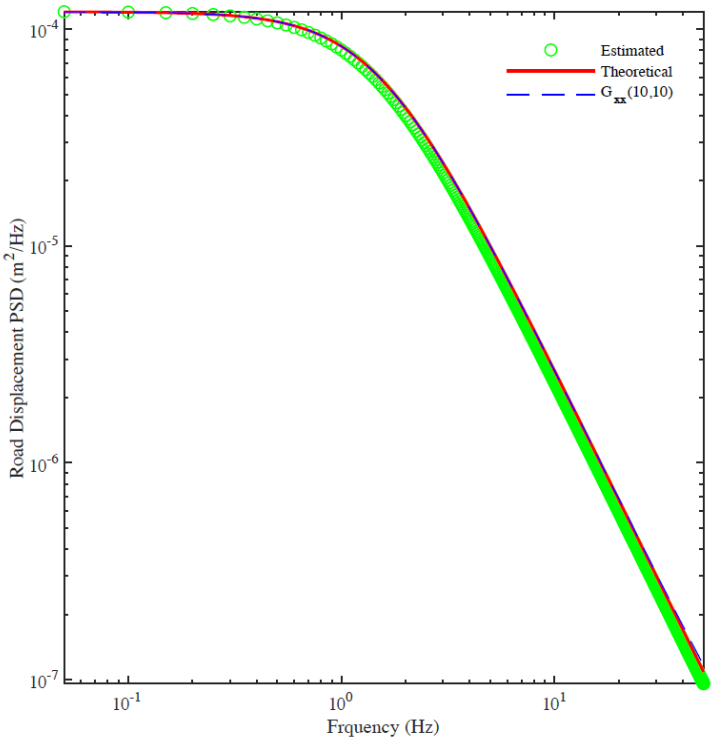

Figure 4.15: Comparison among the theoretical and estimated PSD

4.2.2 GONZALEZ METHOD

With reference to the diagram in figure 2.32, the method is applied considering a profile obtained by Sussman approximation of class B for calibration, and a profile of class E for verification. By exploiting the relation (4.2) it is possible to obtain the matrix of the transfer function $\boldsymbol{H_t}(f)$. For the element $(9, 10)$ of figure 4.12 we obtain the transfer function shown in figure 4.16.

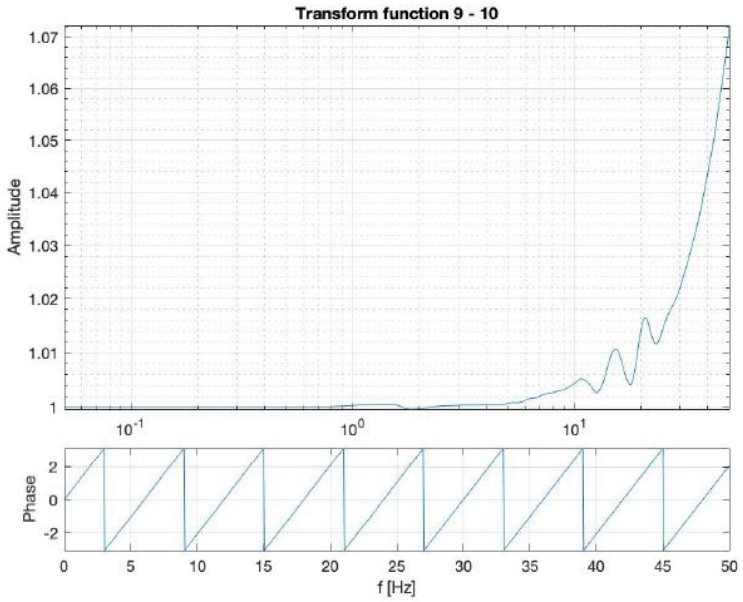

Figure 4.16: Transfer function H_t of the element $(9, 10)$

In figure 4.17 it is possible to appreciate the comparison between the PSD of the estimated rail profile and the theoretical one, as well as with the auto-PSD of the element $(7, 7)$.

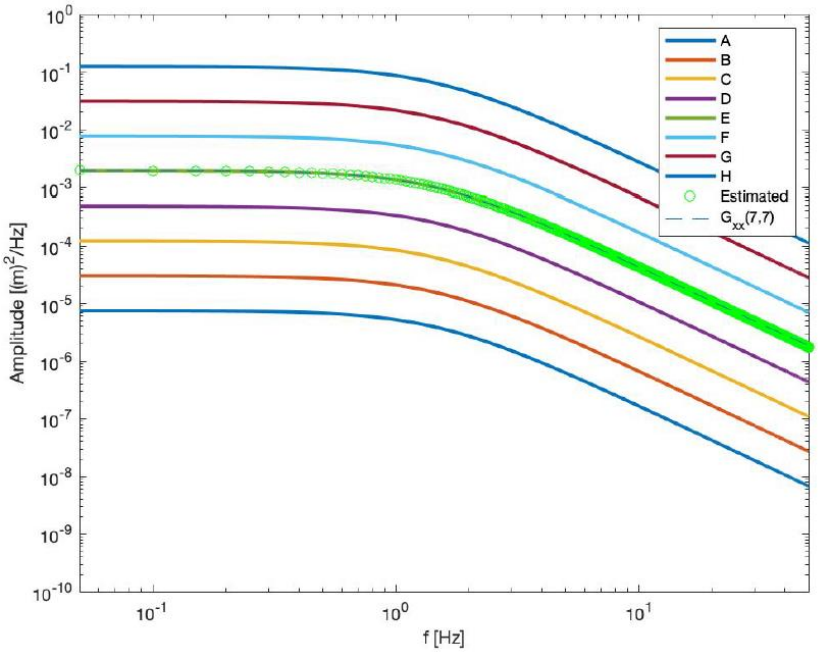

Figure 4.17: Comparison among the theoretical and estimated PSD

By means of a non-linear fitting it is possible to estimate the parameters of the profile and compare them with those of the Class E profile; this comparison is shown in table 4.7.

$G_d(f_0)_{ref}$	$G_d(f_0)_{est}$	$err[G_d(f_0)]$ [%]	$f_{0_{ref}}$	$f_{0_{est}}$	$err(f_0)$ [%]
$\mathbf{4.3395 \cdot 10^{-3}}$	$4.3395 \cdot 10^{-3}$	$3.0876 \cdot 10^{-6}$	1.500	1.500	$2.0551 \cdot 10^{-6}$

Table 4.7: Comparison between model's and estimated profile's parameters

From the comparison of the curves and parameters, the estimates obtained show a very small error compared to the reference values.
At this point it is possible to repeat the same procedure, with the addition of background noise with $SNR = 20dB$ to the historical output signals (figure 4.18). Then, through equation (4.2) we obtain the matrix $\boldsymbol{H_t}(f)$, of which the element $(9, 10)$ is reported in figure 4.19.

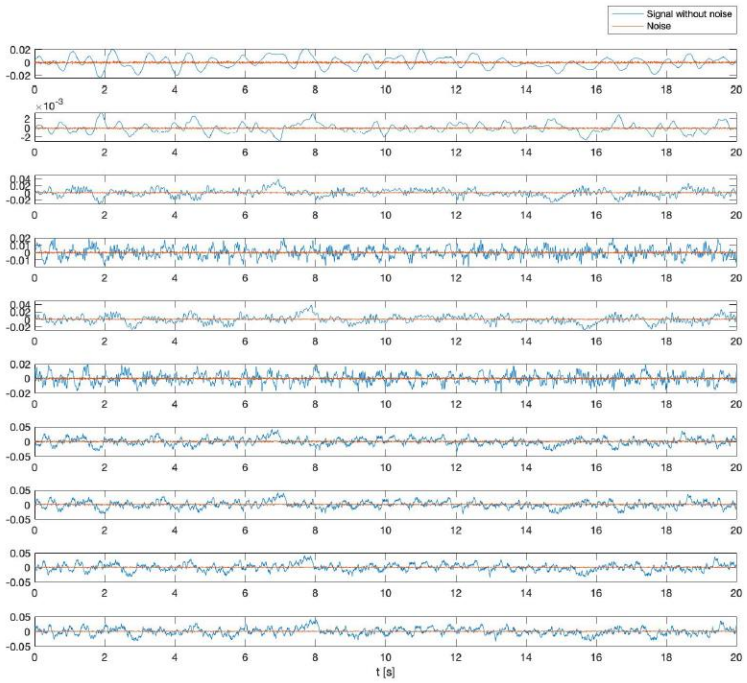

Figure 4.18: Time domain representation of the signal and the noise

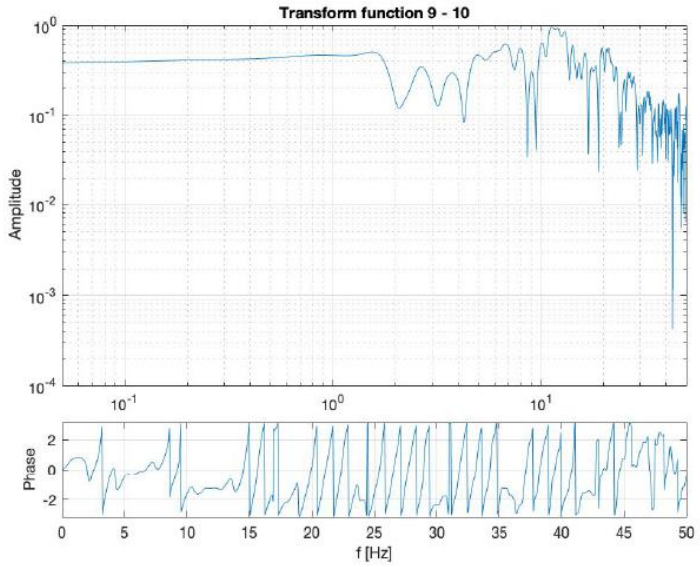

Figure 4.19: Transfer function H_t of the element $(9, 10)$ in case study with addiction of background noise

Figure 4.20 highlights the comparison between the PSD of the estimated roughness of the profile, the theoretical one and the auto-PSD of the element $(7,7)$, in the case with background noise, while in table 4.8 the comparison between parameters of the estimated profile and those of the imposed profile. Despite the addition of the noise to the response signals of the system, the estimates obtained are consistent with the expected values.

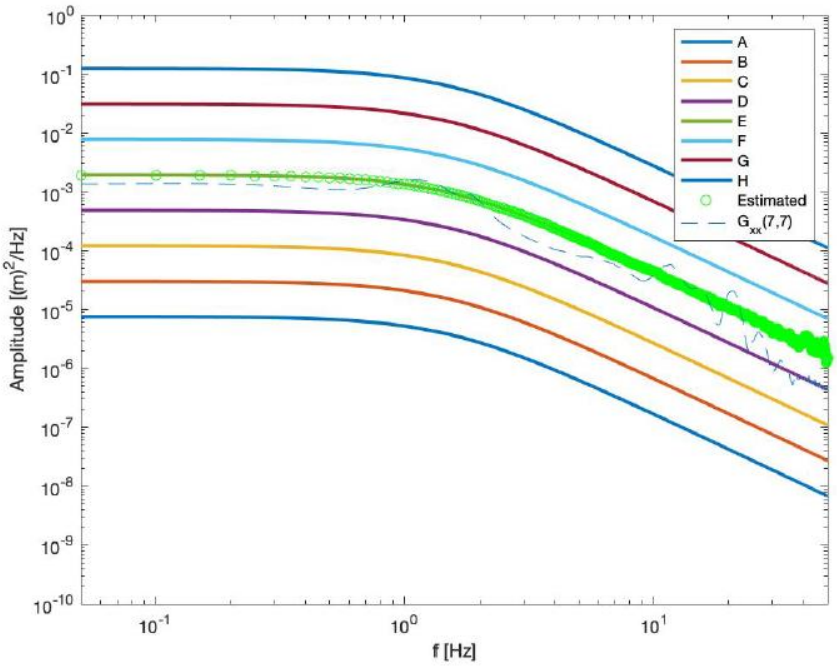

Figure 4.20: Comparison among the theoretical and estimated PSD with addiction of background noise

$G_d(f_0)_{ref}$	$G_d(f_0)_{est}$	$err[G_d(f_0)]$ [%]	$f_{0_{ref}}$	$f_{0_{est}}$	$err(f_0)$ [%]
$\mathbf{4.3395 \cdot 10^{-3}}$	$4.3206 \cdot 10^{-3}$	0.4359	1.500	1.4945	0.3648

Table 4.8: Comparison between model's and estimated profile's parameters

4.3 *CASE 3*

The third case analyzed takes into consideration the 17 dof full-train model, with a rail profile obtained using the Sussman approximation as input, a vehicle speed of 30 m/s and a sampling frequency of 200 Hz.

4.3.1 OMA METHOD

Figure 4.21 shows some elements of the PSD matrix of the outputs obtained with the relation (3.21). A profile obtained by Class C Sussman approximation was used as system input.

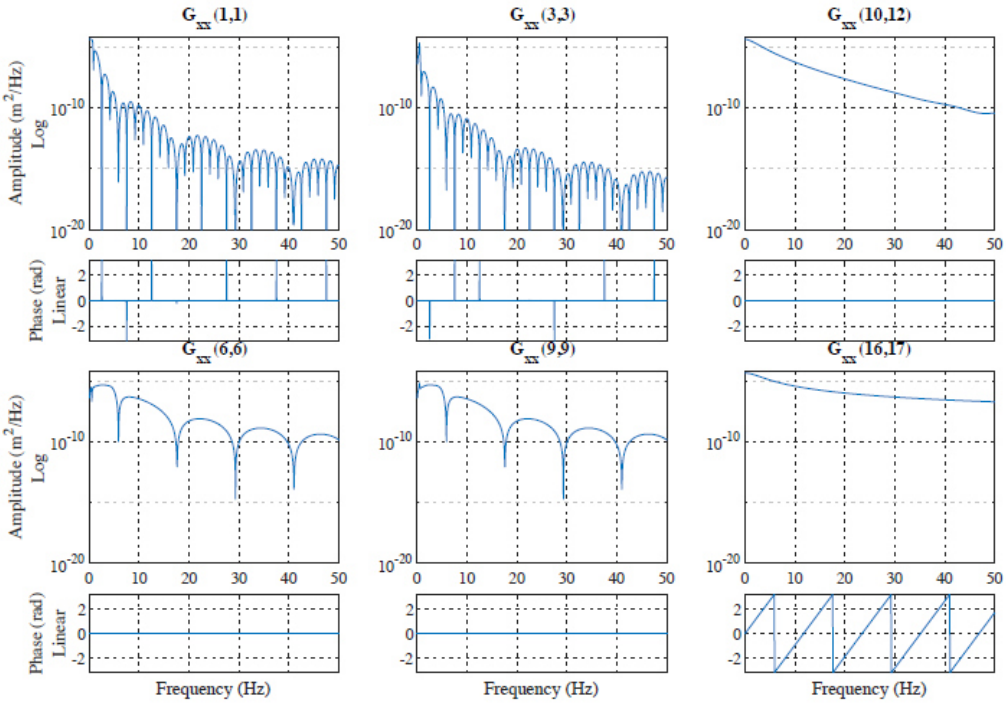

Figure 4.21: Modulus and phase of some elements of the output PSD matrix

The stabilization diagram obtained using the polynomial model of (2.88) of the modified OMA method is shown in figure 4.22.

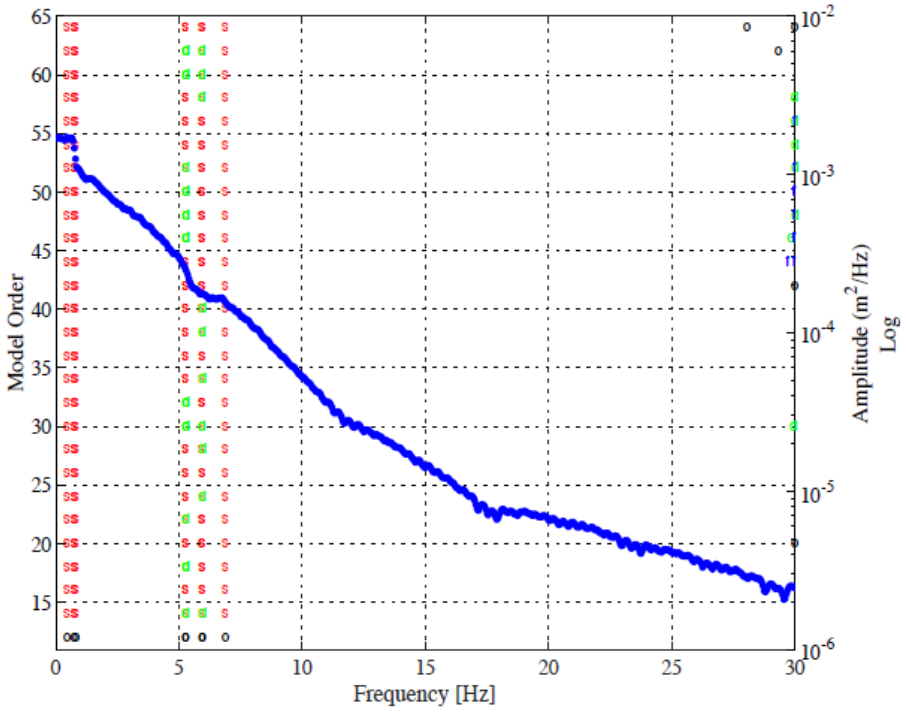

Figure 4.22: Modified OMA stabilization diagram

Notice how in this case, in addition to the letters s and o, the letter d is also present in the diagram. This indicates that, for that order of the model, the pole stabilizes in terms of damping ratio and modal shapes, but not in terms of natural frequency. The identified poles are 8, compared to the 9 expected. Also in this case, as confirmed by the MAC and COMAC values, the fact that the poles linked to the pitching modes of the bogies are coincident contributes negatively to the estimates.
Table 4.9 shows the natural frequencies and the estimated damping ratios compared with those obtained from the model and an indication of the relative percentage error.

f_{ref} $[Hz]$	f_{est} $[Hz]$	$err(f)$ [%]	ζ_{ref}	ζ_{est}	$err(\zeta)$ [%]
0.4586	0.4585	0.0205	12.8315	12.8066	0.1936
0.7351	0.7350	0.0168	18.7565	18.7574	0.0049
0.8268	0.8269	0.0075	21.0855	21.0742	0.0535
5.2589	5.2581	0.0157	19.8206	19.8197	0.0048
5.2642	5.2651	0.0177	20.0267	20.0280	0.0067
5.9393	5.9087	0.5154	38.6399	38.3517	0.7199
5.9404	5.9651	0.4160	38.7205	38.7897	01787
6.8865	6.8859	0.0086	36.0489	36.0636	0.0406

Table 4.9: Comparison between model's and estimated values of natural frequencies and damping ratios

In figure 4.23 it is possible to see the comparison between the system modes of the reference model and the estimated ones, also with the help of the MAC and COMAC graphs.

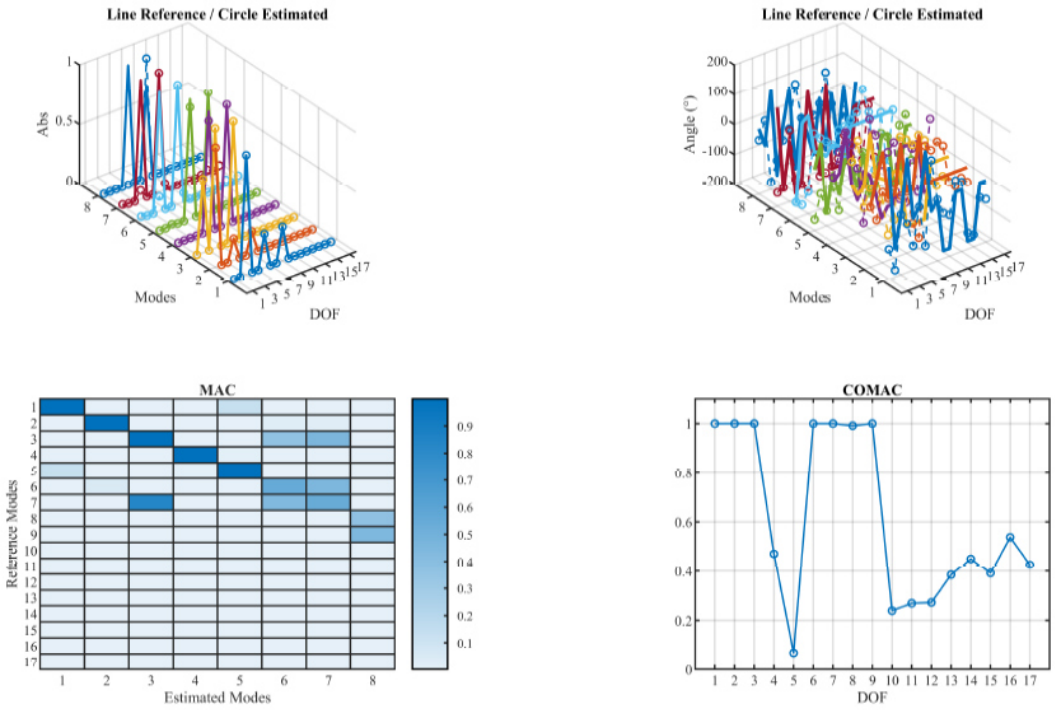

Figure 4.23: Comparison among the model's and estimated modes, MAC and COMAC

Table 4.10 shows the comparison between the parameters of the $G_d(f_0)$ and f_0 profile used in (2.59) and those estimated with the OMA method with indication of the relative percentage error.

$G_d(f_0)_{ref}$	$G_d(f_0)_{est}$	$err[G_d(f_0)]$ [%]	$f_{0_{ref}}$	$f_{0_{est}}$	$err(f_0)$ [%]
$\mathbf{4.6346 \cdot 10^{-4}}$	$4.7231 \cdot 10^{-4}$	1.9109	3	3.0286	0.9526

Table 4.10: Comparison between model's and estimated profile's parameters

In figure 4.24 it is possible to see the comparison between the PSD of the theoretical railway track, the estimated one and the output auto-PSD corresponding to the degree of freedom 10, i.e. the shaking of the left front wheel. Also in this case the three curves are practically superimposed for the whole range of frequencies considered.

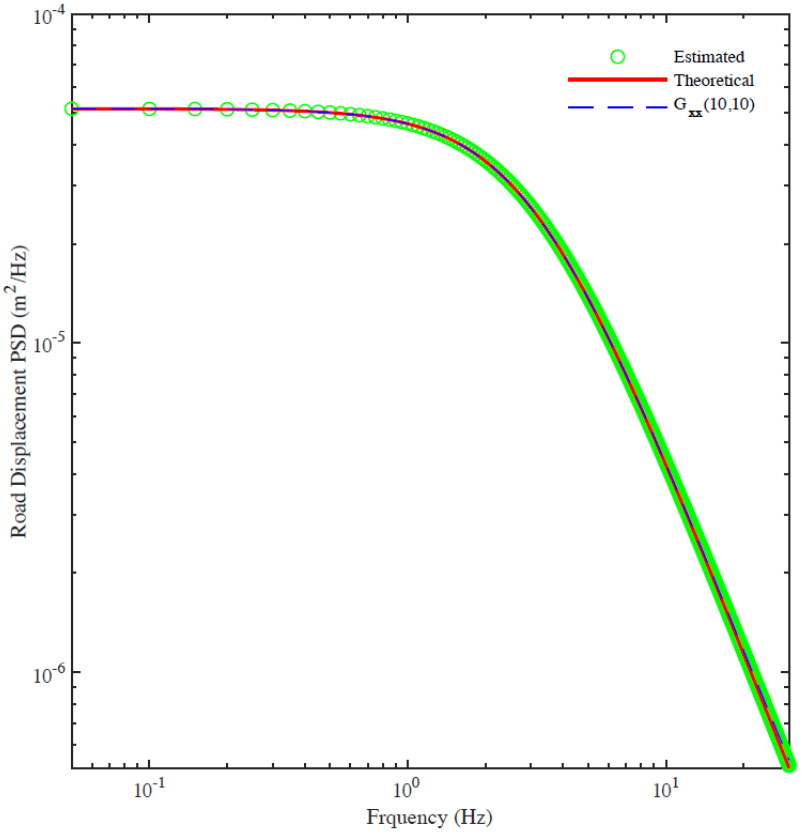

Figure 4.24: Comparison among the theoretical and estimated PSD

4.3.2 GONZALEZ METHOD

With reference to the diagram in figure 2.32, the method is applied considering a profile obtained by Sussman approximation of class C for calibration, and a profile of class F for verification. By exploiting the relation (4.2) it is possible to obtain the matrix of the transfer function $\boldsymbol{H_t}(f)$. For the element $(16, 17)$ of figure 4.21 we obtain the transfer function shown in figure 4.25.

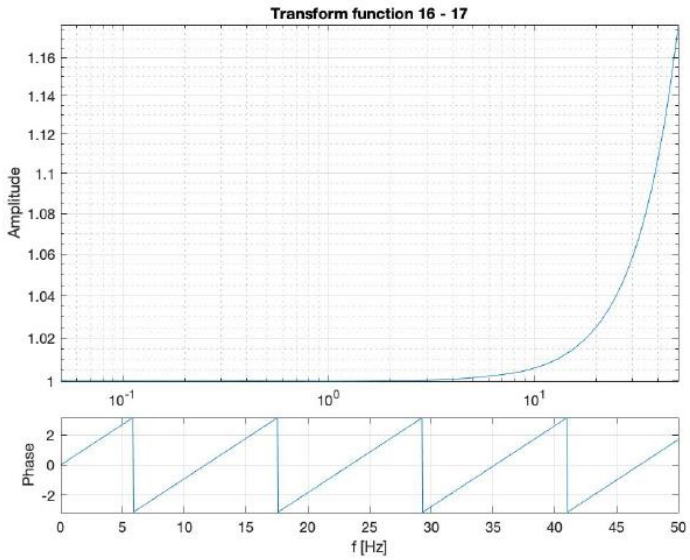

Figure 4.25: Transfer function H_t of the element $(16, 17)$

In figure 4.26 it is possible to appreciate the comparison between the PSD of the estimated rail profile and the theoretical one, as well as with the auto-PSD of the element $(16, 16)$. The three curves are almost completely superimposed in the considered frequency range.

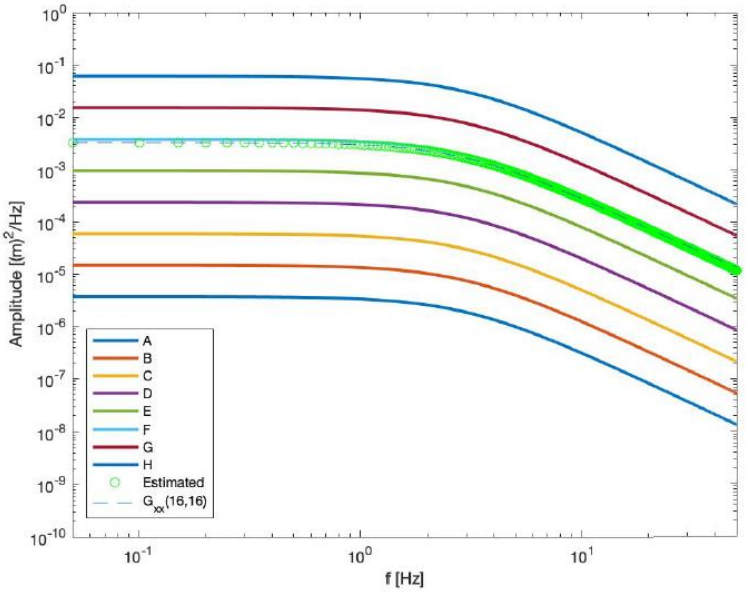

Figure 4.26: Comparison among the theoretical and estimated PSD

By means of a non-linear fitting it is possible to estimate the parameters of the profile and compare them with those of the Class F profile; this comparison is shown in table 4.11.

$G_d(f_0)_{ref}$	$G_d(f_0)_{est}$	$err[G_d(f_0)]$ [%]	$f_{0_{ref}}$	$f_{0_{est}}$	$err(f_0)$ [%]
$\mathbf{2.9661 \cdot 10^{-2}}$	$2.9661 \cdot 10^{-2}$	$2.7132 \cdot 10^{-10}$	3	3	$1.8039 \cdot 10^{-10}$

Table 4.11: Comparison between model's and estimated profile's parameters

From the comparison of the curves and parameters, the estimates obtained show a very small error compared to the reference values.
At this point it is possible to repeat the same procedure, with the addition of background noise with $SNR = 20dB$ to the historical output signals. Then, through equation (4.2) we obtain the matrix $\boldsymbol{H_t}(f)$, of which the element $(16, 17)$ is reported in figure 4.27.

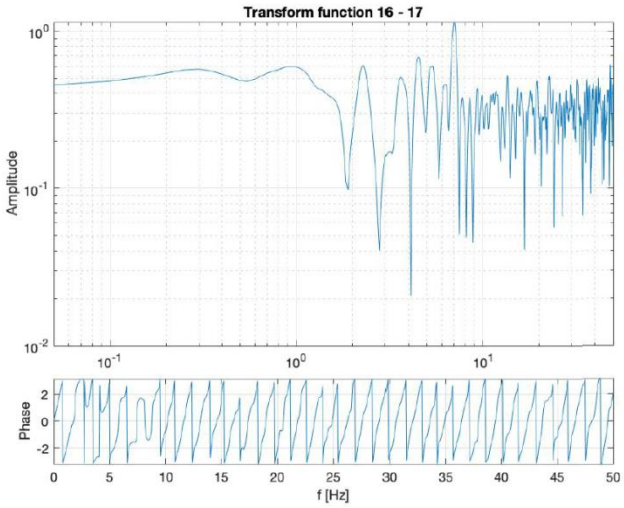

Figure 4.27: Transfer function H_t of the element $(16, 17)$ in the case of study with addiction of background noise

Figure 4.28 highlights the comparison between the PSD of the estimated roughness of the profile, the theoretical one and the auto-PSD of the element $(16, 16)$, in the case with background noise, while in table 4.12 the comparison between parameters of the estimated profile and those of the imposed profile. Despite the addition of the noise to the response signals of the system, the estimates obtained are consistent with the expected values.

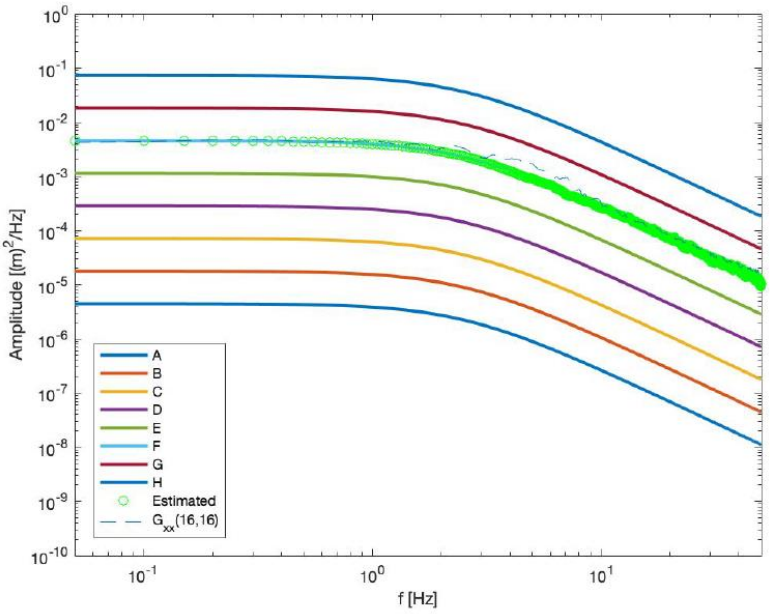

Figure 4.28: Comparison among the theoretical and estimated PSD with addiction of background noise

$G_d(f_0)_{ref}$	$G_d(f_0)_{est}$	$err[G_d(f_0)]$ [%]	$f_{0_{ref}}$	$f_{0_{est}}$	$err(f_0)$ [%]
$\mathbf{2.9661 \cdot 10^{-2}}$	$2.966 \cdot 10^{-2}$	0.0057	3	3.0045	0.1494

Table 4.12: Comparison between model's and estimated profile's parameters

Consider once again the 17 dof full-train model with a rail profile obtained with the FRA approximation and with a vehicle forward speed of 25 m/s and a sampling frequency of 200 Hz; applying the method considering a class 1 profile for calibration and a class 5 profile for verification.
Repeating the same procedure seen for the previous cases, the estimate of the PSD of the profile is obtained. Figure 4.29 shows the comparison between the estimated PSD, the theoretical one and the auto-PSD of the element $(16, 16)$.

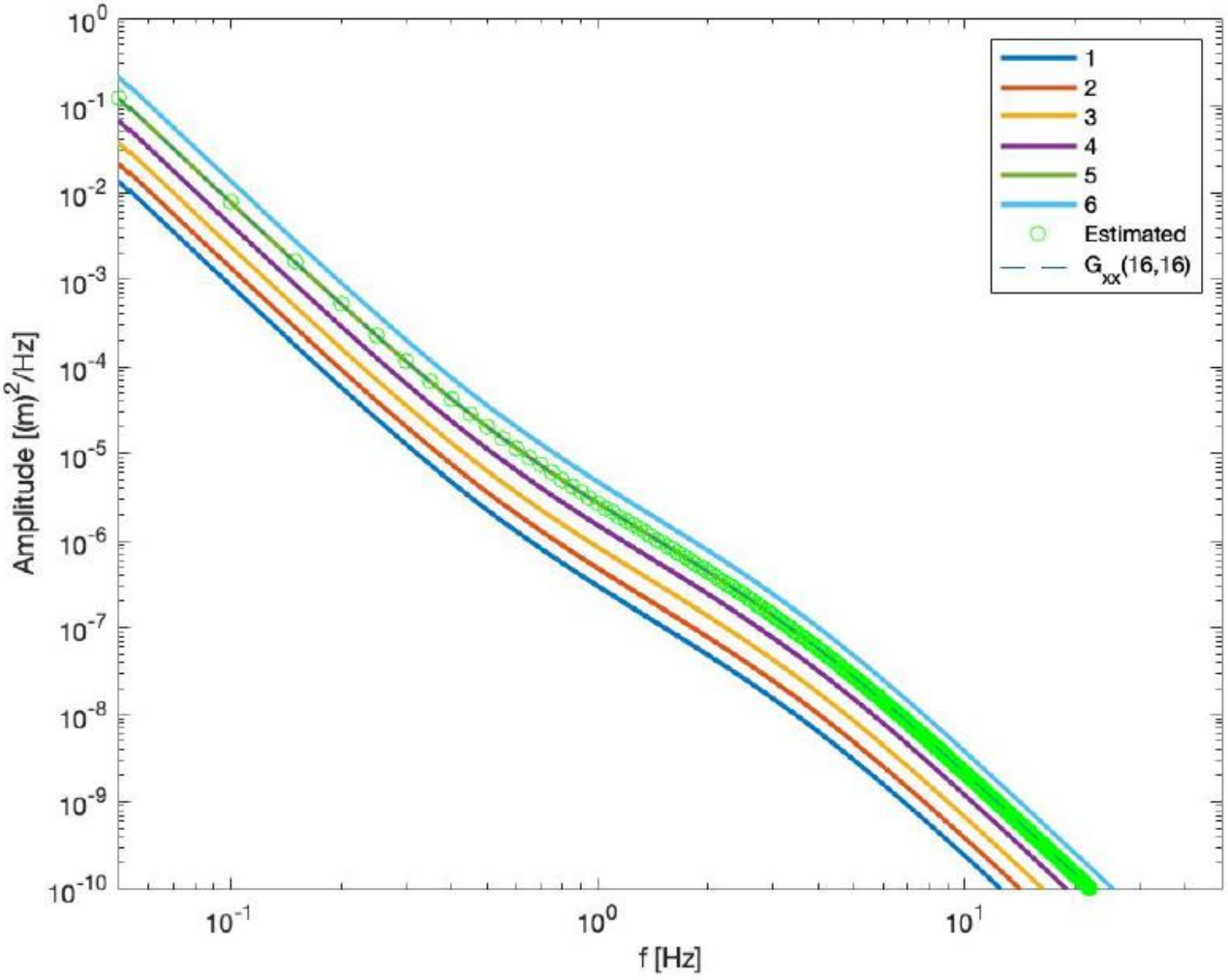

Figure 4.29: Comparison among the theoretical and estimated PSD

5 EXPERIMENTAL RESULTS: MERMEC'S DIAGNOSTIC VEHICLE

The wear of the rails is a very important issue in the railway sector; in fact, any profile change deeply affects the dynamic characteristics of railway vehicles, their stability and passenger comfort, and, in the worst cases, can cause the vehicle to derail. It is therefore of fundamental importance to periodically carry out measurement campaigns of the railway infrastructure in order to verify its state and integrity. The diagnostic train is a convoy of measurement and vision systems that allows to perform a predictive maintenance strategy over the entire railway line. In this chapter we will show how to identify the rail profile through an appropriate installation layout of accelerometers, reaching out results that are good enough to be considered comparable with respect to the optical ones. MerMec S.p.A. is an Italian company specialized in railway inspection and diagnostics, railway signaling, asset management software, diagnostic and professional services for the railway industry.
First of all, the measurement system used will be described and then the results of the road profile identification, performed through the Gonzalez method [7], will be shown and commented.

5.1 *MEASURING SYSTEM DESCRIPTION AND ACQUISITION PARAMETERS*

The MerMec accelerometers layout mounted on the diagnostic train employs 12 mono-axial accelerometers positioned on the body, bogies and axles as shown in figure 5.1, where the sensors that measure vertical accelerations are marked with z while those that measure transversal accelerations are marked with y. The mono-axial accelerometers are able to measure accelerations along the axis, with a sensitivity range compatible with the stress levels required by the application context [18].
Thus the number of accelerometers is too low to perform a correct OMA-based vehicle identification, we took advantage only of the six accelerometers mounted on the axle boxes for most of the further evaluations.

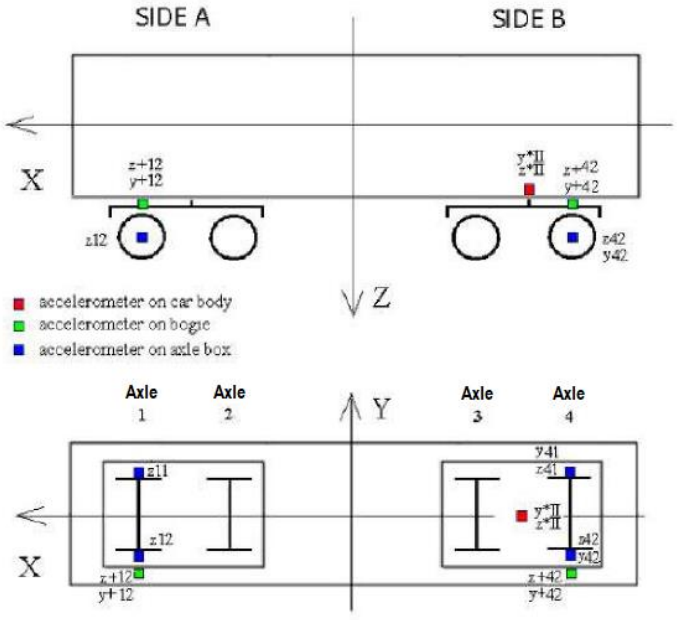

Figure 5.1: MerMec diagnostic vehicle's accelerometers layout

The system outputs consist in various data, acquired with a sampling frequency of 2.5 [kHz]. Those used for the analysis are the following:

- railway line travelled with indication of the kilometer of the line;
- longitude, latitude, and altitude of the vehicle position for each acquisition;
- vehicle forward speed;
- time of each acquisition;
- accelerometric output signal in Volt [V] and in m/s^2.

The data have been processed and will be reported below, those concerning six runs, three in one direction of travel and three in the opposite direction of the same section of the railway line.

5.2 *MEASURING SYSTEM DESCRIPTION AND ACQUISITION PARAMETERS*

The first step was to find a way to extract location information and visualize the path of the diagnostic train. For this purpose, the MATLAB *mapping toolbox* was used to process longitude, latitude, and altitude data. Furthermore, for each of the runs, it is possible to achieve the history over time in terms of speed and output signal. As for the first run, the GPS and historical data are shown in figure 5.2. In the map of figure 5.2a there is an indication of the speed, with the latter increasing in the passage from cold to warm colours of the route.

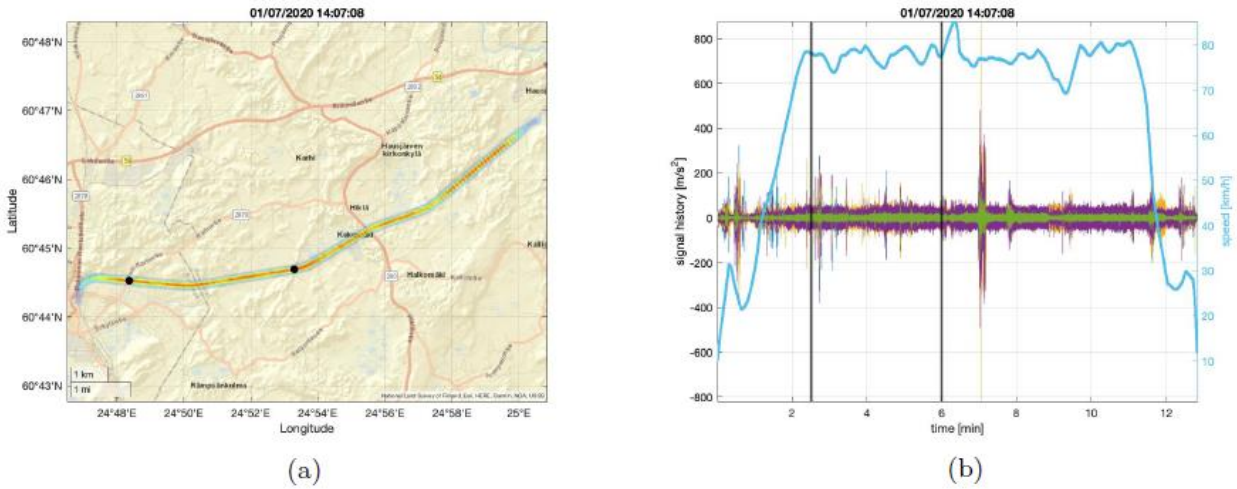

Figure 5.2: Run 1 – GPS data (a) and historic acceleration and speed signals (b)

Both images also show the intervals (marked with black dots in 5.2a and lines in 5.2b) in which the estimates of the PSDs discussed in section 5.3 were obtained. As far as possible, we tried to consider intervals in which the speed results constant as much as possible.
Below there are the GPS data and the histories for the other runs, which are distinguished by the indication of the date and time of the start of the acquisition.

All (b) images from Figure 5.2 to Figure 5.7 show the axle box accelerations (ABA) measured during several runs. It is evident that the accelerometers represented by the green curve shows gain problems during the acquisition. This topic will be properly dealt and discussed in §5.5, according to the railway standard EN 13848-2 [19].

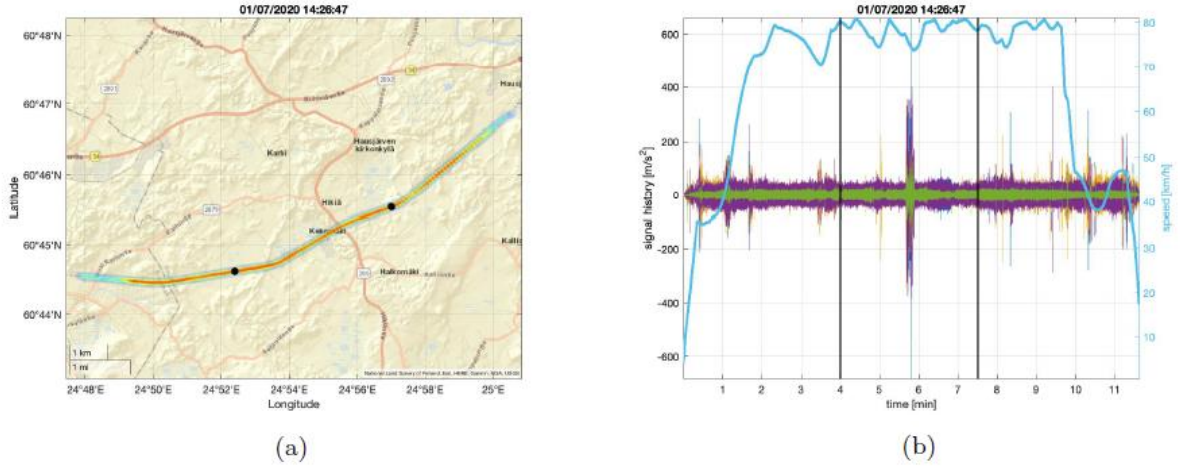

(a) (b)

Figure 5.3: Run 2 – GPS data (a) and historic acceleration and speed signals (b)

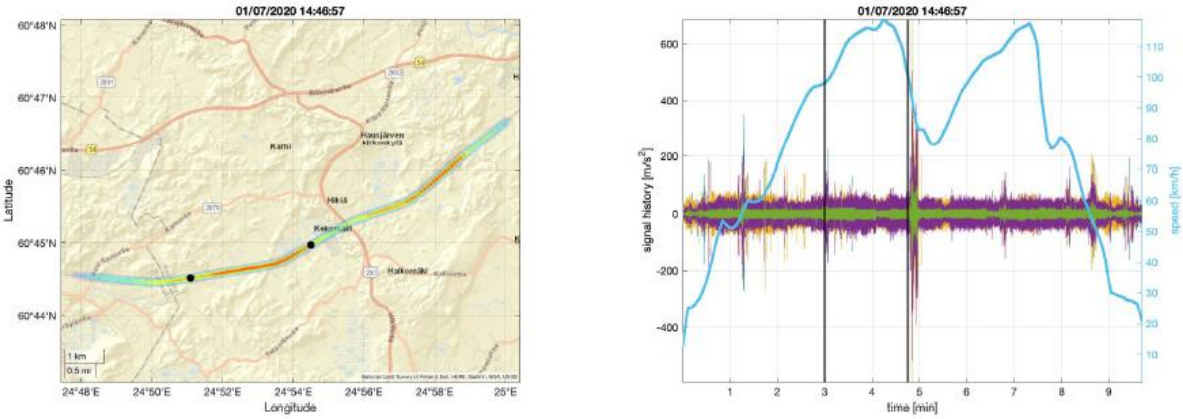

(a) (b)

Figure 5.4: Run 3 – GPS data (a) and historic acceleration and speed signals (b)

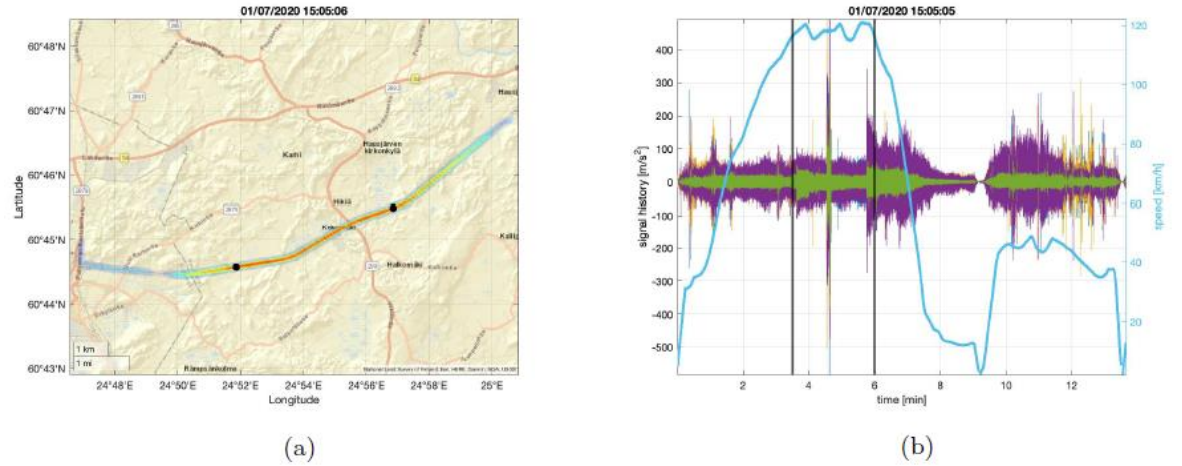

(a) (b)

Figure 5.5: Run 4 – GPS data (a) and historic acceleration and speed signals (b)

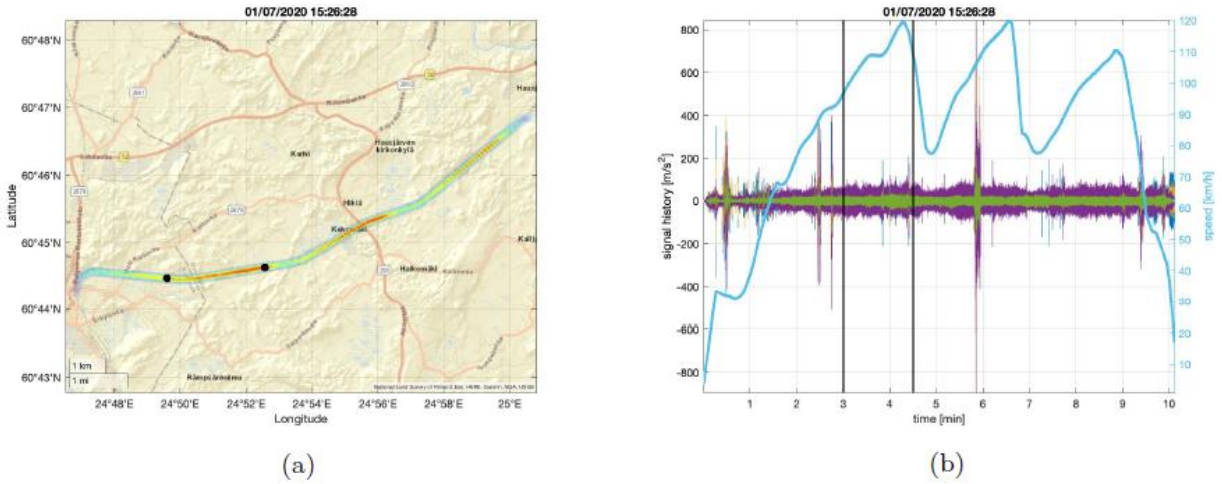

Figure 5.6: Run 5 – GPS data (a) and historic acceleration and speed signals (b)

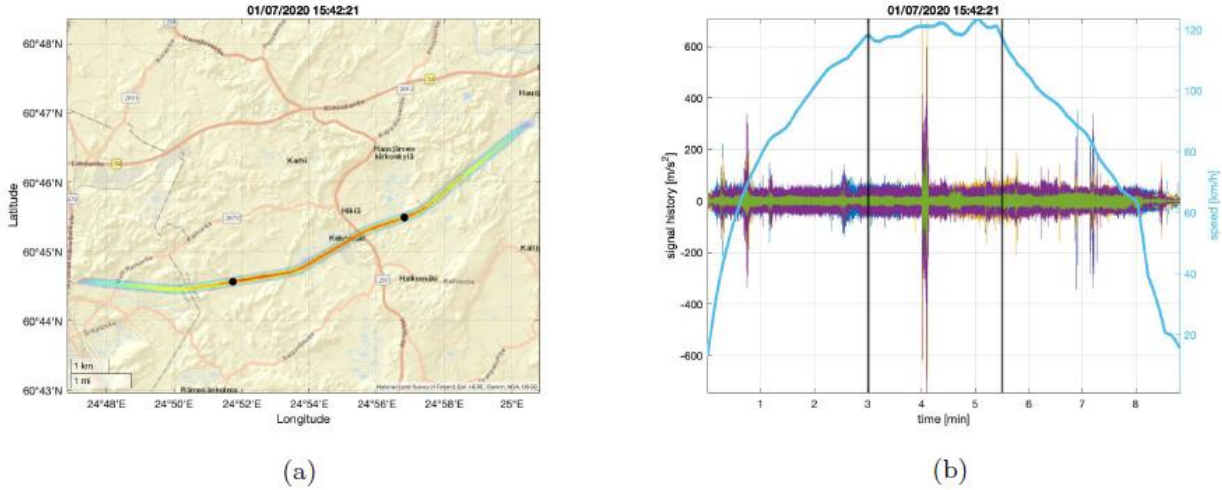

Figure 5.7: Run 6 – GPS data (a) and historic acceleration and speed signals (b)

From the histories it is possible to note how the speed trend (and consequently also the accelerometric output signals) is highly diversified between the different runs. If on one hand this allowed a wider analysis considering different situations and driving conditions, on the other hand this could affect the comparability between the analyses carried out for the different runs.

5.3 *PSD ESTIMATE*

The estimate of the PSDs for the different runs was carried out by using the Welch periodogram method and the correlogram method through which it is also possible to estimate the half-spectrum. The following are the estimates of some elements of the PSD matrix, with reference to the accelerometric sensors indicated in figure 5.1. In particular, the estimates referring to the signals measured by the accelerometers of the body (5.8), of the rear bogie (5.9) and of one of the wheels of axle 4 (5.10) are shown. The graphs show the modulus, phase, and unwrap of the phase for each estimate.

It is possible to notice how the half spectrum estimation provides cleaner and less noisy curves than those obtained through Welch's modified periodogram, by virtue of what has already been

said in subsection 3.2.3. As expected, the highest body peaks occur at low frequencies; for bogies they move to higher frequencies; finally for the wheels with frequency bands up to 500/600 Hz. These considerations derive from involved masses and stiffnesses such that the modes of vibration of the body, bogies and axles affect higher frequencies as one moves to elements with lower masses and higher stiffnesses.
To properly figure out the location of all mentioned accelerometers (e.g., Z*II, Y+42, Z42), please rely on the vehicle's accelerometers layout shown in Figure 5.1.

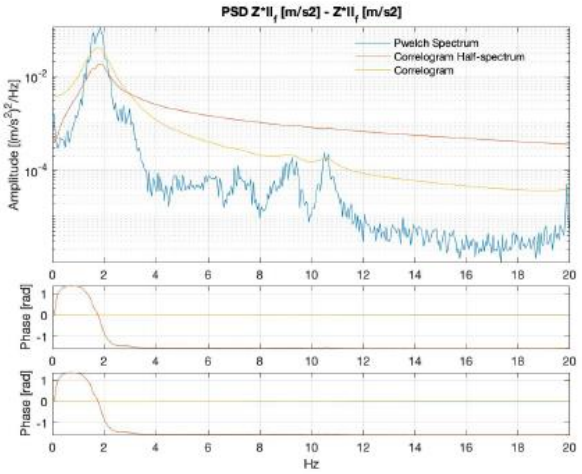

(a) $Z*II$ $autoPSD$

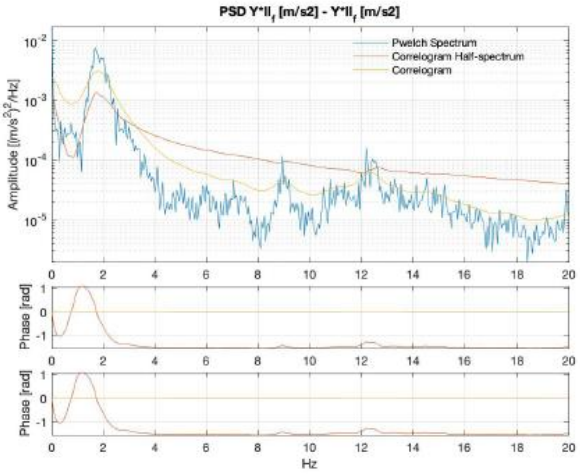

(b) $Y*II$ $auto$ PSD

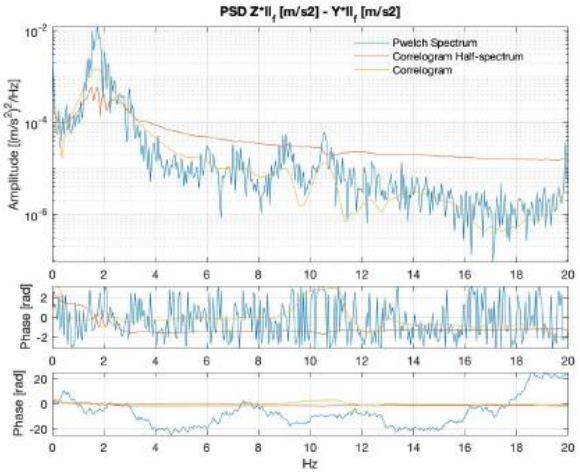

(c) $Z*II \cdot Y*II$ $cross$ PSD

Figure 5.8: Body's PSDs estimate

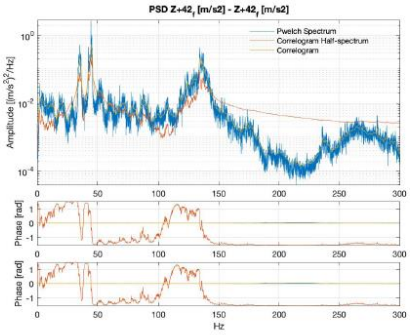

(a) $Z + 42$ *autoPSD*

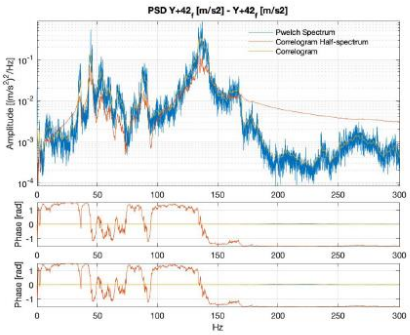

(b) $Y + 42$ *auto PSD*

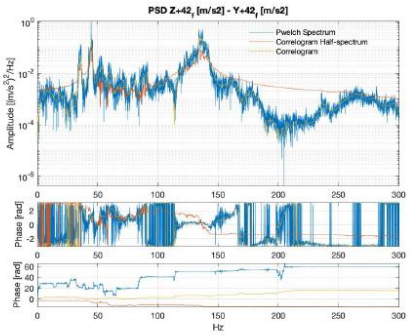

(c) $Z + 42 \cdot Y + 42$ *cross PSD*

Figure 5.9: Bogie's PSDs estimate

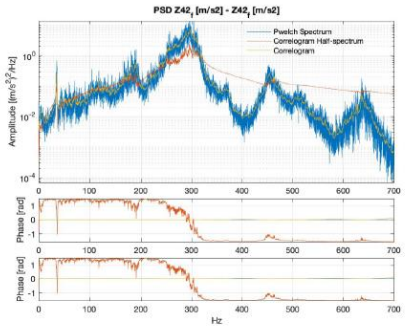

(a) $Z42$ *autoPSD*

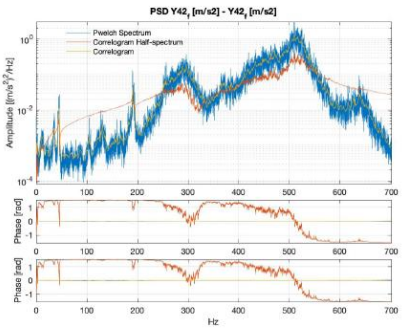

(b) $Y42$ *auto PSD*

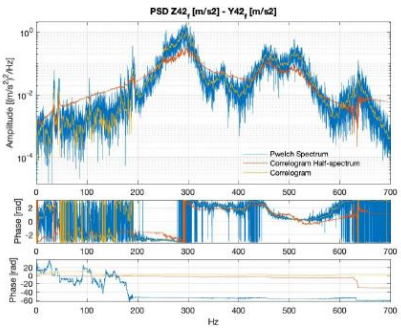

(c) *cross PSD* $Z42 \cdot Y42$

Figure 5.10: Wheel's PSDs estimate

5.3.1 NON-PARAMETRIC ESTIMATE OF TIME DELAYS

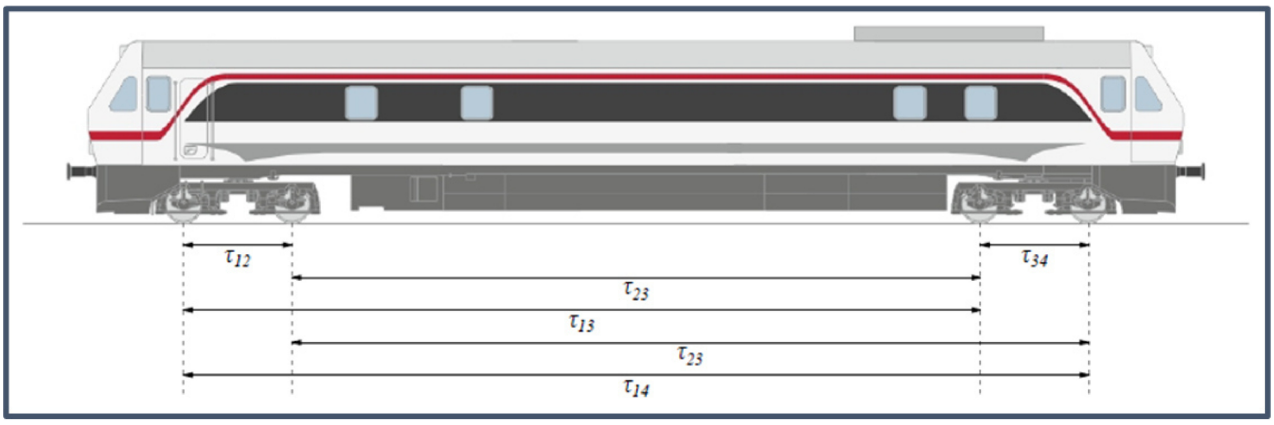

Figure 5.11: Railway vehicle's time delays

As seen in subsection 2.1.7, in the case of two white noises, one out of phase by a time τ with respect to the other, the trend of the cross-PSD phase of the two time-correlated signals is represented by a straight line, whose angular coefficient is precisely the time lag τ. For non-white signals, the trend is very similar or in any case comparable. Therefore, in this study case, taking into consideration the cross-PSD between the output signals of the accelerometers placed on axle 1 and 4 (with reference to figure 5.1 the sensors Z42 and Z12) it is possible to estimate the time lag knowing the angular coefficient of the linear regression line of the phase, on which a phase-unwrapping operation has been carried out. Figure 5.12 shows the estimate of the cross-PSD of sensor signals Z42 and Z12 for run 1. For phase it is possible to notice a sawtooth trend which is the typical trend in the case of time-correlated signals.

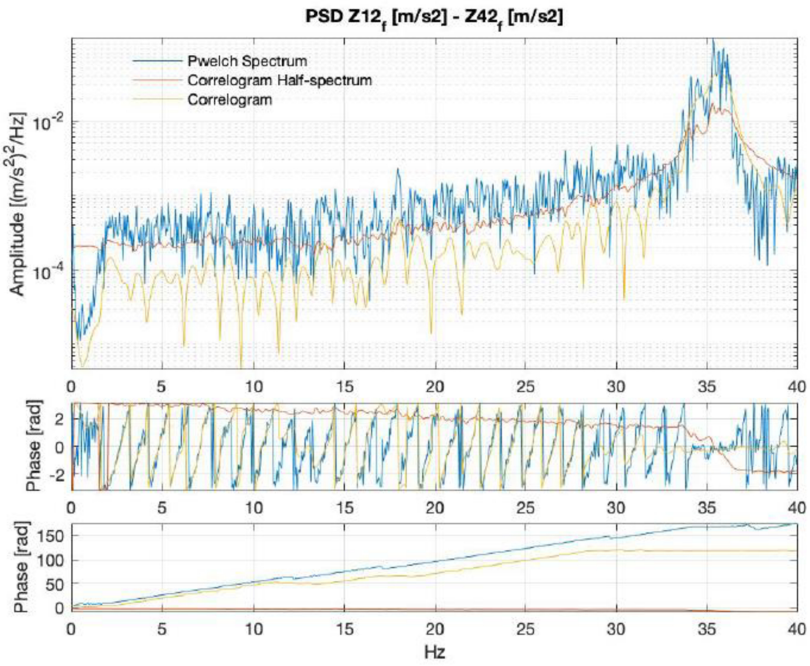

Figure 5.12: Z12 and Z42 cross-PSD estimate

The phase regression line is shown in figure 5.13. To verify this estimate, it is possible to compare it with the phase shift obtained from the ratio between the two axles distance l_{14} and the vehicle speed in the section considered. Since the latter is not constant, the average speed can be considered but a certain margin of error must be taken into account between the two estimates.

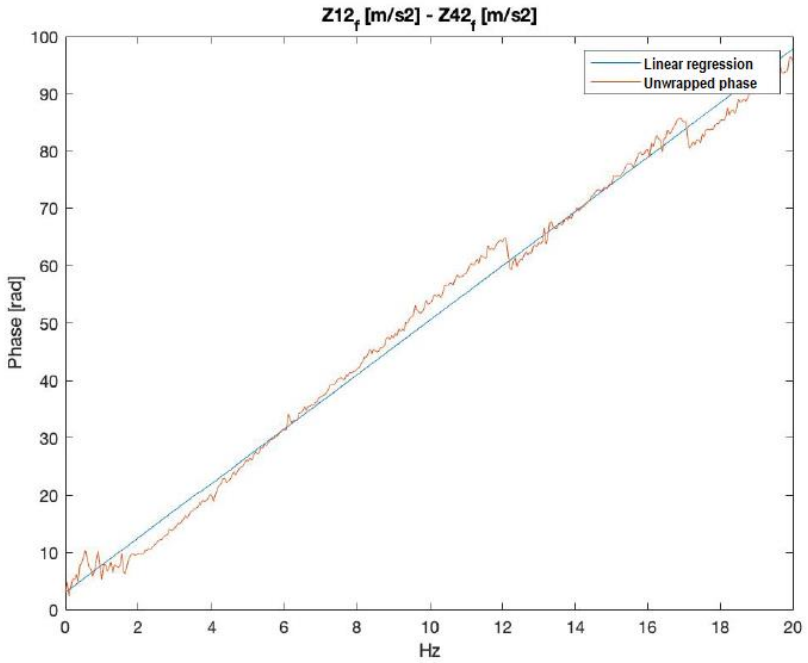

Figure 5.13: Phase linear regression of the Z12 and Z42 cross-PSD

It is interesting to note that from the angular coefficient of the regression line it is also possible to obtain another information: the direction of travel of the train; in fact, if the axle on which the sensor Z12 is present is in advance of the axle of Z42, the angular coefficient (and therefore the phase shift) will be positive. In case of opposite direction of travel, sensor Z42 will be ahead of Z12 and the angular coefficient (and therefore the phase shift) will have the opposite sign.

5.3.2 NON-PARAMETRIC ESTIMATE OF COHERENCE

As we saw for the phase shift between axles, it is possible to exploit the definition of coherence between roughness profiles of (2.68) to estimate it from the measured data:

$$\Gamma(f) = \frac{|G_{LR}(f)|}{\sqrt{G_{LL}(f) \cdot G_{RR}(f)}} \tag{5.1}$$

When dealing with vehicles and interactions with the rolling profile, the auto-PSD of the signals coming out of the wheels are approximable to the PSD of the profile himself. This behaviour is much more noticeable when studying the case of railway vehicles, since the stiffness value of the wheels of such vehicles is much higher than, for example, that of automobiles. This implies an almost unitary transmissibility at low frequencies, and consequently a high similarity between the input and output PSDs. This aspect has already been highlighted in chapter 4, when the theoretical PSD of the track was compared with the estimates made and with the auto-PSD of the wheels. At

low frequencies, the curves are almost superimposed, while at high frequencies there is a deviation, linked to the modes of vibration that affect the unsuspended masses. Therefore, for the estimation of the coherence in the real case through (5.1) it is possible to use the PSD of the displacements of the output signals of the wheels (in figure 5.14), instead of the input ones of the profile, obtaining in any case some indications on the coherence of the profiles.

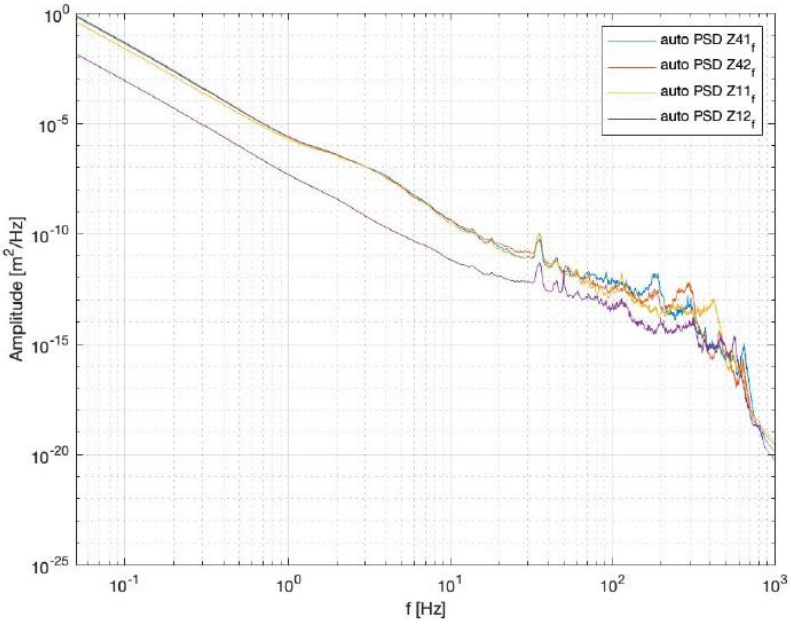

Figure 5.14: Wheels' Auto-PSD

Figure 5.15 shows an average of the auto-PSD signals (without the one related to Z12) output from the sensors on the wheels, compared with the classification according to FRA.

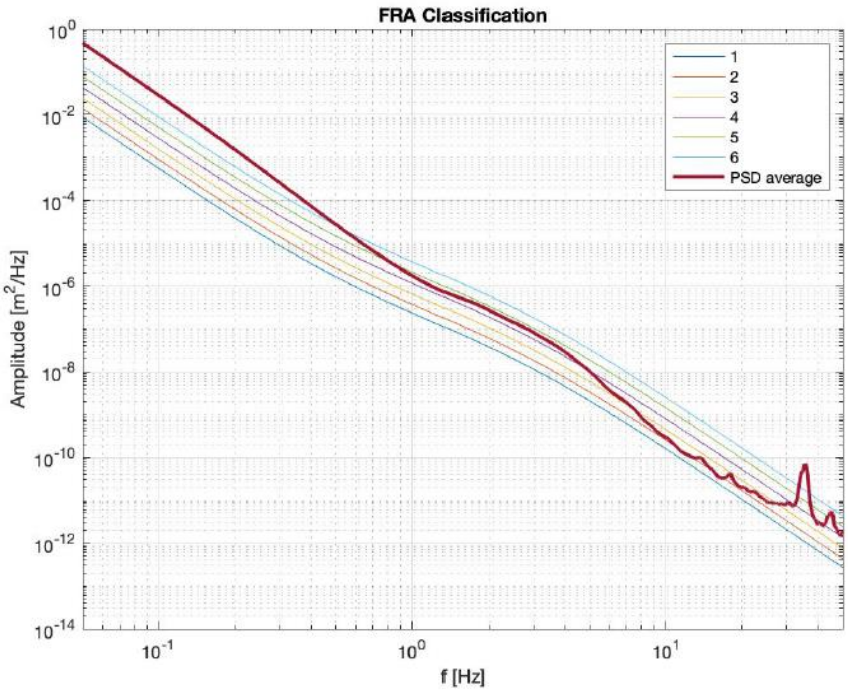

Figure 5.15: Averaged Wheels' Auto-PSD compared with the FRA profiles

Figure 5.16 shows the trends of the coherence between the PSDs of the displacements measured by accelerometers placed on opposite wheels.

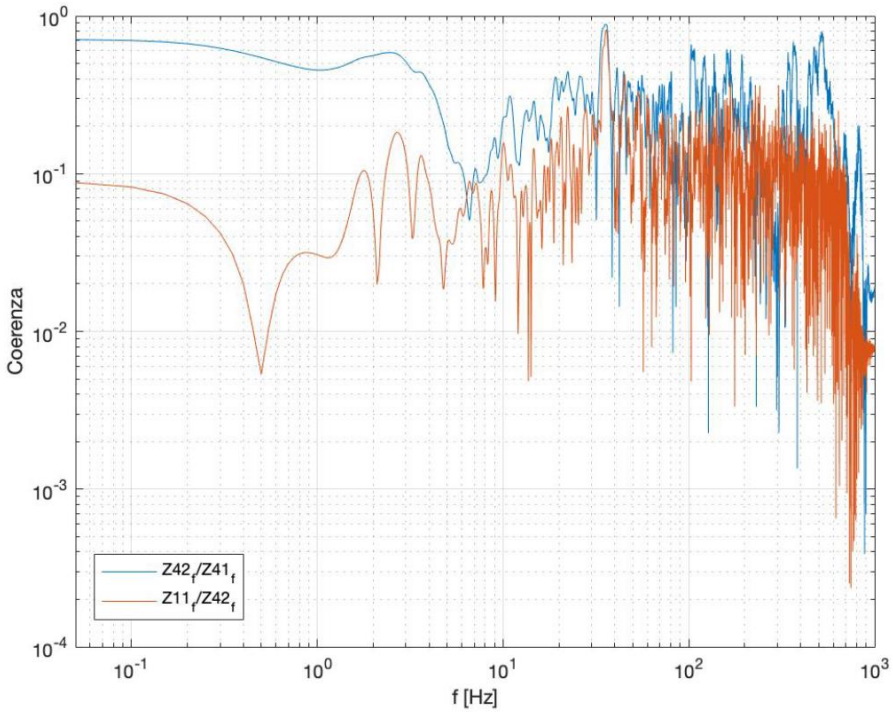

Figure 5.16: Real profiles' coherence estimate

From the comparison with the coherence estimated through (5.1) in the theoretical case of the 17 dof model of figure 5.17, we can see a very similar trend at the lowest frequencies and an equivalent behaviour in the higher frequency band. The figure also shows the Bogsjö curve obtained through (2.69). Note how the curves are superimposable below the frequency of 1 Hz.

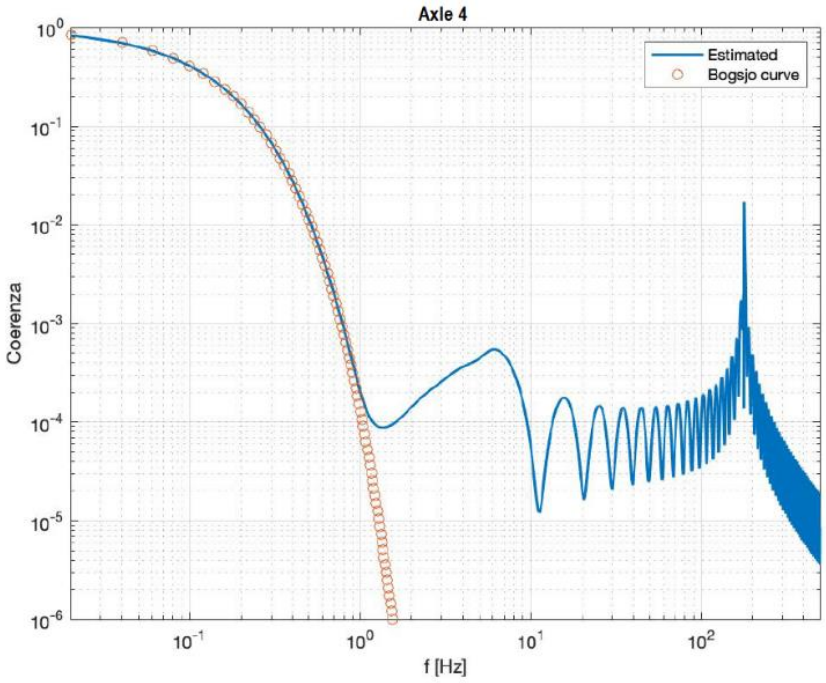

Figure 5.17: Real profiles' coherence estimate

5.4 *INVERSE PROBLEM RESOLUTION THROUGH THE GONZALEZ METHOD*

We now proceed to apply Gonzalez's method to the data of the real case. Compared to the algorithm of figure 2.32 used for the theoretical models, there are some differences, since the output signals are already available and it is not necessary to estimate them either in the calibration phase or in the extraction phase. Figure 5.18 shows the pipeline. Approximate profiles according to FRA will be used for calibration.

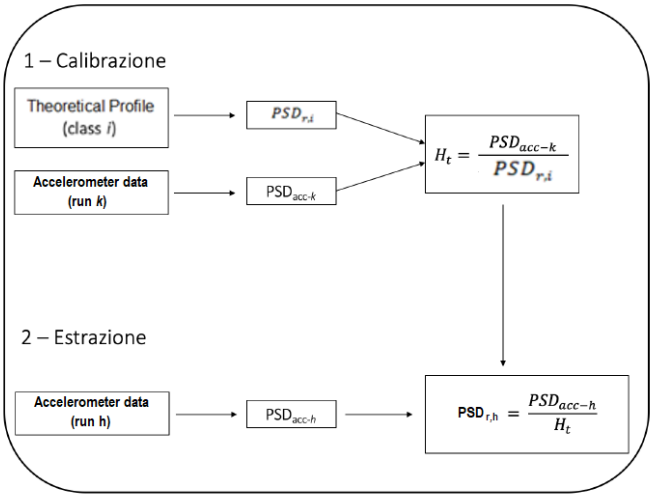

Figure 5.18: Application scheme of the Gonzalez method

5.4.1 CASE 1

In the first case, run 1 is taken into consideration for calibration and run 2 for verification. Figure 5.19 compares the GPS data and the histories of speed and signal of the two runs.
The choice of the profile's class used for the calibration fell on class 5. Figure 5.20 shows the comparison between the average of the PSD of the displacements on the wheels during run 1 and the PSD of the class 5 according to FRA.
For the estimation of PSD, both in calibration and in extraction, the correlogram method on the whole spectrum and the one on the half-spectrum were used. Figure 5.21 shows the comparison between the element of the matrix $\boldsymbol{H_t}(f)$ corresponding to the auto-PSD of the sensor signal $Z11_f$ estimated with both modes.
Regarding the rail profile estimated in the case of the correlogram, figure 5.22a shows the estimated profile within the FRA classification, while figure 5.22b shows the comparison between the estimated profile and the average of auto-PSD of the wheels' displacements. Figure 5.23, on the other hand, shows the estimate obtained in the case of the correlogram on a half-spectrum.

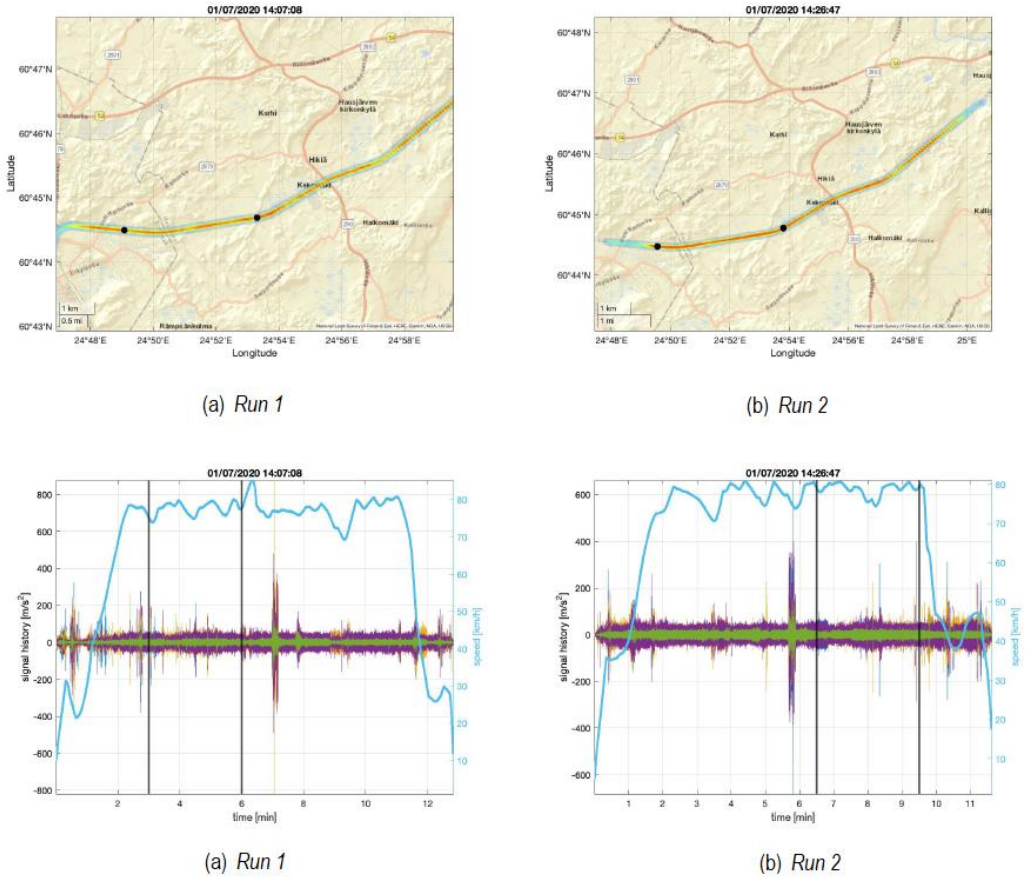

Figure 5.19: Runs' histories comparison

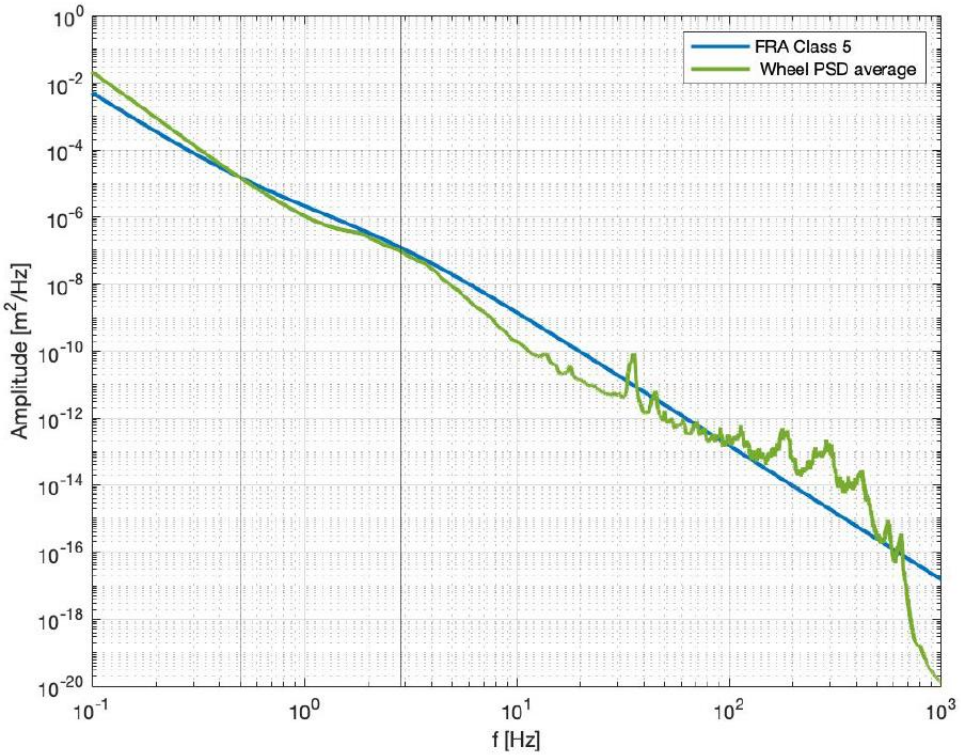

Figure 5.20: Comparison between the average wheels' PSD and the Class 5 FRA profile

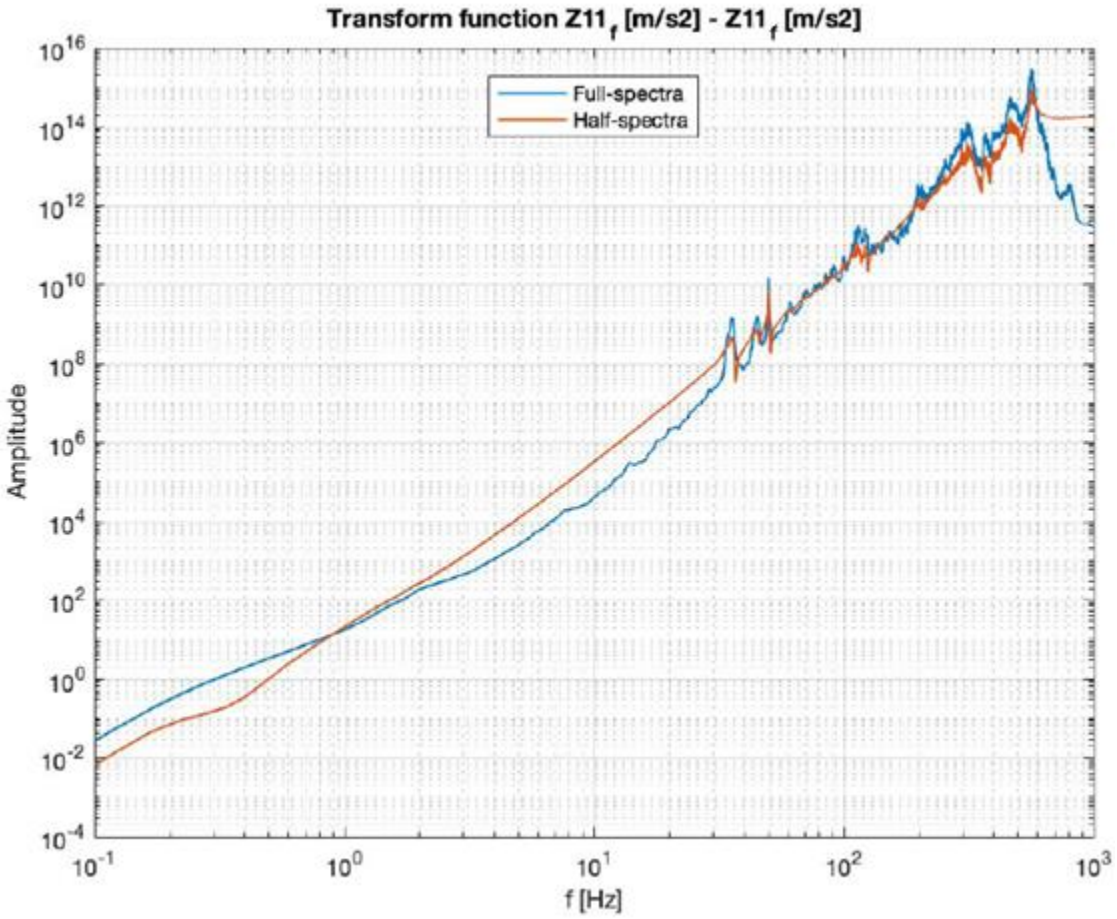

Figure 5.21: Comparison between the same $H_t(f)$ element, estimated through half and full spectra correlogram

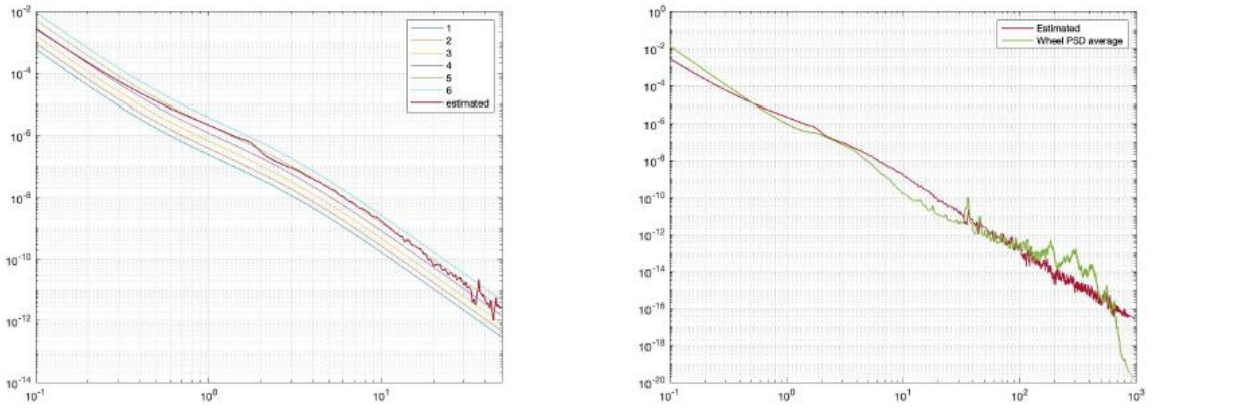

(a) *Estimate and classification*

(b) *Comparison between the estimated profile and the wheels' auto-PSD*

Figure 5.22: Comparison between the average wheels' PSD and the Class 5 FRA profile

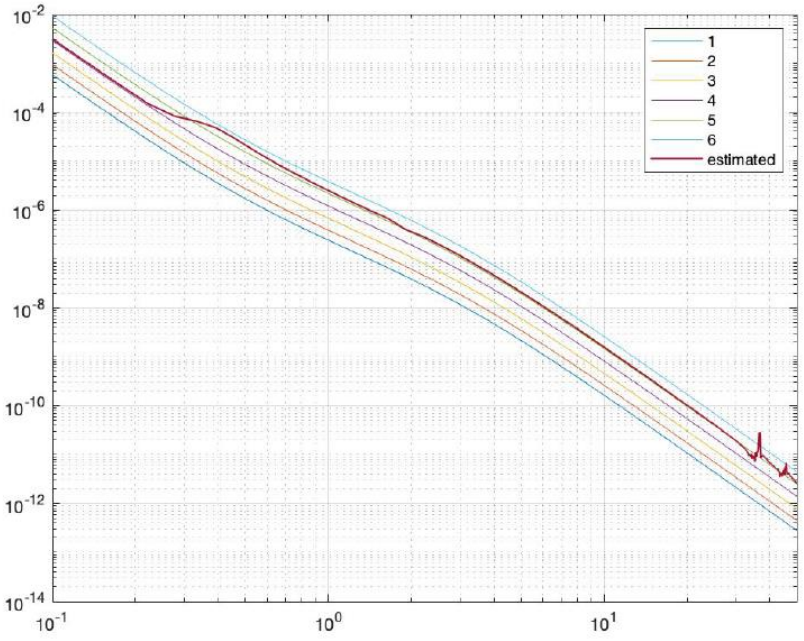

Figure 5.23: Estimate starting from the half-spectrum correlogram's results

Note now how both estimated profiles have a similar trend to the class 5 profile, in particular in the range $1 \div 30\ Hz$.
By exploiting the same transfer function $\boldsymbol{H_t}(f)$ it is possible to proceed with the extraction phase taking into consideration another section of run 1 (figure 5.24).

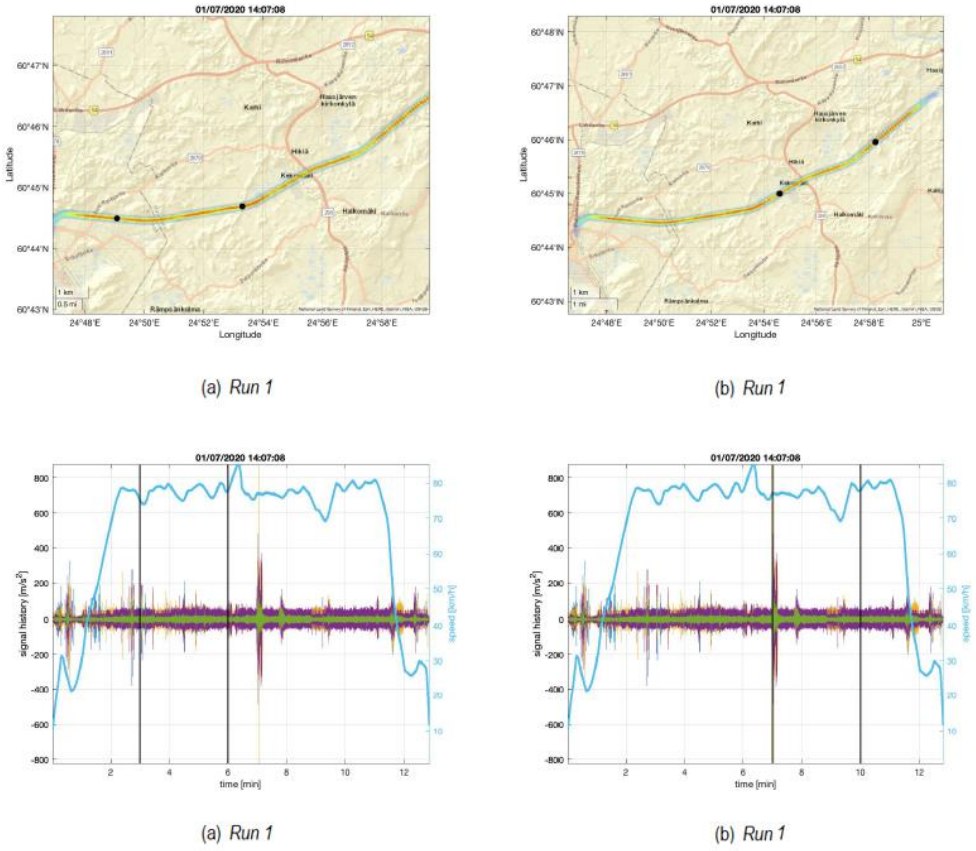

(a) *Run 1* (b) *Run 1*

(a) *Run 1* (b) *Run 1*

Figure 5.24: Runs' histories comparison

The results are reported in figures 5.25 and 5.26. Notice how in this case the estimate has shifted towards a higher class, i.e. class 6.

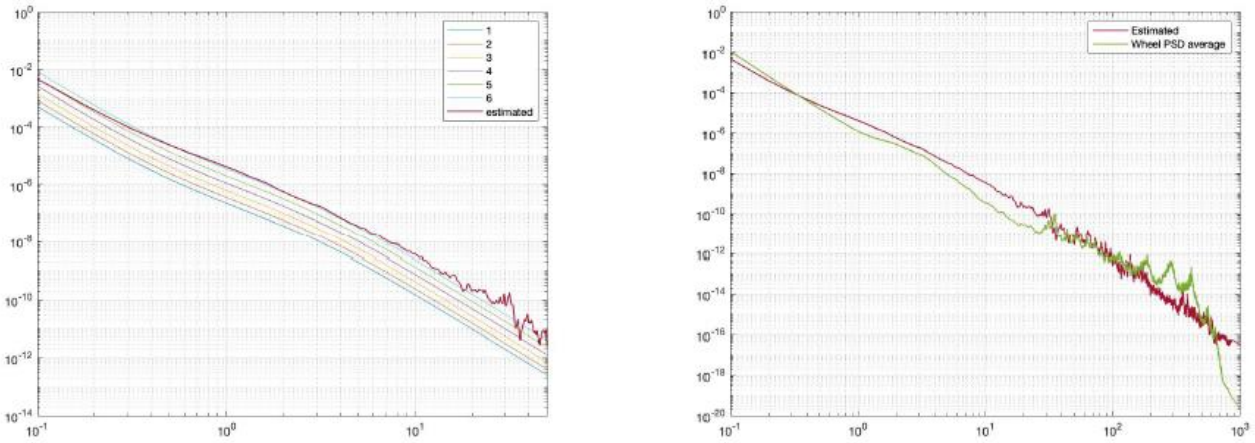

(a) *Estimate and classification*

(b) *Comparison between the estimated profile and the wheels' auto-PSD*

Figure 5.25: Correlogram estimate

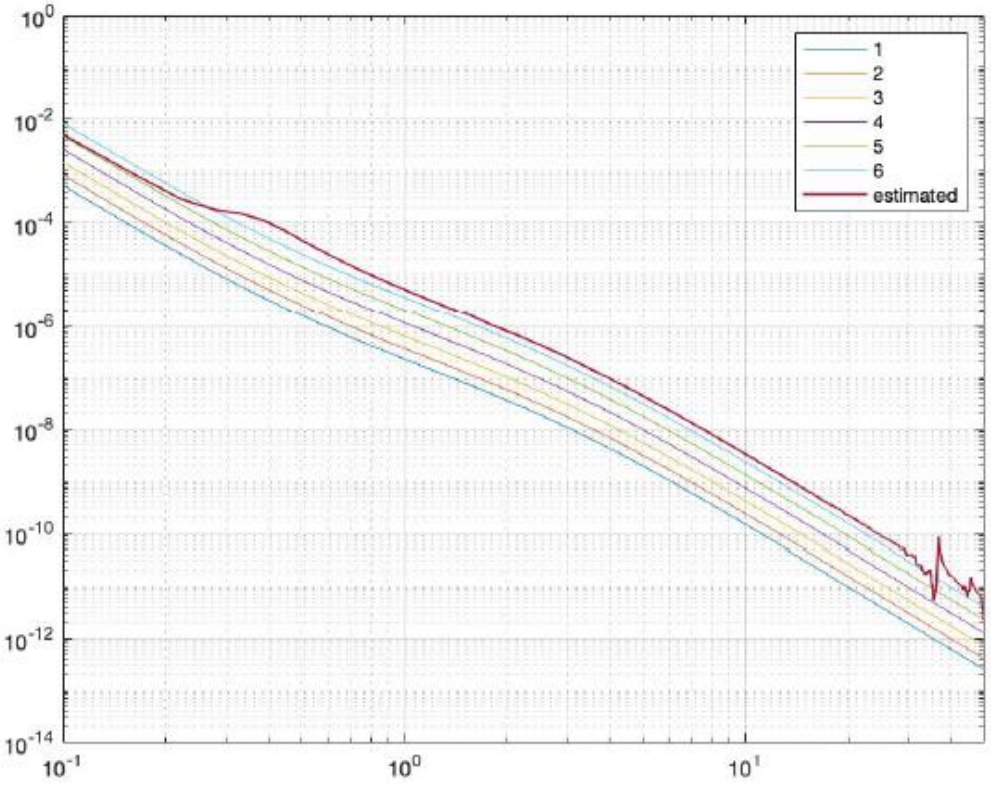

Figure 5.26: Estimate starting from the half-spectrum correlogram's results

5.4.2 CASE 2

Now we want to verify the goodness of the results considering the same railway section traveled with different speed, using run 2 for calibration and run 4 for verification. Figure 5.19 compares the GPS data and the histories of speed and signal of the two runs. Note how, since the speeds between the two sections are very different, in order to maintain an equal observation time, the two considered sections have different lengths.
In particular, in run 2 the average speed is about 77 km/h while in run 4 it is about 117 km/h, therefore in the observation time $t_0 = 180\ s$ the distance traveled by the train in run 4 is greater than in run 2.

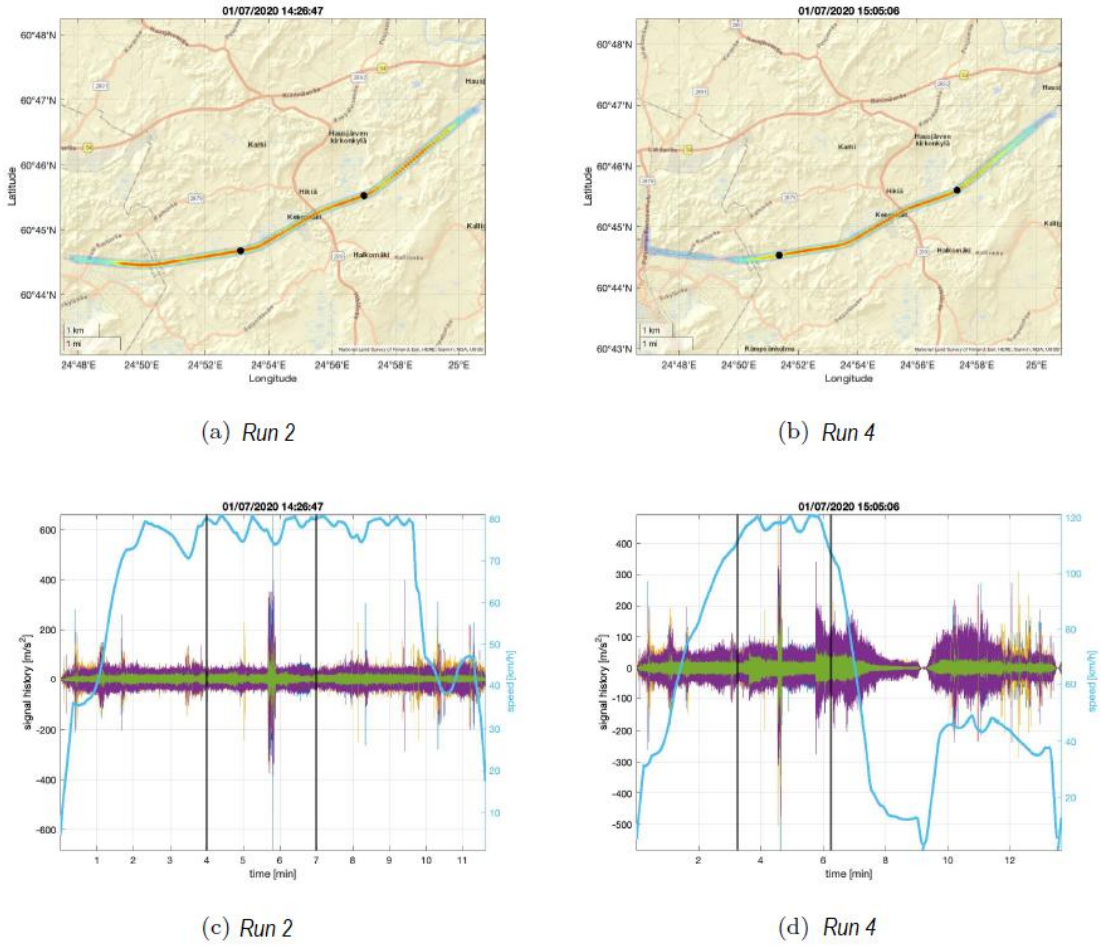

(a) *Run 2* (b) *Run 4*

(c) *Run 2* (d) *Run 4*

Figure 5.27: Runs' histories comparison

Also in this case a profile class 5 was chosen for calibration. Figure 5.28 shows the comparison between the element of the matrix $\boldsymbol{H_t}(f)$ corresponding to the auto-PSD of the sensor signal $Z11_f$ estimated with the full-spectrum and half-spectrum correlogram method.
Regarding the rail profile estimate in the case of the correlogram, figure 5.29a shows the estimated profile within the FRA classification, while figure 5.29b shows the comparison between the estimated profile and the average of the auto-PSD of the wheel's displacements. Figure 5.30 shows the estimate obtained in the case of the correlogram on a half-spectrum.

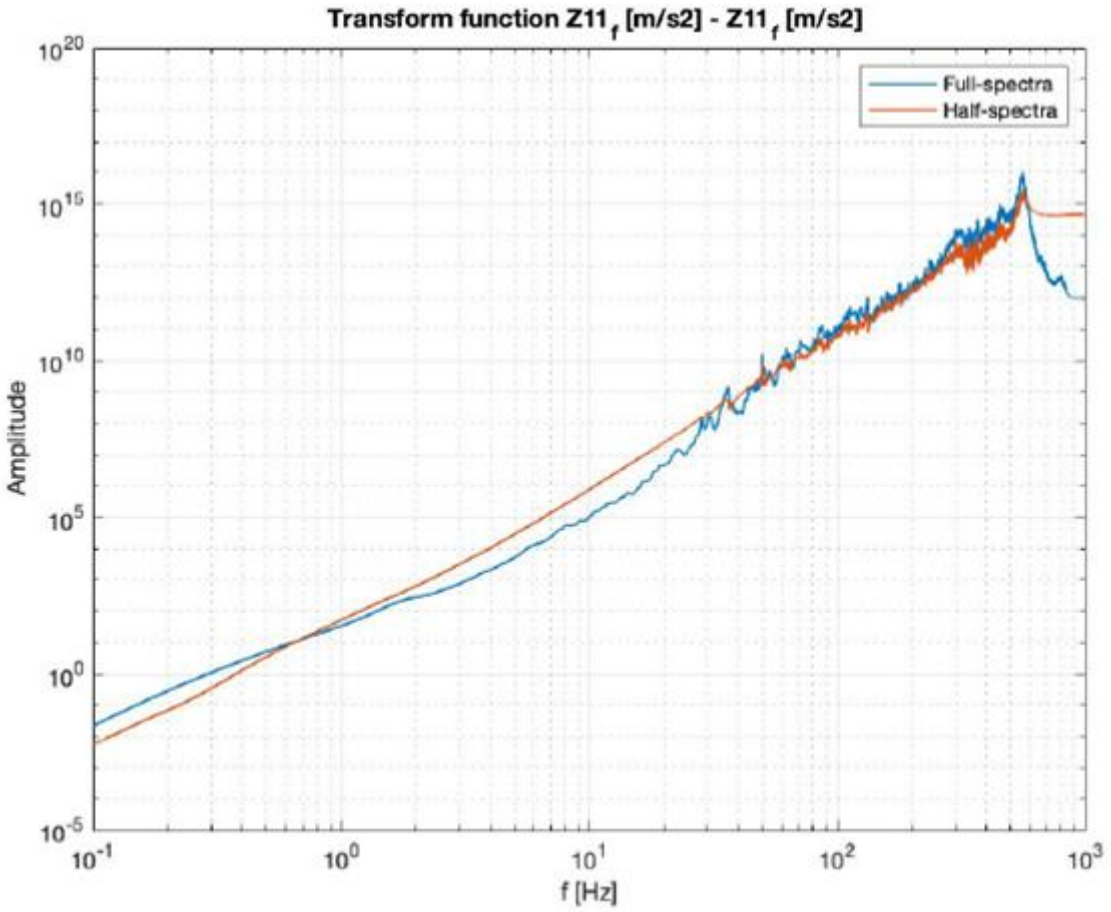

Figure 5.28: Comparison between the same $H_t(f)$ element, estimated through half and full spectra correlogram

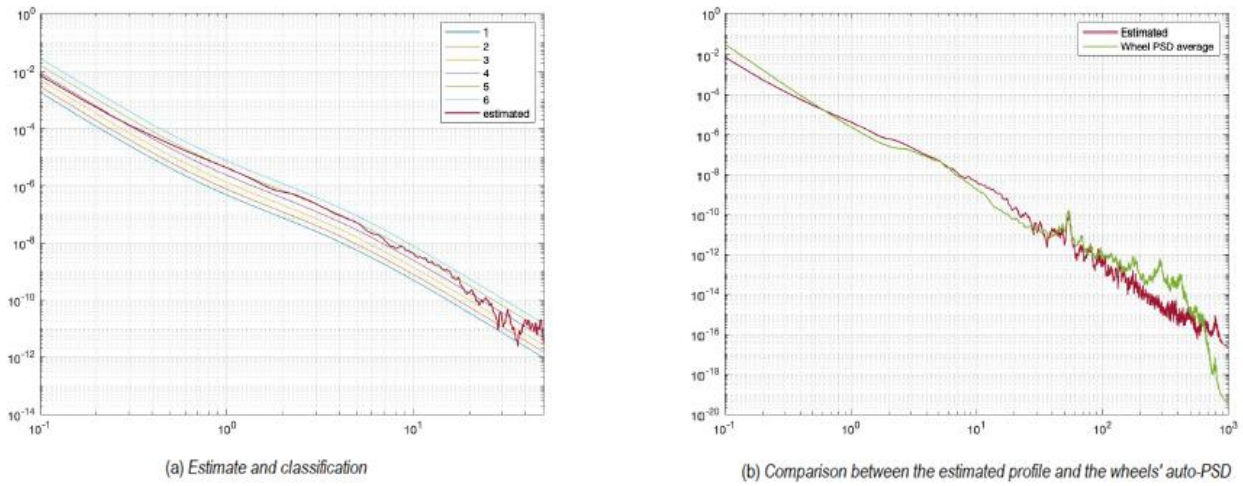

(a) *Estimate and classification*

(b) *Comparison between the estimated profile and the wheels' auto-PSD*

Figure 5.29: Correlogram estimate

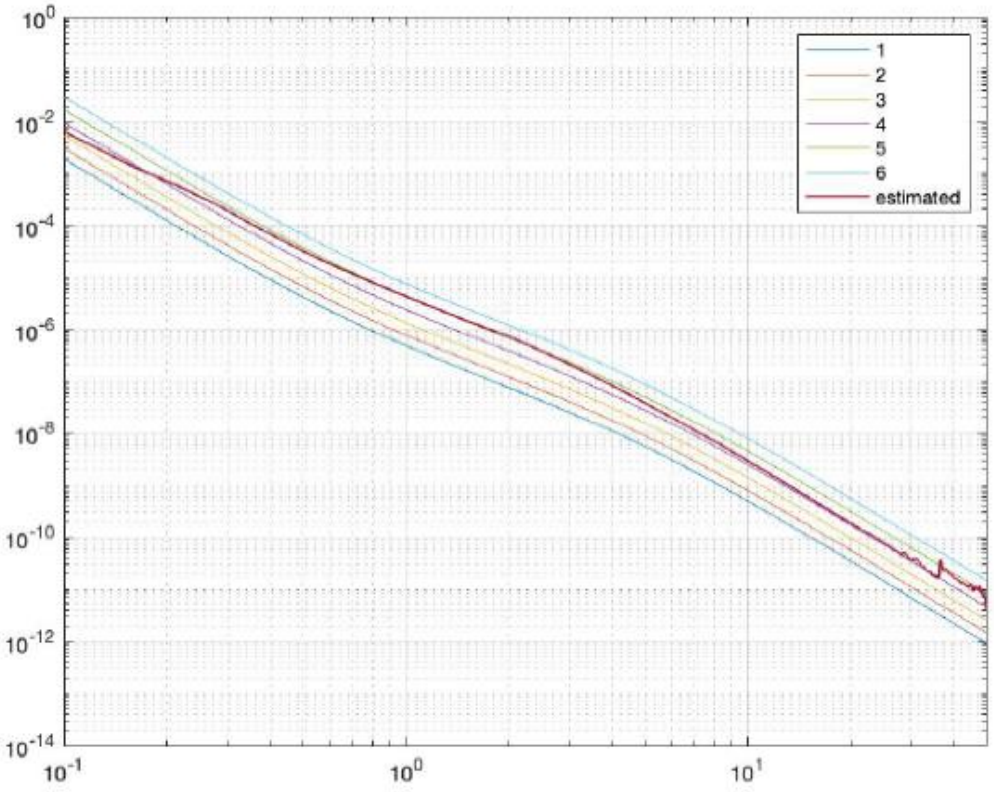

Figure 5.30: Estimate starting from the half-spectrum correlogram's results

In this case too, the estimates obtained are quite similar to class 5 profile but certainly less accurate than the ones obtained in Case 1, where the forwarding speed was the same in each run.

5.5 *PROFILE IDENTIFICATION AND LIVE VALIDATION ACCORDING TO EN 13848*

The profile identification is now investigated according to EN 13848 ([18], [19], and [20]).
Since the vehicle accelerometers layout do not allow to correctly perform the OMA method, we are going to exploit the low frequency similarity between the profiles' and the wheels' displacement PSDs.
Note that the accelerometers mounted on right (or left) wheel of axle 1 and those on right (or left) wheel of axle 4 could be considered as two different and independent sensors that measures the same rail profile. Consequently, it is not strictly necessary to run multiple times on the same track to validate the repeatability of the measuring campaign because this could be performed "live".
This characteristic of the railway's vibration-based condition monitoring is almost unique if compared with the common optical measuring systems, because involving the mounting of multiple optical boxes and/or laser sensors would have a big impact on the overall cost of the installation.

Next figures show the wheels' PSD represented in the spatial frequency and then in wavelength domain, for a run performed at a constant speed.

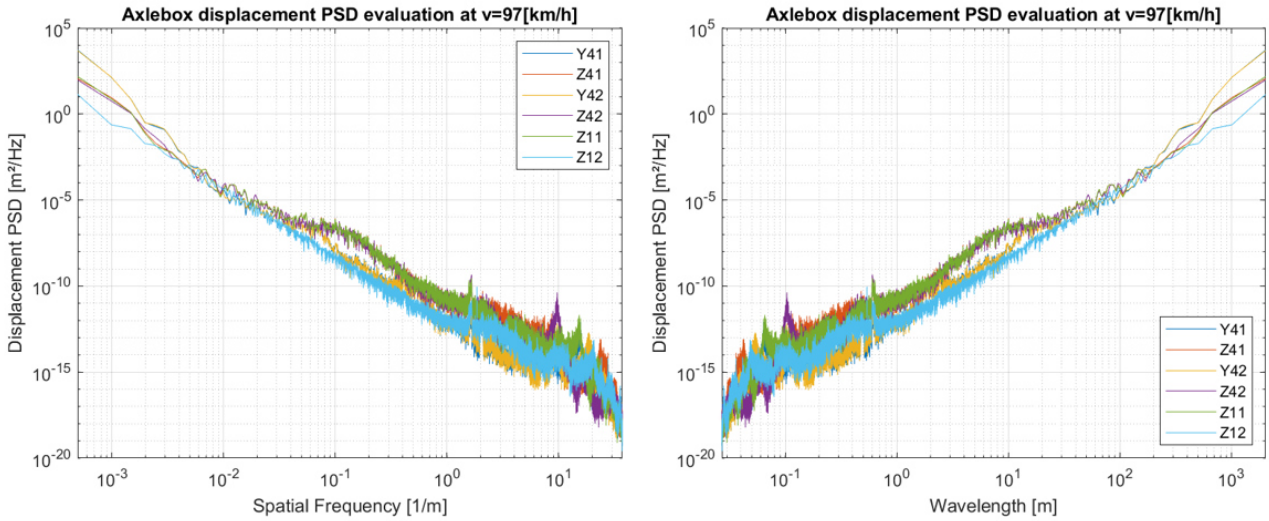

Figure 5.31: Wheels' displacement PSD in spatial frequency and wavelength domain

Next step consists simply in focus the analysis in the wavelength ranges defined in Table 2.3 of section 2.4.3.

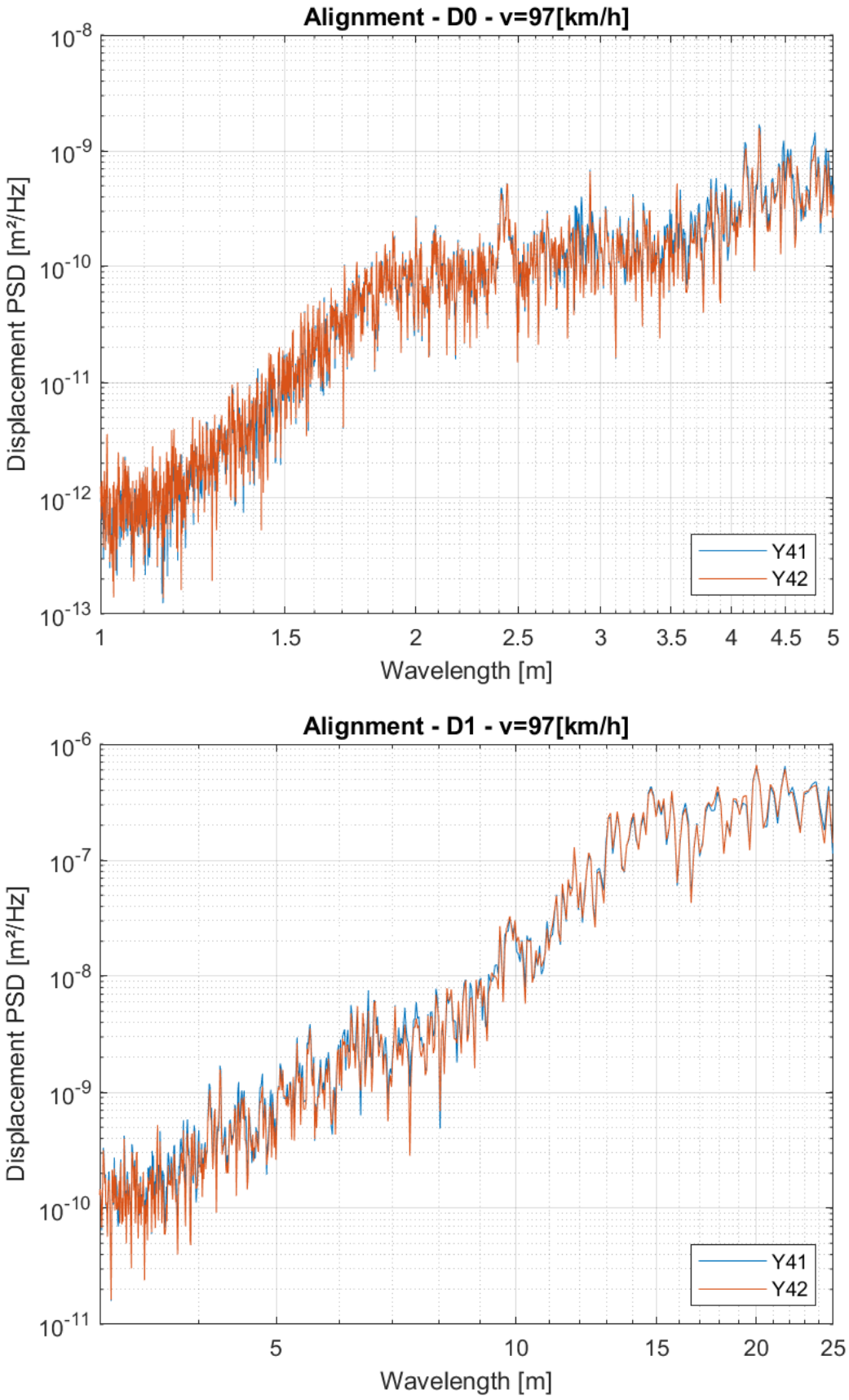

Figure 5.32: Alignment, D0 and D1 category

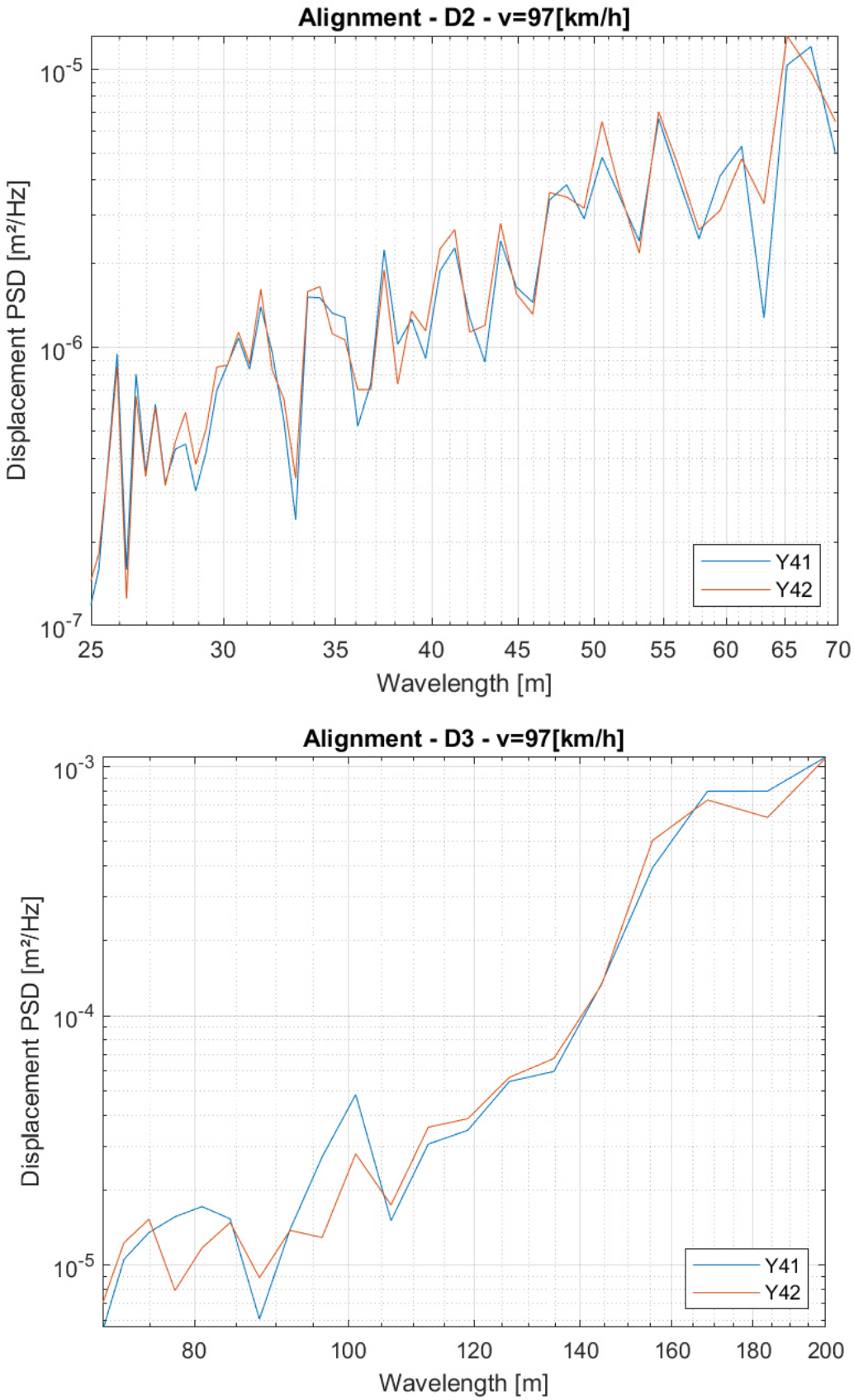

Figure 5.33: Alignment, D2 and D3 category

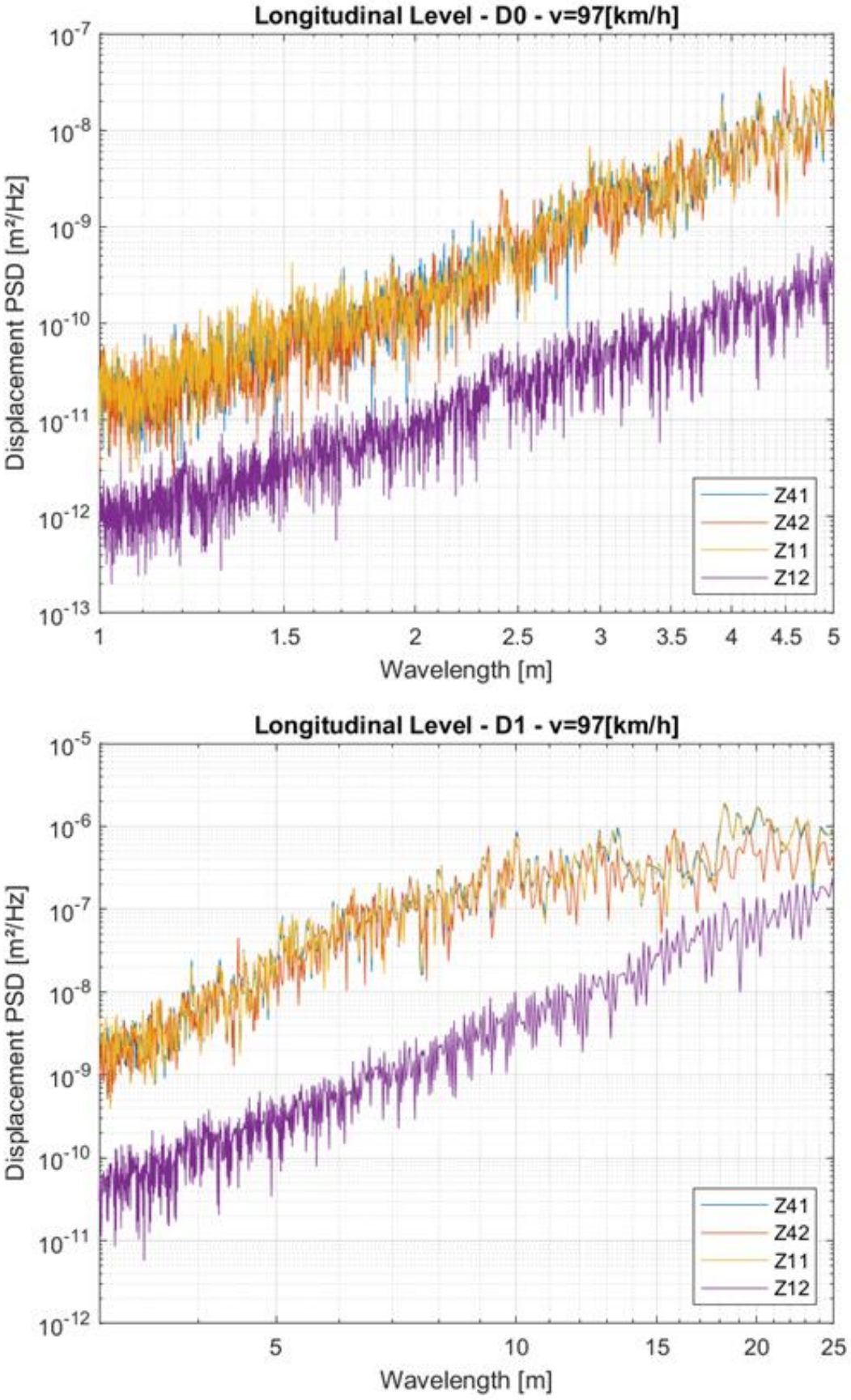

Figure 5.34: Longitudinal Level, D0 and D1 category

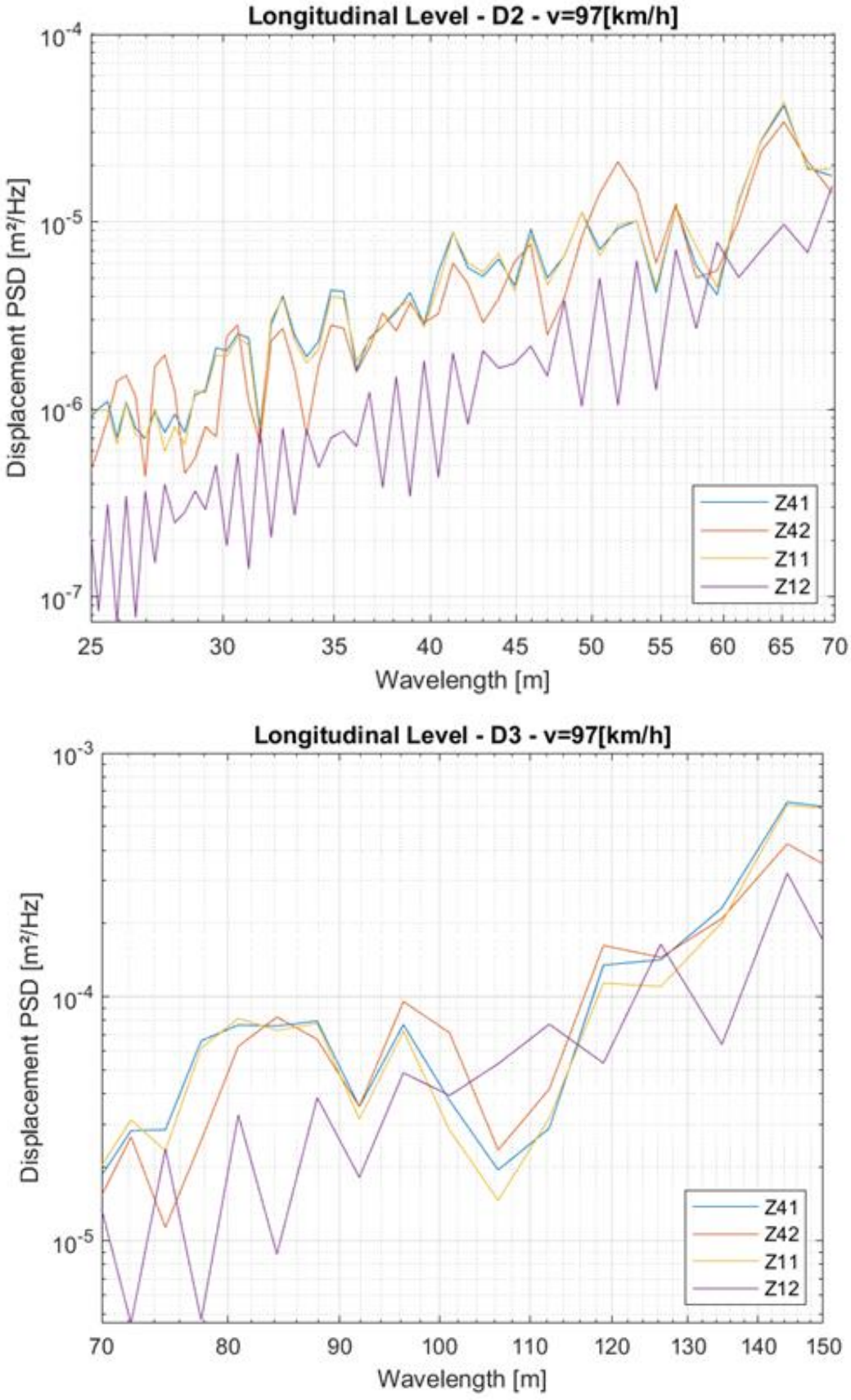

Figure 5.35: Longitudinal Level, D2 and D3 category

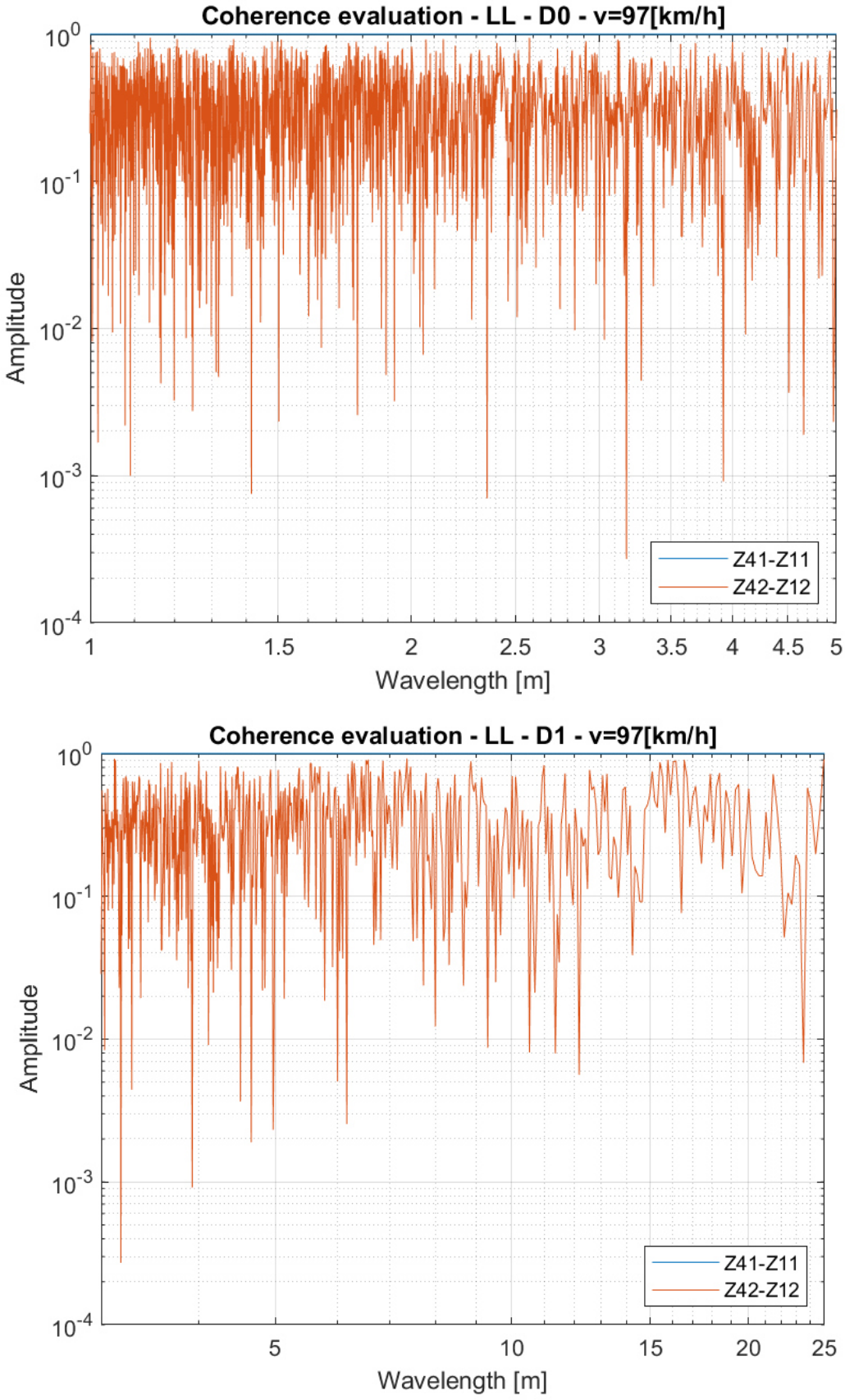

Figure 5.36: Longitudinal Level, D0 and D1 category, Front–Rear Coherence function

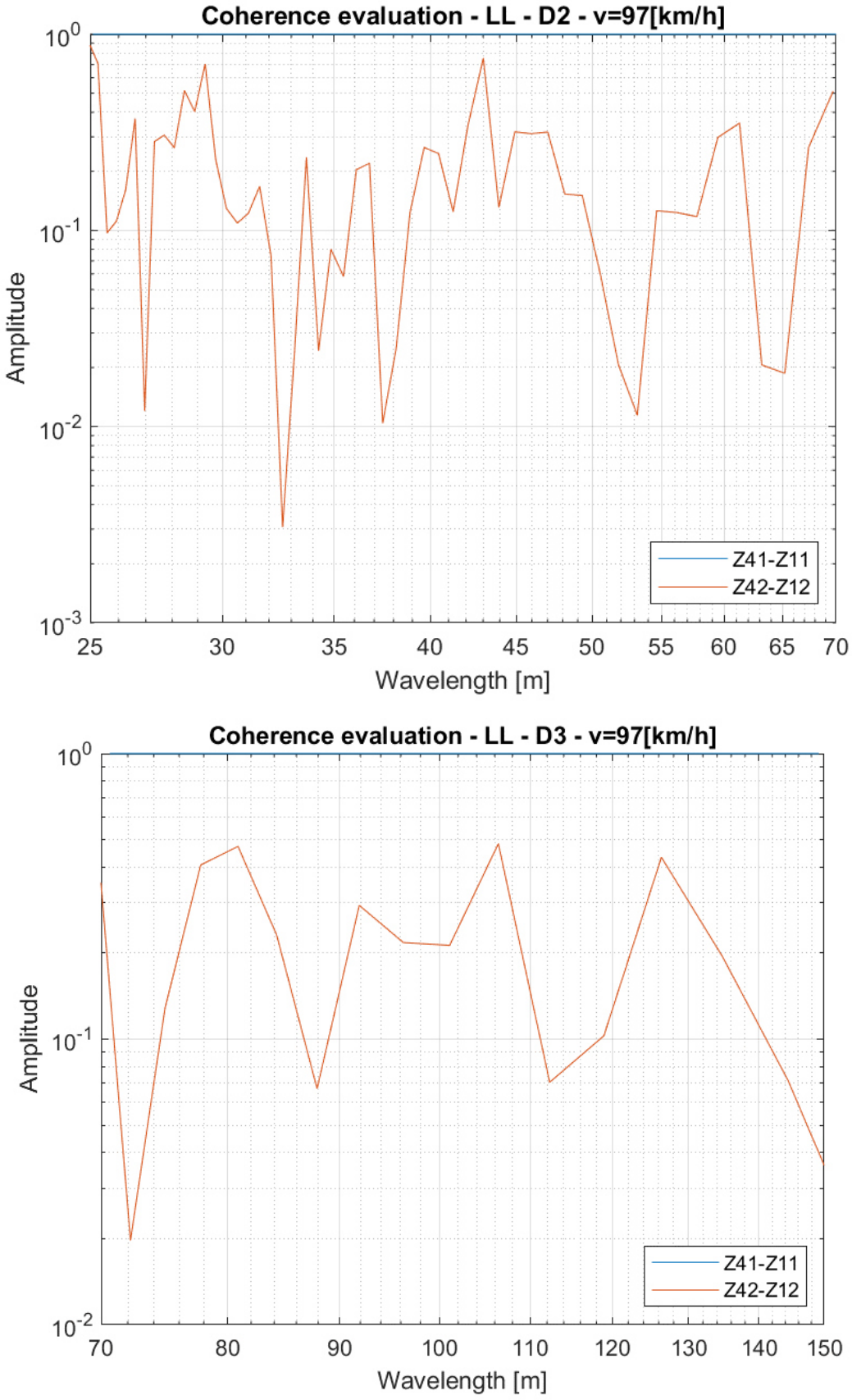

Figure 5.37: : Longitudinal Level, D2 and D3 category, Front–Rear Coherence function

The following table summarizes the RMS value obtained via displacement PSD integration (the valued obtained are all lower than the intervention and alert limits indicated in standard [20]), the transfer function mean value and the coherence mean value for each wavelength range.

	LL – D0	LL – D1	LL – D2	LL – D3
Z41 – RMS [m]	1.67E-04	1.09E-03	2.00E-03	5.52E-03
Z42 – RMS [m]	1.60E-04	9.32E-04	1.94E-03	4.89E-03
Z11 – RMS [m]	1.67E-04	1.08E-03	2.00E-03	5.37E-03
Z12 – RMS [m]	2.51E-05	2.68E-04	1.20E-03	3.76E-03
Coherence Z41 – Z11	1.00E+00	1.00E+00	1.00E+00	1.00E+00
Coherence Z42 – Z12	3.37E-01	3.53E-01	2.21E-01	2.32E-01
Transfer function Z41 – Z11	1.00	1.00	1.00	1.03
Transfer function Z42 – Z12	6.39	3.48	1.62	1.30

Table 5.1: Longitudinal Level measured values

The transfer function and the coherence evaluated for the couple Z41-Z11 have a value near to 1 for all ranges, so the estimation have been validated.
Unfortunately, the Z42-Z12 values are far from being acceptable but this is attributable to a misfunction of sensor Z12. Its measured values are very different with respect to the other three and this is fair also just looking at the PSDs' wavelength trends in Figure 5.34 and Figure 5.35.

Unfortunately, for the alignment it has not been possible to perform the “live” validation of data because the actual vehicle’s accelerometers layout counts only two Y sensors on the wheels, both on the same axis and so measuring different profiles (right and left ones).

	AL – D0	AL – D1	AL – D2	AL – D3
Y41 – RMS [m]	4.48E-05	5.48E-04	1.20E-03	6.95E-03
Y42 – RMS [m]	4.24E-05	5.51E-04	1.24E-03	6.84E-03

Table 5.2: Alignment measured values

Note that, even if a correct validation according to [19] is not possible in a single run for the alignment, the estimated RMS values of Y41 and Y42 are very similar to each other, and a hypothetic transfer function or coherence function evaluated on them would have been acceptable.

5.6 *PROFILE IDENTIFICATION AND COMPARISON WITH THE OPTICAL SYSTEMS*

We perform now a profile identification according to EN 13848 ([18],[19], and [20]) and then compare the statistical results obtained with the ones evaluated through the MerMec's opto-electronic Track Geometry measuring system (from now on, called TGMS).
The TGMS uses a non-contact optical technology to detect several track geometry parameters, such as: track gauge, cross level, twist, alignment, and longitudinal levels.

Figure 5.38: MerMec's Track Geometry Measuring System

The Accelerometers / TGMS validation will be carried out comparing the evaluated values of the last aforementioned track parameter on the same rail segment.

For the sake of the corporate confidentiality about the TGMS recordings, no GPS values will be shown and none of the railway line name will be declared in the next paragraphs.

5.6.1 METHODOLOGY

In order to obtain a perfect match between the displacement signals measured by the TGMS and the displacements obtained started from the sampled ABAs, all accelerations (that are sampled with a constant time frequency) needs to be reconstructed to achieve an equivalent constant space sampling frequency, even in non-constant vehicle speed recording conditions.
Moreover, note that the sampling frequency of the TGMS is lower than the ABA's one: the first takes a sample every 250 mm while the second measures at 2.5 kHz (just to give an idea, for a vehicle speed of 100 km/h, this sampling frequency corresponds to about one sample every 11 mm). This means that the ABA's data will be strongly sub-sampled during the signal's reconstruction from constant-time sampling to constant-space sampling.

The inertial displacements have been obtained by a double integration (and double detrend, in order to compensate any possible sensors' measuring offsets) of the ABAs in the given frequency ranges (i.e., D1 and D2 using a 4^{th} order Butterworth filter), as suggested by the standard [18].

For this kind of analysis, knowing that the nominal radius of the vehicle's wheel is equal to 0.452 m and that the minimum wavelength inspected is equal to 3 m, no inspection about an identification of the running wheel profile has been implemented.

5.6.2 CASE 1

In the first case, we compared the measures made on the same rail length of 1000 m, run at a constant vehicle speed of 156 km/h.

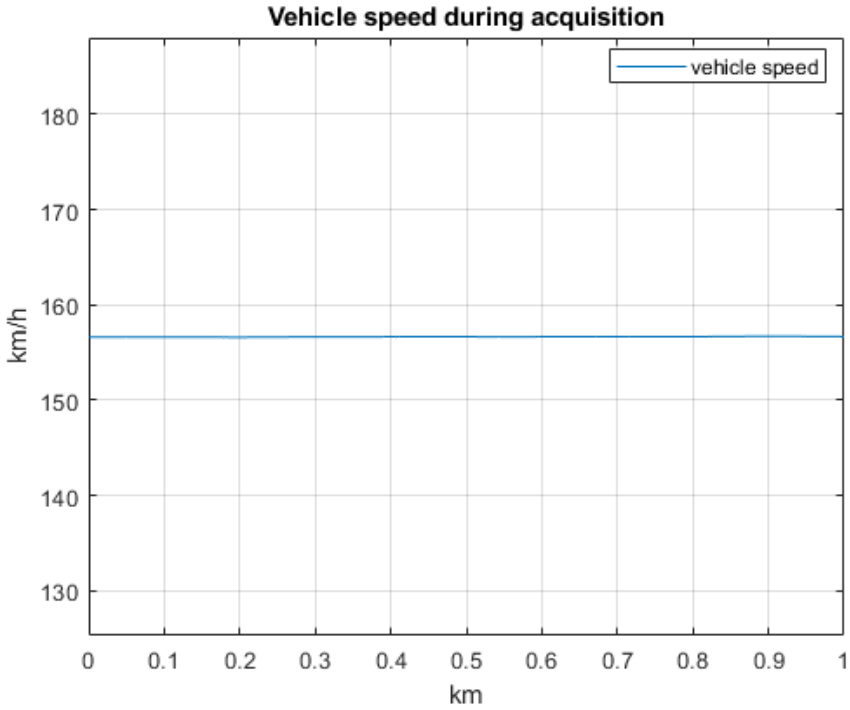

Figure 5.39: Vehicle speed during acquisition

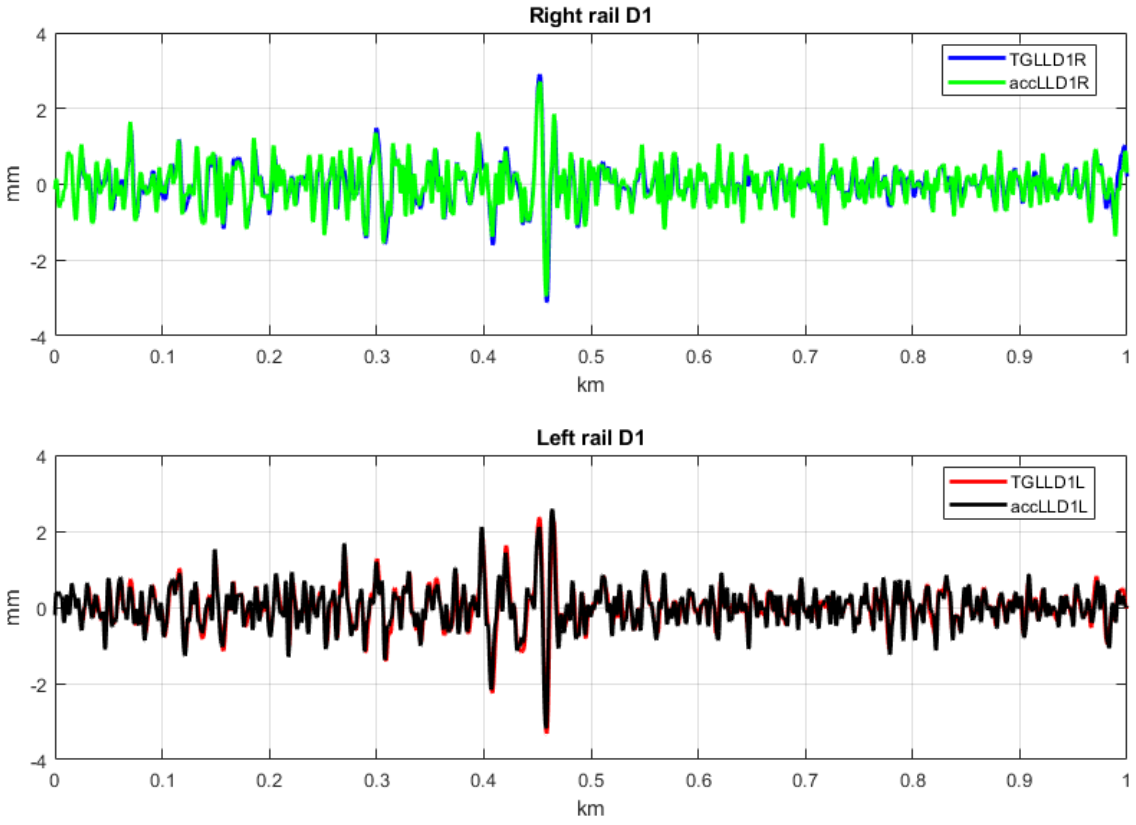

Figure 5.40: Rail profile evaluation – TGMS vs ABA (displacements) – Wavelength range: D1

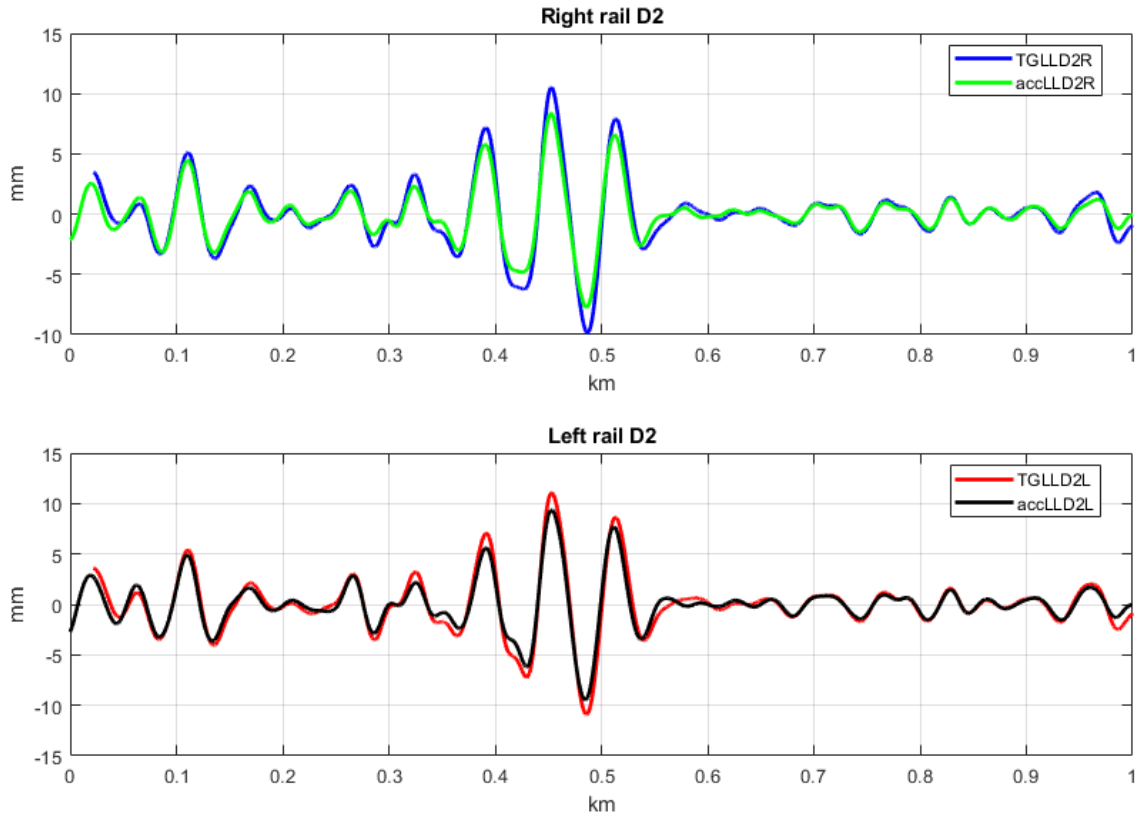

Figure 5.41: Rail profile evaluation – TGMS vs ABA (displacements) – Wavelength range: D2

Next table summarizes the results of the rail head profile evaluation made by both technologies. Note that, thus the accelerometer Z12 has to be considered as an outlier, all inertial rail profiles have been evaluated exploiting a single sensor per side (i.e., Z41 and Z42, the ABAs of axle 4, according to Figure 5.1) so these estimations have been carried out without any redundance.

	Right LL – D1	Left LL – D1	Right LL – D2	Left LL – D2
ACC – RMS [mm]	0.540	0.536	2.151	2.443
TGMS – RMS [mm]	0.525	0.529	2.692	2.882
Transfer function ACC / TGMS	2.8%	1.4%	20.1%	15.3%
Transfer function Tolerances	±7%	±7%	±10%	±10%

Table 5.3: Rail head estimation and comparison between Accelerometers (ACC) and Track Geometry (TGMS) - 1

The previous table underlines a great result for what concerns D1 wavelength range of the Longitudinal Level estimation but an out of tolerance estimation of the D2 wavelength rage.
Nevertheless, Figure 5.41 shows an identical trend of the two measuring systems despite some lack in the ABAs gain. This may depend on the absence of a proper ABA's sensors redundance.
We are confident that future measuring campaigns, made with a higher number of accelerometers, will solve this issue.

5.6.3 CASE 2

In the second case, we compared the measures made on the same rail length of 1000 m, run at a non-constant vehicle speed, increasing from 69 to 93 km/h.

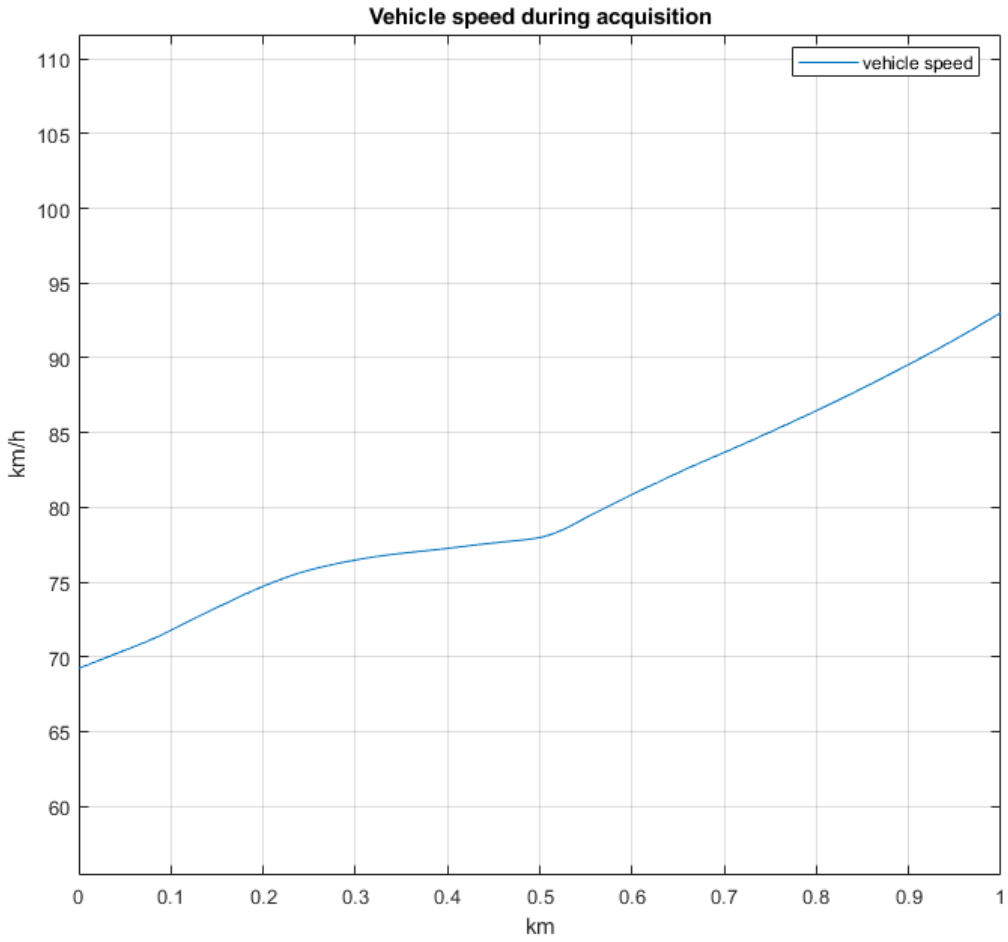

Figure 5.42: Vehicle speed during acquisition

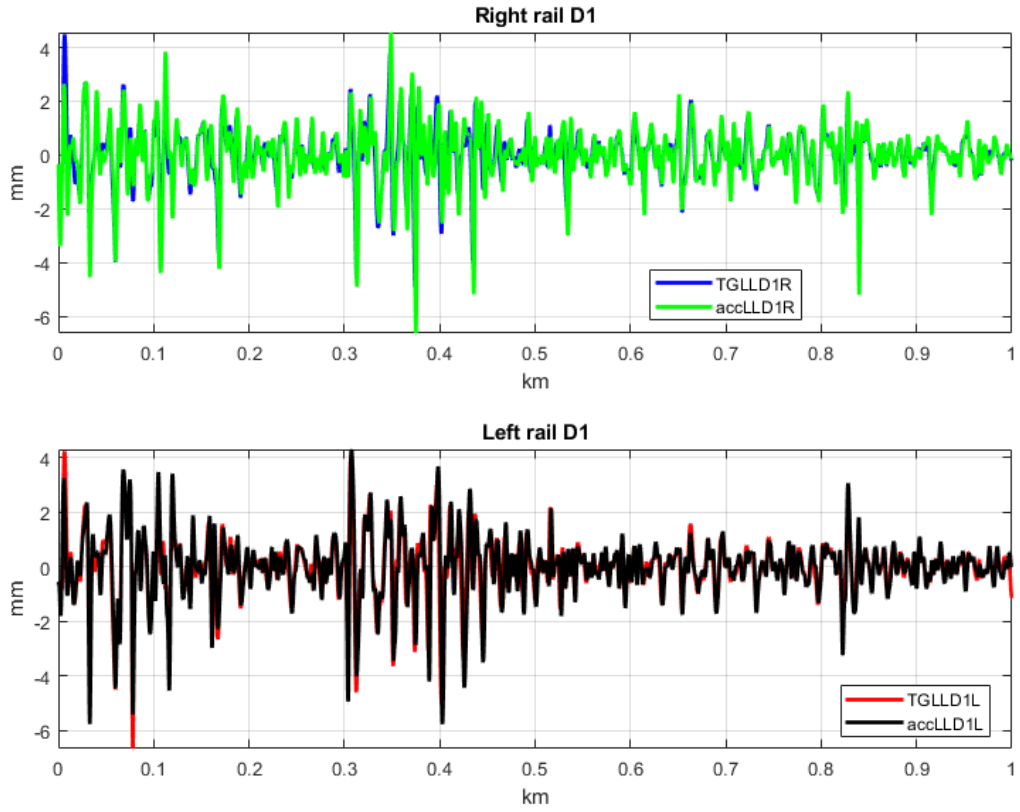

Figure 5.43: Rail profile evaluation – TGMS vs ABA (displacements) – Wavelength range: D1

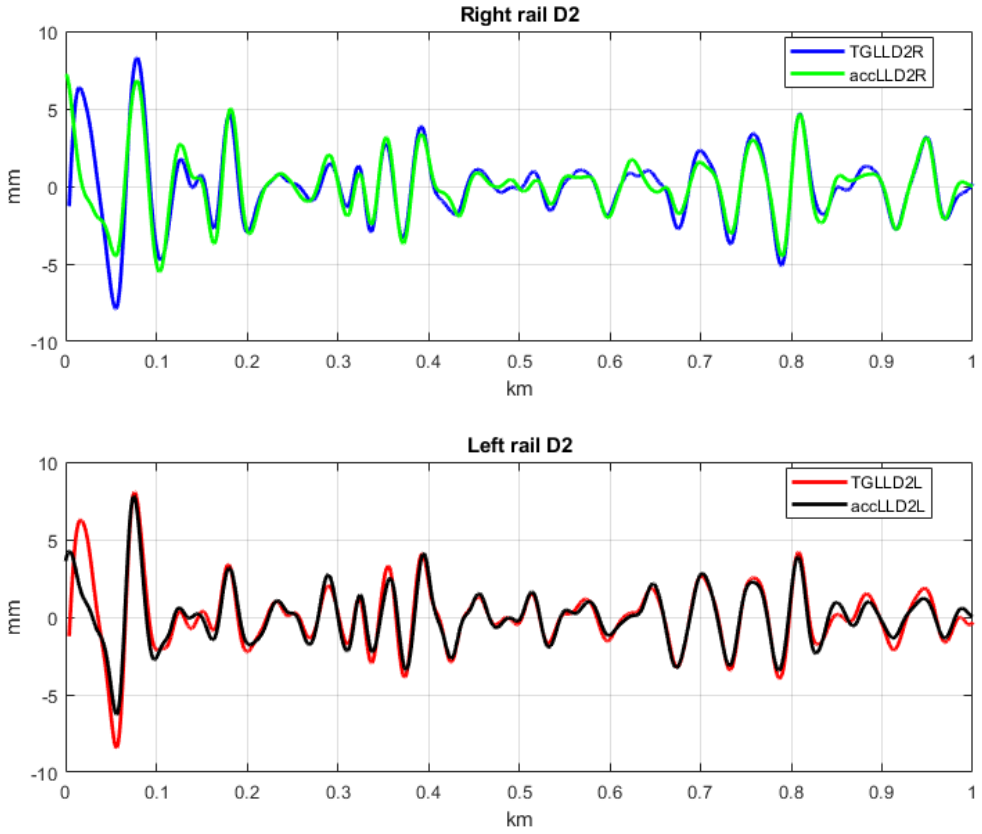

Figure 5.44: Rail profile evaluation – TGMS vs ABA (displacements) – Wavelength range: D2

Next table summarizes the results of the rail head profile evaluation made by both technologies. Note that, thus the accelerometer Z12 has to be considered as an outlier, all inertial rail profiles have been evaluated exploiting a single sensor per side (i.e., Z41 and Z42, the ABAs of axle 4, according to Figure 5.1) so these estimations have been carried out without any redundance.

	Right LL – D1	Left LL – D1	Right LL – D2	Left LL – D2
ACC – RMS [mm]	1.155	1.098	2.026	1.843
TGMS – RMS [mm]	0.962	1.055	2.121	2.275
Transfer function ACC / TGMS	20.0%	4.1%	4.5%	19.0%
Transfer function Tolerances	±7%	±7%	±10%	±10%

Table 5.4: Rail head estimation and comparison between Accelerometers (ACC) and Track Geometry (TGMS) - 1

This test case gave us interesting results: the reproducibility tolerances results to be satisfied alternatively for wavelength D1 or D2 for both right and left ABA. Even there, a wider amount of sensors would probably gave us better information about the accuracy of this inertial track geometry estimator, but it is still true that the trends of all curves are extremely similar one to the other even in this non-constant vehicle speed recording condition.

5.6.4 CASE 3

In the third case, we compared the measures made on the same rail length of 1000 m, run at a non-constant vehicle speed, decreasing from 143 to 131 km/h.

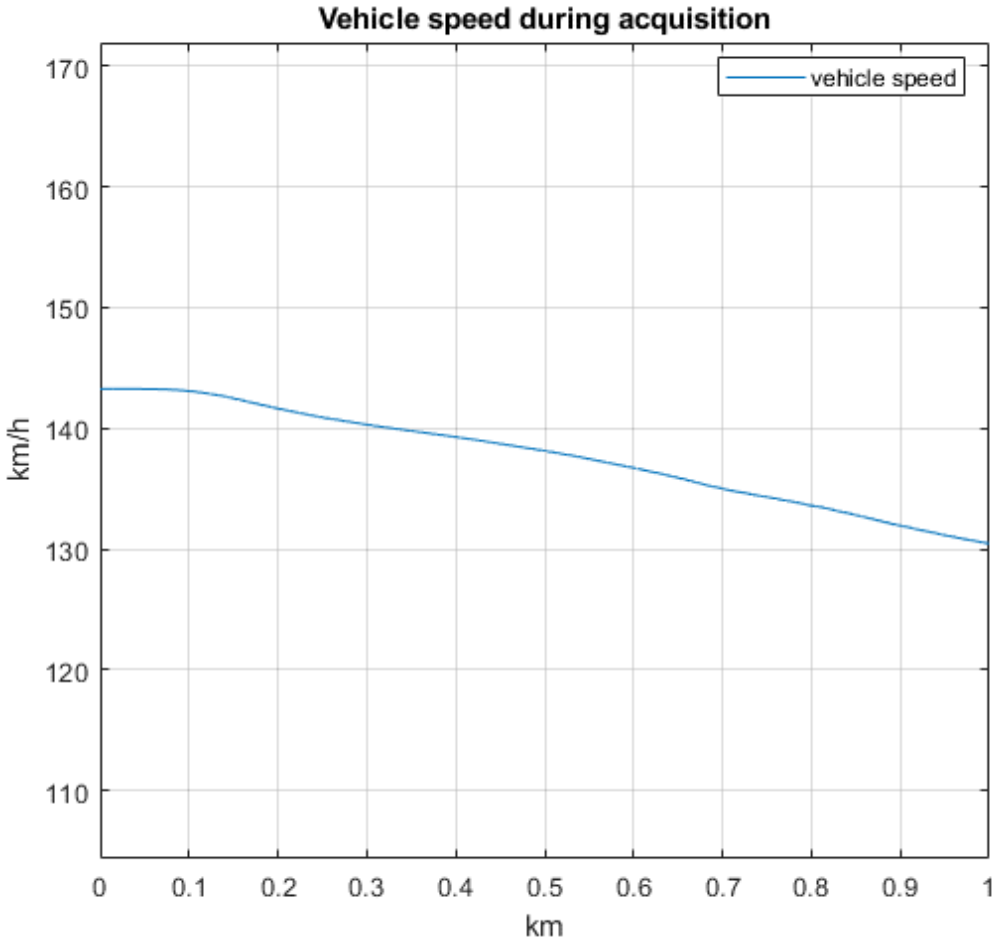

Figure 5.45: Vehicle speed during acquisition

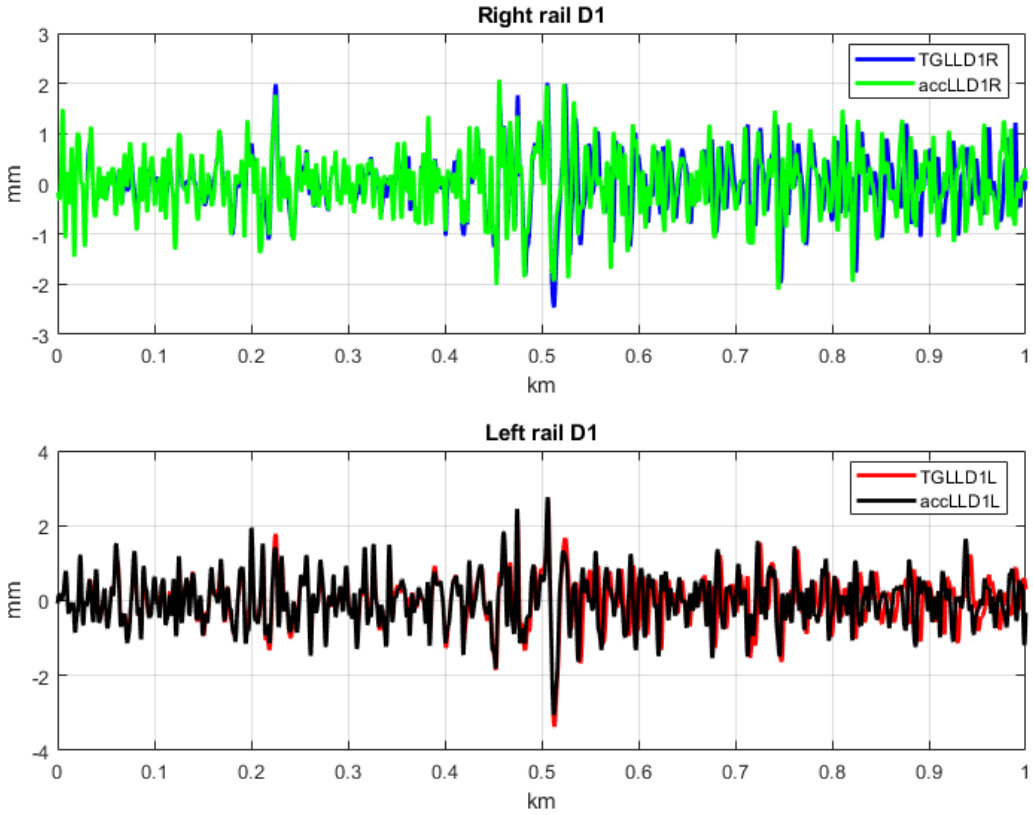

Figure 5.46: Rail profile evaluation – TGMS vs ABA (displacements) – Wavelength range: D1

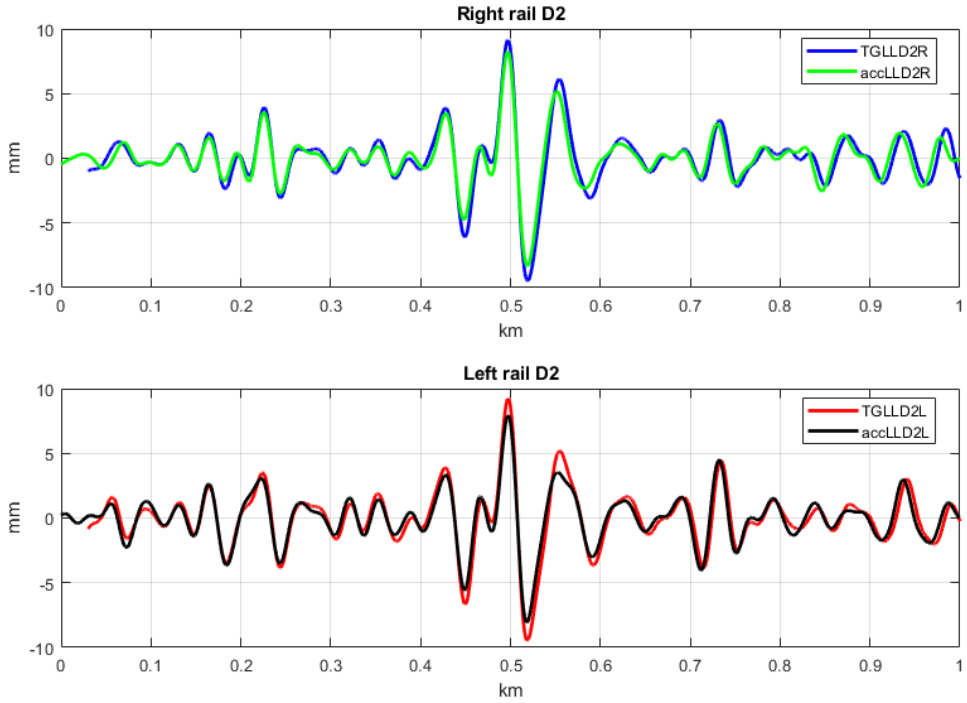

Figure 5.47: Rail profile evaluation – TGMS vs ABA (displacements) – Wavelength range: D2

Next table summarizes the results of the rail head profile evaluation made by both technologies. Note that, thus the accelerometer Z12 has to be considered as an outlier, all inertial rail profiles have been evaluated exploiting a single sensor per side (i.e., Z41 and Z42, the ABAs of axle 4, according to Figure 5.1) so these estimations have been carried out without any redundance.

	Right LL – D1	Left LL – D1	Right LL – D2	Left LL – D2
ACC – RMS [mm]	0.620	0.655	2.000	1.853
TGMS – RMS [mm]	0.585	0.642	2.167	2.290
Transfer function ACC / TGMS	5.9%	2.0%	7.7%	19.1%
Transfer function Tolerances	±7%	±7%	±10%	±10%

Table 5.5: Rail head estimation and comparison between Accelerometers (ACC) and Track Geometry (TGMS) - 3

This third identification case clarify that the ABAs could be a good estimator of the rail head profile for all wavelengths higher than 3 m, without the necessity of identifying the whole vehicle's FRF, but starting from a sufficiently large set of sensors, in order to exploit a proper redundance of measures to reduce at minimum the effects of stochastic recording errors.

6 CONCLUSIONS

The results obtained in the identification of the roughness profiles through the theoretical models and through the experimental analyses, represent a starting point for future developments in this research field.

In chapter 4 it is shown how, having a complete knowledge of vehicle dynamics, it is possible to carry out different types of analyses that allow to reach more precise results in terms of estimating roughness profiles and related parameters. In particular, the modified OMA method (the so called *In-Operation Modal Analysis* or *Track-Vehicle Interaction Modal Model* [4],[24]) allows to obtain excellent results starting from the sole knowledge of the system responses and its geometric and mechanical characteristics, all these data are easily obtainable in the cases of real vehicles by means of accelerometric measurements and design data. From the analysis of the various model cases, it was evident that the estimates of the profiles and related parameters are extremely close to those taken as a reference, and this is true as well for the estimated parameters of the model itself (vehicle identification).

The in-Operation Modal Analysis effectively represents a tool with enormous potential in this field not only for vehicle identification, but also in the identification of roughness profiles at any wavelength of interest. However, the analysis of the data on models made it possible to obtain also other interesting points from which to start for the analysis of the experimental case. We have seen how it is possible to make a non-parametric estimate of the time lags by exploiting only information from the system's response cross-PSDs. Another important consideration concerns the fact that, at first glance, it is possible to use the auto-PSD of displacements of the unsuspended masses to estimate the roughness profiles, in particular for low frequencies (and so for high wavelength). In this way it is possible to identify, in a first stage of the analysis, the profile category. This consideration also allows a non-parametric estimate of the coherence between the auto-PSDs of the displacements of the unsuspended masses which, as we have seen, is indicative of the coherence between the PSDs of the profiles.

All results obtained with the theoretical models and subsequent considerations have therefore made it possible to obtain useful indications for the real case analysis. The profiles identification by using the Gonzalez method, or simply by the auto-PSD of displacements of the unsuspended masses, represents only a preliminary stage, which in any case allowed to get good estimates. However, this method, compared to OMA, presents the limit of the need to know the profile with which the transfer function is calculated, which in the cases studied has only been hypothesized. For this reason, applying the OMA method to the real case is the next natural step. For this purpose, it is necessary to have a greater amount of data, regarding both the geometry or dynamics of the system, and the responses of the system. Moreover, an enrichment of the measurement system's layout with a higher number of sensors than the actual layout available in the diagnostic train represents a necessary condition for carrying out this kind of analyses. For example, think of the expressions of the operational vector (2.87) and of the modified polynomial model (2.88) in which the time lag terms appear, which can be obtained either by knowing the forward speed and the geometry of the vehicle, or by mounting accelerometers on all axles and exploiting the non-parametric estimate of the delays. Another key element for future developments could be a larger comparison between the accelerometric OMA results and those obtained through the optical systems, e.g. the MerMec's Track Geometry Measuring System, along all wavelength ranges, even the rail corrugation or the rail roughness.

The conclusions reached can be summarized in the following points:

- the analyses and estimates of the profiles carried out on the model data are adherent to those given as input and represent a starting point for the case of real vehicles;

- the Gonzalez method has the limit of having to know the calibration profile, a limit that results to be overcome by exploiting the modified OMA method; furthermore, calibration depends on the particular speed condition and therefore this operation must be repeated for different speed values;

- after a sufficiently high number of system responses measurements, it is possible to recreate some typical inertial stress load cycles and exploit them during the design phase of any critical instrumentation to be installed on vehicle body, bogie frame or axle box, in order to perform a dynamic structural verification using the real input stresses instead of the “almost white noises” suggested by the standard [21];

- with the actual accelerometers layout of the MerMec diagnostic vehicle, it has been possible to evaluate with sufficient accuracy (according to the standard [18], [19] and [19]) all categories of longitudinal levels and alignment but the results estimated for the detection of low wavelength (or high frequency) defect were not acceptable due to the no more unitary transmissibility value at high frequencies between the wheel and rail profile. Moreover, all longitudinal level estimations made starting from the ABA have been validated through a successful comparison with the same results obtained by the MerMec’s opto-electronic Track Geometry Measuring System (TGMS);

- for the application of the OMA method to the real case, a greater number of accelerometric sensors is required and this represent the most important future step in order to complete the study stage of a new diagnostic system.

7 APPENDICES

7.1 APPENDIX A

The damping and stiffness matrices of the 17 dof full-train model are as follows:

$$C = \begin{bmatrix}
4c_2 & 0 & 0 & -2c_2 & 0 & 0 & -2c_2 & 0 & 0 & 0 & 0 & 0 & 0 & 0 & 0 & 0 & 0 \\
0 & 4c_2l_2^2 & 0 & 2c_2l_2 & 0 & 0 & -2c_2l_2 & 0 & 0 & 0 & 0 & 0 & 0 & 0 & 0 & 0 & 0 \\
0 & 0 & 4c_2b_2^2 & 0 & 0 & -2c_2b_2 & 0 & 0 & 0 & 0 & 0 & 0 & 0 & 0 & 0 & 0 & 0 \\
-2c_2 & 2c_2l_2 & 0 & 4c_1 + 2c_2 & 0 & 0 & 0 & 0 & 0 & 0 & 0 & 0 & 0 & 0 & 0 & 0 & 0 \\
0 & 0 & 0 & 0 & 4c_1l_1^2 & 0 & 0 & 0 & 0 & 0 & 0 & 0 & 0 & 0 & 0 & 0 & 0 \\
0 & 0 & -2c_2b_2 & 0 & 0 & 2c_2b_2^2 + 4c_1b_1^2 & 0 & 0 & 0 & 0 & 0 & 0 & 0 & 0 & 0 & 0 & 0 \\
-2c_2 & -2c_2l_2 & 0 & 0 & 0 & 0 & 4c_1 + 2c_2 & 0 & 0 & 0 & 0 & 0 & 0 & 0 & 0 & 0 & 0 \\
0 & 0 & 0 & 0 & 0 & 0 & 0 & 4c_1l_1^2 & 0 & 0 & 0 & 0 & 0 & 0 & 0 & 0 & 0 \\
0 & 0 & -2c_2b_2 & 0 & 0 & 0 & 0 & 0 & 2c_2b_2^2 + 4c_1b_1^2 & 0 & 0 & 0 & 0 & 0 & 0 & 0 & 0 \\
0 & 0 & 0 & -c_1 & c_1l_1 & c_1b_1 & -c_1 & c_1l_1 & 0 & c_1 & 0 & 0 & 0 & 0 & 0 & 0 & 0 \\
0 & 0 & 0 & -c_1 & -c_1l_1 & c_1b_1 & -c_1 & -c_1l_1 & c_1b_1 & 0 & c_1 & 0 & 0 & 0 & 0 & 0 & 0 \\
0 & 0 & 0 & -c_1 & c_1l_1 & -c_1b_1 & -c_1 & c_1l_1 & -c_1b_1 & 0 & 0 & c_1 & 0 & 0 & 0 & 0 & 0 \\
0 & 0 & 0 & -c_1 & -c_1l_1 & -c_1b_1 & -c_1 & -c_1l_1 & -c_1b_1 & 0 & 0 & 0 & c_1 & 0 & 0 & 0 & 0 \\
0 & 0 & 0 & 0 & 0 & 0 & 0 & 0 & 0 & c_1 & 0 & 0 & 0 & c_1 & 0 & 0 & 0 \\
0 & 0 & 0 & 0 & 0 & 0 & 0 & 0 & 0 & 0 & c_1 & 0 & 0 & 0 & c_1 & 0 & 0 \\
0 & 0 & 0 & 0 & 0 & 0 & 0 & 0 & 0 & 0 & 0 & c_1 & 0 & 0 & 0 & c_1 & 0 \\
0 & 0 & 0 & 0 & 0 & 0 & 0 & 0 & 0 & 0 & 0 & 0 & c_1 & 0 & 0 & 0 & c_1
\end{bmatrix}$$

$$
K = \begin{bmatrix}
4k_2 & 0 & 0 & -2k_2 & 0 & 0 & -2k_2 & 0 & 0 & 0 & 0 & 0 & 0 & 0 & 0 & 0 & 0 & 0 & 0 & 0 \\
0 & 4k_2b_2^2 & 0 & 2k_2l_2 & 0 & 0 & -2k_2l_2 & 0 & 0 & 0 & 0 & 0 & 0 & 0 & 0 & 0 & 0 & 0 & 0 & 0 \\
0 & 0 & 4k_2b_2^2 & 0 & 0 & -2k_2b_2 & 0 & 0 & -2k_2b_2 & 0 & 0 & 0 & 0 & 0 & 0 & 0 & 0 & 0 & 0 & 0 \\
-2k_2 & 2k_2l_2 & 0 & 4k_1 + 2k_2 & 0 & 0 & 0 & 0 & 0 & -k_1 & -k_1 & 0 & 0 & 0 & 0 & 0 & 0 & 0 & 0 & 0 \\
0 & 0 & 0 & 0 & 4k_1l_1^2 & 0 & 0 & 0 & 0 & -k_1l_1 & -k_1l_1 & 0 & 0 & 0 & 0 & 0 & 0 & 0 & 0 & 0 \\
0 & 0 & -2k_2b_2 & 0 & 0 & 2k_2b_2^2 + 4k_1b_1^2 & 0 & 0 & 0 & -k_1b_1 & -k_1b_1 & 0 & 0 & 0 & 0 & 0 & 0 & 0 & 0 & 0 \\
-2k_2 & -2k_2l_2 & 0 & 0 & 0 & 0 & 4k_1 + 2k_2 & 0 & 0 & 0 & 0 & k_1 + k_h & 0 & 0 & 0 & 0 & 0 & 0 & 0 & 0 \\
0 & 0 & 0 & 0 & 0 & 0 & 0 & 4k_1l_1^2 & 0 & 0 & 0 & 0 & k_1 + k_h & 0 & 0 & 0 & 0 & 0 & 0 & 0 \\
0 & 0 & -2k_2b_2 & 0 & 0 & 0 & 0 & 0 & 2k_2b_2^2 + 4k_1b_1^2 & 0 & 0 & 0 & 0 & k_1 + k_h & 0 & 0 & 0 & 0 & 0 \\
0 & 0 & 0 & -k_1 & k_1l_1 & k_1b_1 & -k_1 & k_1l_1 & k_1b_1 & k_1 + k_h & 0 & 0 & 0 & 0 & k_1 + k_h & 0 & 0 & 0 & 0 \\
0 & 0 & 0 & -k_1 & -k_1l_1 & k_1b_1 & -k_1 & -k_1l_1 & k_1b_1 & 0 & k_1 + k_h & 0 & 0 & 0 & 0 & k_1 + k_h & 0 & 0 & 0 \\
0 & 0 & 0 & -k_1 & k_1l_1 & -k_1b_1 & -k_1 & k_1l_1 & -k_1b_1 & 0 & 0 & k_1 + k_h & 0 & 0 & 0 & 0 & k_1 + k_h & 0 & 0 \\
0 & 0 & 0 & -k_1 & -k_1l_1 & -k_1b_1 & -k_1 & -k_1l_1 & -k_1b_1 & 0 & 0 & 0 & k_1 + k_h & 0 & 0 & 0 & 0 & k_1 + k_h & 0 \\
0 & 0 & 0 & 0 & 0 & 0 & 0 & 0 & 0 & 0 & 0 & 0 & 0 & k_1 + k_h & 0 & 0 & 0 & 0 & 0 & k_1 + k_h
\end{bmatrix}
$$

7.2 APPENDIX B

The influence matrices of the 6 dof system are shown below:

$$T_1 = \begin{bmatrix} 0 & 0 & 0 & 0 & 0 & 0 \\ 0 & 0 & 0 & 0 & 0 & 0 \\ 0 & 0 & c_1 & c_1 & 0 & 0 \\ 0 & 0 & c_1 l_1 & -c_1 l_1 & 0 & 0 \\ 0 & 0 & 0 & 0 & c_1 & c_1 \\ 0 & 0 & 0 & 0 & c_1 l_1 & -c_1 l_1 \end{bmatrix}$$

$$T_2 = \begin{bmatrix} 0 & 0 & 0 & 0 & 0 & 0 \\ 0 & 0 & 0 & 0 & 0 & 0 \\ 0 & 0 & k_1 & k_1 & 0 & 0 \\ 0 & 0 & k_1 l_1 & -k_1 l_1 & 0 & 0 \\ 0 & 0 & 0 & 0 & k_1 & k_1 \\ 0 & 0 & 0 & 0 & k_1 l_1 & -k_1 l_1 \end{bmatrix}$$

The force applied to the system is given by the relation:

$$F(\omega) = T_1 \begin{bmatrix} 0 \\ 0 \\ Y_1'(\omega) \\ Y_2'(\omega) \\ Y_3'(\omega) \\ Y_4'(\omega) \end{bmatrix} + T_2 \begin{bmatrix} 0 \\ 0 \\ Y_1(\omega) \\ Y_2(\omega) \\ Y_3(\omega) \\ Y_4(\omega) \end{bmatrix}$$

where the apex indicates that it is the transform of the derivative (the speed) while the subscripts (from 1 to 4) indicate the transform of the input signal linked to the contact points indicated in figure 3.1 (any out of phase signal is obtained according to what is described in subsection 2.3.2).

For the 10 dof system the T1 matrix is null:

$$T_2 = \begin{bmatrix} 0 & 0 & 0 & 0 & 0 & 0 & 0 & 0 & 0 & 0 \\ 0 & 0 & 0 & 0 & 0 & 0 & 0 & 0 & 0 & 0 \\ 0 & 0 & 0 & 0 & 0 & 0 & 0 & 0 & 0 & 0 \\ 0 & 0 & 0 & 0 & 0 & 0 & 0 & 0 & 0 & 0 \\ 0 & 0 & 0 & 0 & 0 & 0 & 0 & 0 & 0 & 0 \\ 0 & 0 & 0 & 0 & 0 & 0 & 0 & 0 & 0 & 0 \\ 0 & 0 & 0 & 0 & 0 & 0 & k_h & 0 & 0 & 0 \\ 0 & 0 & 0 & 0 & 0 & 0 & 0 & k_h & 0 & 0 \\ 0 & 0 & 0 & 0 & 0 & 0 & 0 & 0 & k_h & 0 \\ 0 & 0 & 0 & 0 & 0 & 0 & 0 & 0 & 0 & k_h \end{bmatrix}$$

The force matrix applied to the system is given by the relation:

$$F(\omega) = T_2 \begin{bmatrix} 0 \\ 0 \\ 0 \\ 0 \\ 0 \\ 0 \\ Y_1(\omega) \\ Y_2(\omega) \\ Y_3(\omega) \\ Y_4(\omega) \end{bmatrix}$$

here the subscripts (from 1 to 4) indicate the transform of the input signal linked to the contact points indicated in figure 3.4.

The T1 matrix is null for the 17 dof system too:

$$T_2 = \begin{bmatrix}
0 & 0 & 0 & 0 & 0 & 0 & 0 & 0 & 0 & 0 & 0 & 0 & 0 & 0 & 0 & 0 & 0 \\
0 & 0 & 0 & 0 & 0 & 0 & 0 & 0 & 0 & 0 & 0 & 0 & 0 & 0 & 0 & 0 & 0 \\
0 & 0 & 0 & 0 & 0 & 0 & 0 & 0 & 0 & 0 & 0 & 0 & 0 & 0 & 0 & 0 & 0 \\
0 & 0 & 0 & 0 & 0 & 0 & 0 & 0 & 0 & 0 & 0 & 0 & 0 & 0 & 0 & 0 & 0 \\
0 & 0 & 0 & 0 & 0 & 0 & 0 & 0 & 0 & 0 & 0 & 0 & 0 & 0 & 0 & 0 & 0 \\
0 & 0 & 0 & 0 & 0 & 0 & 0 & 0 & 0 & 0 & 0 & 0 & 0 & 0 & 0 & 0 & 0 \\
0 & 0 & 0 & 0 & 0 & 0 & 0 & 0 & 0 & 0 & 0 & 0 & 0 & 0 & 0 & 0 & 0 \\
0 & 0 & 0 & 0 & 0 & 0 & 0 & 0 & 0 & 0 & 0 & 0 & 0 & 0 & 0 & 0 & 0 \\
0 & 0 & 0 & 0 & 0 & 0 & 0 & 0 & 0 & 0 & 0 & 0 & 0 & 0 & 0 & 0 & 0 \\
0 & 0 & 0 & 0 & 0 & 0 & 0 & 0 & 0 & k_h & 0 & 0 & 0 & 0 & 0 & 0 & 0 \\
0 & 0 & 0 & 0 & 0 & 0 & 0 & 0 & 0 & 0 & k_h & 0 & 0 & 0 & 0 & 0 & 0 \\
0 & 0 & 0 & 0 & 0 & 0 & 0 & 0 & 0 & 0 & 0 & k_h & 0 & 0 & 0 & 0 & 0 \\
0 & 0 & 0 & 0 & 0 & 0 & 0 & 0 & 0 & 0 & 0 & 0 & k_h & 0 & 0 & 0 & 0 \\
0 & 0 & 0 & 0 & 0 & 0 & 0 & 0 & 0 & 0 & 0 & 0 & 0 & k_h & 0 & 0 & 0 \\
0 & 0 & 0 & 0 & 0 & 0 & 0 & 0 & 0 & 0 & 0 & 0 & 0 & 0 & k_h & 0 & 0 \\
0 & 0 & 0 & 0 & 0 & 0 & 0 & 0 & 0 & 0 & 0 & 0 & 0 & 0 & 0 & k_h & 0 \\
0 & 0 & 0 & 0 & 0 & 0 & 0 & 0 & 0 & 0 & 0 & 0 & 0 & 0 & 0 & 0 & k_h
\end{bmatrix}$$

The force matrix applied to the system is given by the relation:

$$F(\omega) = T_2 \begin{bmatrix} 0 \\ 0 \\ 0 \\ 0 \\ 0 \\ 0 \\ 0 \\ 0 \\ 0 \\ Y_1^{sx}(\omega) \\ Y_2^{sx}(\omega) \\ Y_1^{dx}(\omega) \\ Y_2^{dx}(\omega) \\ Y_3^{sx}(\omega) \\ Y_4^{sx}(\omega) \\ Y_3^{dx}(\omega) \\ Y_4^{dx}(\omega) \end{bmatrix}$$

Subscripts and apexes refer to the axles (1 to 4) and profiles (left and right) of figure 3.8. In this case, in addition to the time lag, it is also necessary to consider the correlation between left and right profile through the coherence function (described in subsection 2.3.2).
For the three models, the time lags used to obtain the related transforms are defined as follows:

$$\tau_{12} = \frac{2l_1}{u}$$
$$\tau_{13} = \frac{2l_2}{u}$$
$$\tau_{14} = \frac{2l_2 + 2l_1}{u}$$
$$\tau_{23} = \frac{2l_2 - 2l_1}{u}$$
$$\tau_{24} = \frac{2l_2}{u}$$
$$\tau_{34} = \frac{2l_1}{u}$$

7.3 APPENDIX C

In subsection 3.2.2 we have seen the relation:

$$G_{out}(\omega_i) = H(\omega_i)[j\omega_i T_1' + T_2']G_{in}(\omega_i)[j\omega_i T_1' + T_2']^H H^H(\omega_i)$$

Where the matrices T_1' and T_2' for the 6 dof model are:

$$T_1' = \begin{bmatrix} 0 & 0 & 0 & 0 \\ 0 & 0 & 0 & 0 \\ c_1 & c_1 & 0 & 0 \\ c_1 l_1 & -c_1 l_1 & 0 & 0 \\ 0 & 0 & c_1 & c_1 \\ 0 & 0 & c_1 l_1 & -c_1 l_1 \end{bmatrix}$$

$$T_2' = \begin{bmatrix} 0 & 0 & 0 & 0 \\ 0 & 0 & 0 & 0 \\ k_1 & k_1 & 0 & 0 \\ k_1 l_1 & -k_1 l_1 & 0 & 0 \\ 0 & 0 & k_1 & k_1 \\ 0 & 0 & k_1 l_1 & -k_1 l_1 \end{bmatrix}$$

For the 10 dof model, where T_1' is null, we have:

$$T_2' = \begin{bmatrix} 0 & 0 & 0 & 0 \\ 0 & 0 & 0 & 0 \\ 0 & 0 & 0 & 0 \\ 0 & 0 & 0 & 0 \\ 0 & 0 & 0 & 0 \\ 0 & 0 & 0 & 0 \\ k_h & 0 & 0 & 0 \\ 0 & k_h & 0 & 0 \\ 0 & 0 & k_h & 0 \\ 0 & 0 & 0 & k_h \end{bmatrix}$$

For the 17 dof model, where T_1' is null, we have:

$$T_2' = \begin{bmatrix} 0 & 0 & 0 & 0 & 0 & 0 & 0 & 0 \\ 0 & 0 & 0 & 0 & 0 & 0 & 0 & 0 \\ 0 & 0 & 0 & 0 & 0 & 0 & 0 & 0 \\ 0 & 0 & 0 & 0 & 0 & 0 & 0 & 0 \\ 0 & 0 & 0 & 0 & 0 & 0 & 0 & 0 \\ 0 & 0 & 0 & 0 & 0 & 0 & 0 & 0 \\ 0 & 0 & 0 & 0 & 0 & 0 & 0 & 0 \\ 0 & 0 & 0 & 0 & 0 & 0 & 0 & 0 \\ 0 & 0 & 0 & 0 & 0 & 0 & 0 & 0 \\ k_h & 0 & 0 & 0 & 0 & 0 & 0 & 0 \\ 0 & k_h & 0 & 0 & 0 & 0 & 0 & 0 \\ 0 & 0 & k_h & 0 & 0 & 0 & 0 & 0 \\ 0 & 0 & 0 & k_h & 0 & 0 & 0 & 0 \\ 0 & 0 & 0 & 0 & k_h & 0 & 0 & 0 \\ 0 & 0 & 0 & 0 & 0 & k_h & 0 & 0 \\ 0 & 0 & 0 & 0 & 0 & 0 & k_h & 0 \\ 0 & 0 & 0 & 0 & 0 & 0 & 0 & k_h \end{bmatrix}$$

Below are the matrices $G_{in}(\omega_i)$ for the three models analyzed, constructed with the same criterion as in (2.75).

Note that, considering equation (3.21) for each ω_i, the matrices $\mathrm{H}(\omega)$, $G_{in}(\omega)$ and $G_{out}(\omega)$ are actually tensors, in which the third dimension is represented precisely by the number of lines (i.e., the spectral resolution) with which the spectra have been discretized.

For 6 and 10 dof systems the matrix is the same:

$$G_{in}(\omega_i) = G_d(\omega_i)\begin{bmatrix} 1 & e^{j\omega_i\tau_{12}} & e^{j\omega_i\tau_{13}} & e^{j\omega_i\tau_{14}} \\ e^{-j\omega_i\tau_{12}} & 1 & e^{j\omega_i\tau_{23}} & e^{j\omega_i\tau_{24}} \\ e^{-j\omega_i\tau_{13}} & e^{-j\omega_i\tau_{23}} & 1 & e^{j\omega_i\tau_{34}} \\ e^{-j\omega_i\tau_{14}} & e^{-j\omega_i\tau_{24}} & e^{-j\omega_i\tau_{34}} & 1 \end{bmatrix}$$

While for the 17 dof system the matrix is the one showed in next page.

$$G_{in}(\omega_i) = G_d(\omega_i)\begin{bmatrix} 1 & e^{-j\omega_i\tau_{12}} & \Gamma(\omega_i) & \Gamma(\omega_i)e^{-j\omega_i\tau_{12}} & e^{-j\omega_i\tau_{13}} & e^{-j\omega_i\tau_{14}} & \Gamma(\omega_i)e^{-j\omega_i\tau_{13}} & \Gamma(\omega_i)e^{-j\omega_i\tau_{14}} \\ e^{j\omega_i\tau_{12}} & 1 & \Gamma(\omega_i)e^{j\omega_i\tau_{12}} & \Gamma(\omega_i) & e^{-j\omega_i\tau_{23}} & e^{-j\omega_i\tau_{24}} & \Gamma(\omega_i)e^{-j\omega_i\tau_{23}} & \Gamma(\omega_i)e^{-j\omega_i\tau_{24}} \\ \Gamma(\omega_i) & \Gamma(\omega_i)e^{-j\omega_i\tau_{12}} & 1 & e^{-j\omega_i\tau_{12}} & \Gamma(\omega_i)e^{-j\omega_i\tau_{13}} & \Gamma(\omega_i)e^{-j\omega_i\tau_{14}} & e^{-j\omega_i\tau_{13}} & e^{-j\omega_i\tau_{14}} \\ \Gamma(\omega_i)e^{j\omega_i\tau_{12}} & \Gamma(\omega_i) & e^{j\omega_i\tau_{12}} & 1 & \Gamma(\omega_i)e^{-j\omega_i\tau_{23}} & \Gamma(\omega_i)e^{-j\omega_i\tau_{24}} & e^{-j\omega_i\tau_{23}} & e^{-j\omega_i\tau_{24}} \\ e^{j\omega_i\tau_{13}} & e^{j\omega_i\tau_{23}} & \Gamma(\omega_i)e^{j\omega_i\tau_{13}} & \Gamma(\omega_i)e^{j\omega_i\tau_{23}} & 1 & e^{-j\omega_i\tau_{34}} & \Gamma(\omega_i) & \Gamma(\omega_i)e^{-j\omega_i\tau_{34}} \\ e^{j\omega_i\tau_{14}} & e^{j\omega_i\tau_{24}} & \Gamma(\omega_i)e^{j\omega_i\tau_{14}} & \Gamma(\omega_i)e^{j\omega_i\tau_{24}} & e^{j\omega_i\tau_{34}} & 1 & \Gamma(\omega_i)e^{j\omega_i\tau_{34}} & \Gamma(\omega_i) \\ \Gamma(\omega_i)e^{j\omega_i\tau_{13}} & \Gamma(\omega_i)e^{j\omega_i\tau_{23}} & e^{j\omega_i\tau_{13}} & e^{j\omega_i\tau_{23}} & \Gamma(\omega_i) & \Gamma(\omega_i)e^{-j\omega_i\tau_{34}} & 1 & \Gamma(\omega_i)e^{-j\omega_i\tau_{34}} \\ \Gamma(\omega_i)e^{j\omega_i\tau_{14}} & \Gamma(\omega_i)e^{j\omega_i\tau_{24}} & e^{j\omega_i\tau_{14}} & e^{j\omega_i\tau_{24}} & \Gamma(\omega_i)e^{j\omega_i\tau_{34}} & \Gamma(\omega_i) & e^{j\omega_i\tau_{34}} & 1 \end{bmatrix}^T$$

8 REFERENCES

[1] R.J. Allemang and D.L. Brown. *Experimental modal analysis*. 1996

[2] Peter Andrén. «Power spectral density approximations of longitudinal road profiles». In: *International Journal of Vehicle Design - INT J VEH DES* 40 (gen. 2006). DOI: 10.1504/IJVD.2006.008450.

[3] K. Bogsjö. «Coherence of road roughness in left and right wheel-path». In: *Vehicle System Dynamics* 46.sup1 (2008), pp. 599–609. doi: 10.1080/00423110802018289. eprint: https://doi.org/10.1080/00423110802018289. url: https://doi.org/10.1080/00423110802018289.

[4] Giovanni De Filippis et al. «Method for determining the modal parameters of road or rail vehicles and for the indirect characterization of road or rail profiles». English. WO2017/064734 A1. 2017.

[5] W. Fauriat et al. «Estimation of road profile variability from measured vehicle responses». In: *Vehicle System Dynamics* 54.5 (2016), pp. 585–605. doi: 10.1080/00423114.2016.1145243. eprint: https://doi.org/10.1080/00423114.2016.1145243. url: https://doi.org/10.1080/00423114.2016.1145243.

[6] Jun Feng et al. «A Frequency Compensation Algorithm of Four-Wheel Coherence Random Road». In: *Mathematical Problems in Engineering* 2013 (set. 2013). doi: 10.1155/2013/986584.

[7] Arturo Gonzalez et al. «The use of vehicle acceleration measurements to estimate road roughness». In: *Vehicle System Dynamics - VEH SYST DYN* 46 (giu. 2008), pp. 483–499. doi: 10.1080/00423110701485050.

[8] A. Hamid et al. *Analytical Descriptions of Track Geometry Variations: Appendices*. Analytical Descriptions of Track Geometry Variations. Federal Railroad Administration, Office of Research e Development, 1983. url: https://books.google.it/books?id=GQ46AQAAMAAJ.

[9] Xiandong Liu et al. «Construction of road roughness in left and right wheel paths based on PSD and coherence function». In: *Mechanical Systems and Signal Processing* 60-61 (2015), pp. 668–677. issn: 0888-3270. doi: https://doi.org/10.1016/j.ymssp.2015.01.034. url: https://www.sciencedirect.com/science/article/pii/S088832701500045X.

[10] *Matlab. Signal Processing Toolbox User's Guide (R2021a)*. Manuale utenti. 2021.

[11] L. Meirovitch. *Fundamentals of Vibrations*. McGraw-Hill higher education. McGraw-Hill, 2001. isbn: 9780070413450. url: https://books.google.it/books?id=u358QgAACAAJ.

[12] D.E. Newland. *An Introduction to Random Vibrations and Spectral Analysis*. Longman, 1984. isbn: 9780582305304. url: https://books.google.it/books?id=MQBRAAAAMAAJ.

[13] A. Nokhbatolfoghahai, M. A. Noorian e H. Haddadpour. «Dynamic response of tank trains to random track irregularities». In: *Meccanica* 53.10 (2018), pp. 2687–2703. doi: 10.1007/s11012-018-0849-8. url: https://doi.org/10.1007/s11012-018-0849-8.

[14] M.P. Norton e D.G. Karczub. *Fundamentals of Noise and Vibration Analysis for Engineers*. Cambridge University Press, 2003. isbn: 9780521499132. url: https://books.google.it/books?id=jDeRCSqtev4C.

[15] R.B. Randall. *Vibration-based Condition Monitoring: Industrial, Aerospace and Automotive Applications*. EBL-Schweitzer. Wiley, 2011. isbn: 9780470977583. url: https://books.google.it/books?id=5eybNQNbXdYC.

[16] Leonardo Soria et al. «Operational Modal Analysis and the Performance Assessment of Vehicle Suspension Systems». In: *Shock and Vibration* 19 (gen. 2012), pp. 1099–1113. doi: 10.1155/2012/127316.

[17] *UNI 8608:2015. Mechanical vibration – Road surface profiles – Reporting of measured data*. Norma UNI: 2015.

[18] *EN 13848-1:2019.* Railway applications – Track – Track geometry quality – Part 1: Characterization of track geometry.

[19] *EN 13848-2:2021.* Railway applications – Track – Track geometry quality – Part 2: Measuring systems – Track recording vehicles.

[20] *EN 13848-5:2021.* Railway applications – Track – Track geometry quality – Part 5: Geometry quality levels – Plain line, switches, and crossings.

[21] *IEC 61373:2010.* Railway applications – Rolling stock equipment – Shock and vibration tests.

[22] F. Miccoli et al. *Operational Modal Analysis for the dynamic identification of railway vehicle*. Master's degree thesis – Academic Year 2020/2021

[23] Sussman, N.E. (1974) `Statistical ground excitation models for high-speed vehicle dynamics analysis', High Speed Ground Transportation Journal, Vol. 8, No. 3, pp.145±154.

[24] G. Bisceglia et al. *Operational Modal Analysis for the evaluation and classification of rail-head irregularities and the simultaneous identification of train modal parameters*. ISMA 2022. http://past.isma-isaac.be/downloads/isma2022/proceedings/Contribution_574_proceeding_3.pdf